The Dissertation Committee for Scott Staniewicz
Certifies that this is the approved version of the following Dissertation:

Surface Deformation Mapping and Automatic Feature Detection over the Permian Basin using InSAR

Committee:

Jingyi Ann Chen, Supervisor

Srinivas Bettadpur

Peter Hennings

Todd Humphreys

Jon Olson

Surface Deformation Mapping and Automatic Feature

Detection over the Permian Basin using InSAR

by

Scott Staniewicz

Dissertation

Presented to the Faculty of the Graduate School

of The University of Texas at Austin

in Partial Fulfillment

of the Requirements

for the Degree of

Doctor of Philosophy

The University of Texas at Austin

August 2022

Acknowledgments

Abstract

Surface Deformation Mapping and Automatic Feature Detection over the Permian Basin using InSAR

Scott Staniewicz, Ph.D.

The University of Texas at Austin, 2022

Supervisor: Jingyi Ann Chen

The Permian Basin has become the United States' largest producer of oil and gas over the past decade. During the same time, it has experienced a sharp rise in the number of induced earthquakes. In order to better understand the damage potential from induced earthquakes, new data and monitoring approaches are critically needed. Interferometric Synthetic Aperture Radar (InSAR) is a remote sensing technique that measures surface deformation over broad areas with 10s-100s meter spatial resolution and up to millimeter-to-centimeter accuracy. These measurements can be used to derive information about Earth's subsurface and assess induced seismic risks. However, it is difficult to perform basin-scale surface deformation mapping and automatic feature detection using InSAR because the signal-to-noise ratio (SNR) of the deformation signals compared to tropospheric noise is extremely low. It is common to assume that the Permian Basin is rigid enough that the subtle deformation associated with oil and gas production and wastewater injection are not detectable by InSAR.

In this dissertation, we develop methods for characterizing tropospheric noise and its power spectral density directly from InSAR observations. We show that the tropospheric noise distribution is non-Gaussian, and a small portion of SAR scenes are corrupted by up to $\pm$ 15 cm noise outliers associated with storms and heat waves. This finding is significant because most of the InSAR time series solutions are optimal

only when noise follows a Gaussian distribution. We design robust and scalable time series algorithms to reconstruct the temporal evolution of surface deformation in this challenging scenario, and we achieved basin-wide millimeter-level accuracy based on independent GPS validation. We observe numerous subsidence and uplift features near active production and disposal wells, as well as linear deformation patterns associated with fault activities near clusters of induced earthquakes. Furthermore, we designed a new computer vision algorithm for detecting the size and location of unknown deformation features in large volumes of InSAR data. We are able to determine whether a detected feature is associated with tropospheric artifacts or real deformation signals based on a realistic tropospheric noise model derived from InSAR data.

Table of Contents

List of Tables

List of Figures

Chapter 1

Introduction

1.1 Problem Background

The Permian Basin, stretching from eastern New Mexico and covering most of West Texas, has become the United States' largest producer of oil and gas over the past decade (Figure 1.1a). The region's production began to take off around 2009, largely due to advances in horizontal drilling and multi-stage hydraulic fracturing. The rapid expansion of oil and gas production from shale formations has created positive economic impacts as well as sociopolitical concerns, given that researchers have long recognized that injection or withdrawal of fluids from the subsurface can induce earthquakes along existing faults (Council, 2013, Simpson et al., 1988, Ellsworth, 2013). Similar to other oil production and wastewater injection sites around the world (e.g. the central and eastern United States, Canada, China, and Italy) (Foulger et al., 2018), the Permian Basin has experienced a dramatic rise in the rate of low magnitude earthquakes over the past decade (Frohlich et al., 2016a, Atkinson et al., 2016, Frohlich et al., 2019, Lomax and Savvaidis, 2019, Savvaidis et al., 2020, Skoumal et al., 2020a) (Figure 1.1b). For example, Texas recorded over 200 magnitude 3.0 or greater earthquakes in 2021, second only to California in the contiguous United States. While petroleum production and wastewater injection volumes have been rising throughout the basin, the recently cataloged earthquakes are spatially clustered. In order to assess the damage potential from induced and triggered earthquakes, we need to acquire new data and develop new monitoring approaches to better understand which earthquakes are induced, which wells they are associated with, and why some high-rate wells experience seismicity while others do not.

In 2017, the State of Texas funded a state-wide seismicity monitoring system, known as TexNet, which enables the cataloging of earthquakes across Texas at magnitudes down to M2.0 (Savvaidis et al., 2019). However, it is difficult to examine the mechanism, scale, scope, and consequences of induced seismicity in the geologically-complex Permian Basin. This is because (1) in-situ measurements of the Earth's subsurface (e.g. the fault geometries and characteristics of the petroleum reservoirs) are extremely limited; and (2) systematic and sustained collection of such data across
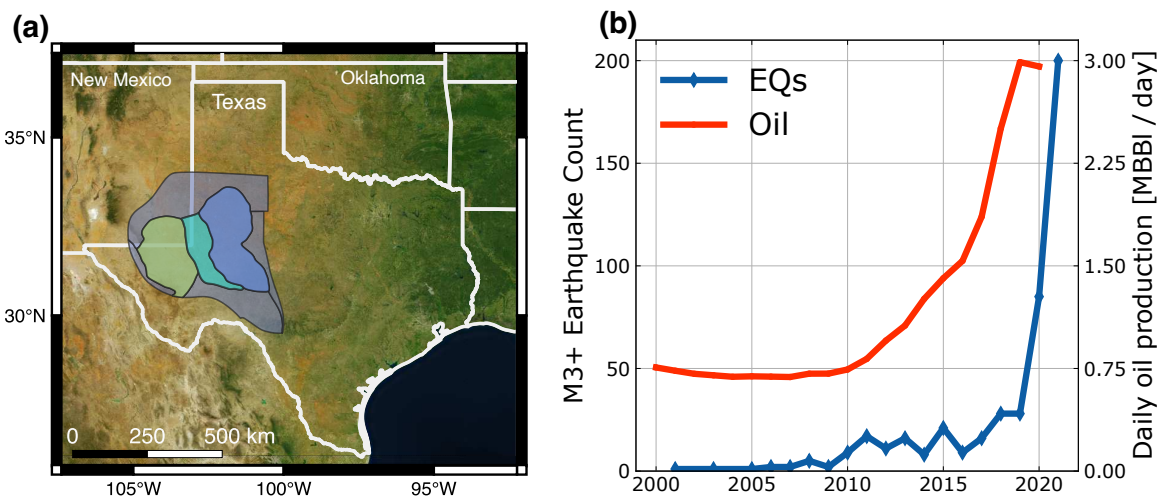
Figure 1.1: (a) Location of Permian Basin within Texas. The subbasins colored within the Permian Basin are (from west to east) the Delaware Basin (green), Central Basin Platform (cyan), and Midland Basin (purple). (b) Yearly number of magnitude 3 or larger earthquakes recorded within Texas since 2000 (blue line), and average daily oil production per year for Permian Basin wells in Texas (red line). Earthquakes retrieved from USGS at https://earthquake.usgs.gov . Oil Production data retrieved from the Texas Railroad Commission's production query system at https://www.rrc.texas.gov .

the $\sim$200,000 km^2 basin represents a costly undertaking with significant technical uncertainties (Hennings et al., 2021).

Since the launch of the Sentinel-1 mission in 2014, the quantity and quality of open-access Interferometric Synthetic Aperture Radar (SAR) data has grown exponentially. InSAR techniques can measure millimeter-to-centimeter deformation of Earth's surface over very wide areas with 10s-to-100s meter spatial resolution (Massonnet et al., 1993, Bürgmann et al., 2000). These high-quality surface deformation measurements can be used to locate previously unknown faults, estimate the distribution of fault slip, and infer associated seismic risk at low cost (Segall, 2010, Elliott et al., 2016, Huang et al., 2017). Shirzaei et al. (2016) reported indications of surface uplift due to wastewater injection near a 2012 M4.8 Timpson earthquake site, though limited validation for the InSAR results was available (Semple et al., 2017). Kim and Lu (2018) detected multiple deformation bowls within the Delaware Basin related to wastewater injection, CO_2 injection, and hydrocarbon production using Sentinel-1 InSAR data. Zheng et al. (2019) incorporated InSAR-derived surface deformation data into a poroelastic model to analyze the geomechanical processes near an uplift signal in northern West Texas. They discovered that the observed surface deformation was likely caused by injection well leakages rather than pressure increases at the planned injection depth, and the leaks may have contributed to freshwater contamination. Recently, Deng et al. (2020) used ascending Sentinel-1 measurements to infer pore pressure change and Coulomb failure stress change at three sites in the southern Delaware Basin. They suggested that certain groups of earthquakes are likely induced by fluid injection, but noted that local rock structure and media properties are key controls on the area's susceptibility to induced seismicity. Zhai et al. (2021) incorporated surface deformation measurements into a geomechanical model to propose that shallow injection is the dominant source of subsurface stress changes. Pepin et al. (2022) determined that the magnitude of fault slip required for the surface deformation observed in a region of the southern Delaware Basin suggests that the slip is predominantly aseismic.

The existing studies mainly focused on sites $\sim$ 60-by-60 km^2 or smaller, and basin-wide InSAR surface deformation data with detailed uncertainty quantification are needed for assessing regional induced seismicity risk. It is difficult to expand the InSAR spatial coverage to the entire Permian Basin while maintaining millimeter-level

accuracy because InSAR tropospheric noise variance increases with the distance away from a reference point (Emardson et al., 2003). There have been extensive efforts for mitigating InSAR tropospheric noise artifacts using global atmospheric models (GAMs) and other auxiliary data sources (Lauknes, 2011, Bekaert et al., 2015b, Doin et al., 2009, Li, 2005, Ding et al., 2008). However, these mitigation methods often do not have sufficient temporal and spatial resolution to capture tropospheric turbulence noise from localized storms, heat waves, or turbulent mixing of water vapor that are commonly observed in Sentinel-1 interferograms over West Texas.

Another challenge for large-scale InSAR analysis arises from the needs of automatic detection of InSAR deformation features. Because residual tropospheric noise is spatially coherent, these artifacts can be easily mistaken as real deformation features. Previous studies have developed algorithms for detecting deformation signals in pixel-wise InSAR deformation time series based on certain magnitude thresholds. The thresholds can be set manually (Raspini et al., 2018), set using pixel-wise standard deviations (Bekaert et al., 2020), derived from auxiliary data sources (e.g. global atmospheric weather models (Parker et al., 2015), MODIS water vapor measurements (Barnhart and Lohman, 2013)), or derived from simulated noise parameters (Havazli and Wdowinski, 2021). Principal component analysis (PCA) and independent component analysis (ICA) have also been used to explore decompositions of noisy time series data (Chaussard et al., 2014, Ebmeier, 2016, Gaddes et al., 2018). Moreover, deep learning methods using convolutional neural networks (CNNs) have been applied to detect deformation features in individual interferograms (Anantrasirichai et al., 2018; 2019a) or InSAR time series (Rouet-Leduc et al., 2021). Because the detection problems are posed as a supervised learning task, they require either labeled training data (Anantrasirichai et al., 2018) or ground truth examples from simulated noise and deformation models (Anantrasirichai et al., 2019b, Rouet-Leduc et al., 2021). These supervised learning approaches work well when deformation signals of interest show spatial signatures that are distinct from InSAR measurement noise. In many applications, both deformation signals and tropospheric turbulence noise are spatially coherent "blob-like" features that look similar to human observers. Additionally, not all algorithms have considered the detection uncertainty based on the noise characteristics of a particular InSAR dataset.

4

1.2   Contributions

The contributions of this dissertation center around designing scalable methods to produce reliable surface deformation maps over large regions. We focus on the mitigation of strong tropospheric noise, as well as the uncertainty quantification of InSAR time series solutions. The contributions are summarized as follows:

1. We developed Python-based InSAR time series analysis software that processes geocoded SAR images acquired from multiple imaging geometries and reconstructs surface deformation in eastward and vertical directions.

2. We performed a rigorous analysis of all noise sources in the Permian Basin Sentinel-1 InSAR data. We identified that the dominant noise term is the tropospheric turbulence noise with up to 15 cm non-Gaussian outliers. We developed methods for characterizing tropospheric noise and its power spectral density directly from InSAR data, as well as methods for mitigating the impact of the troposphere noise outliers.

3. We designed scalable, robust time series algorithms for reconstructing the temporal evolution of surface deformation over very wide regions. Based on independent validation from GPS permanent stations, we achieved millimeter-level accuracy in the cumulative surface deformation solutions.

4. We developed a computer vision algorithm for automatically detecting surface deformation signals of unknown sizes in basin-scale InSAR maps. The detection algorithm produces uncertainty measures for each detected feature based on a realistic tropospheric turbulence noise model.

5. Our InSAR deformation maps reveal numerous subsidence and uplift features near active production and disposal wells, as well as linear deformation patterns associated with fault activities near clusters of seismic activity. The maps are now openly available through the Center for Integrated Seismicity Research (CISR) for the broader scientific community and stakeholders.

1.3 Thesis Roadmap

In Chapter 2, we introduce the principles of Interferometric Synthetic Aperture Radar (InSAR). We start with a review of synthetic aperture radar (SAR) image formation. We show how the phase difference between two SAR images acquired at different times can be used to infer topography or surface deformation. We discuss common InSAR noise sources and their origins, and we show how to combine many interferograms to solve for a time series of surface deformation. Finally, we show how the use of geocoded single-look complex (SLC) SAR images enables a simple InSAR processing workflow.

In Chapter 3, we introduce the scientific background of the induced seismicity problem. We first review the oil and gas production boom of the last decade within the Permian Basin, as well as previous studies on the increase in low magnitude earthquakes during this time. We then describe the geodetic datasets available for monitoring the study site, and discuss the general InSAR data processing strategy and data quality.

In Chapter 4, we present a simple yet effective time series method for mapping cumulative surface deformation over very wide regions. The method incorporates an automated outlier detection and removal algorithm, which enabled 2 mm/year accuracy in the presence of severe non-Gaussian tropospheric noise based on indepedent GPS validation.

In Chapter 5, we expand our robust time series methods for reconstructing non-linear deformation. We present an InSAR time series analysis algorithm using non-parametric Locally Weighted Scatterplot Smoothing (LOWESS). We apply this method to derive the temporal evolution of surface deformation (2015-2021) over the Permian Basin using Sentinel-1 data.

In Chapter 6, we develop a computer vision algorithm based on Laplacian of Gaussian filters for automatically detecting surface deformation signals in InSAR maps. To quantify the likelihood that a detected feature is related to tropospheric noise artifacts, we estimate the tropospheric noise spectrum directly from InSAR data and simulate new instances of noise that resemble the actual InSAR observations.

Finally, we conclude with a summary and suggest areas of future work in Chapter 7.

Chapter 2

Radar Interferometry Background

In this chapter, we introduce the technical principles of Interferometric Synthetic Aperture Radar (InSAR). We provide background on Synthetic Aperture Radar (SAR) image formation and show how the phase difference between two SAR images acquired at different times can be used to infer surface deformation. We outline common InSAR noise sources, and we show how to combine many interferograms to derive time series of surface deformation. Finally, we outline an efficient InSAR processing workflow using geocoded single-look complex (SLC) images.

2.1 Radar Imaging

While originally an acronym for "RAdio Detection And Ranging", radar has entered into the common vernacular. Unlike passive sensors, such as optical cameras, that rely on illumination from outside sources, a radar is an active sensor that emits its own electromagnetic energy. As such, radars are able to operate both day and night, and they generally operate at microwave frequencies that are not blocked by clouds (between ~ 1 GHz and 300 GHz, or wavelengths of 3 m to 1 mm).

The original radars developed during World War 2 were for tracking the position of targets. In these systems, the range to the target is calculated from the round trip travel time of an electromagnetic pulse that reflects off the target, and the angle is determined by the antenna pointing direction. Researchers later developed imaging radar systems that convert a series of radar pulses on a moving platform into a two-dimension image. Although these side-looking radar images originally had coarse resolution, fine resolution images were first demonstrated in the research led by Carl Wiley at Goodyear in the 1950s. The research later led to the imaging technique known as Synthetic Aperture Radar (SAR) (Wiley, 1954; 1985).

The first demonstration of a spaceborne Earth-observing SAR mission with interferometric capability was Seasat, launched by NASA in 1978 (Born et al., 1979, Gabriel et al., 1989). Since that time, there have been dozens of missions launched by various space agencies, leading some to call the last decade "the golden age of SAR" (Moreira, 2014).
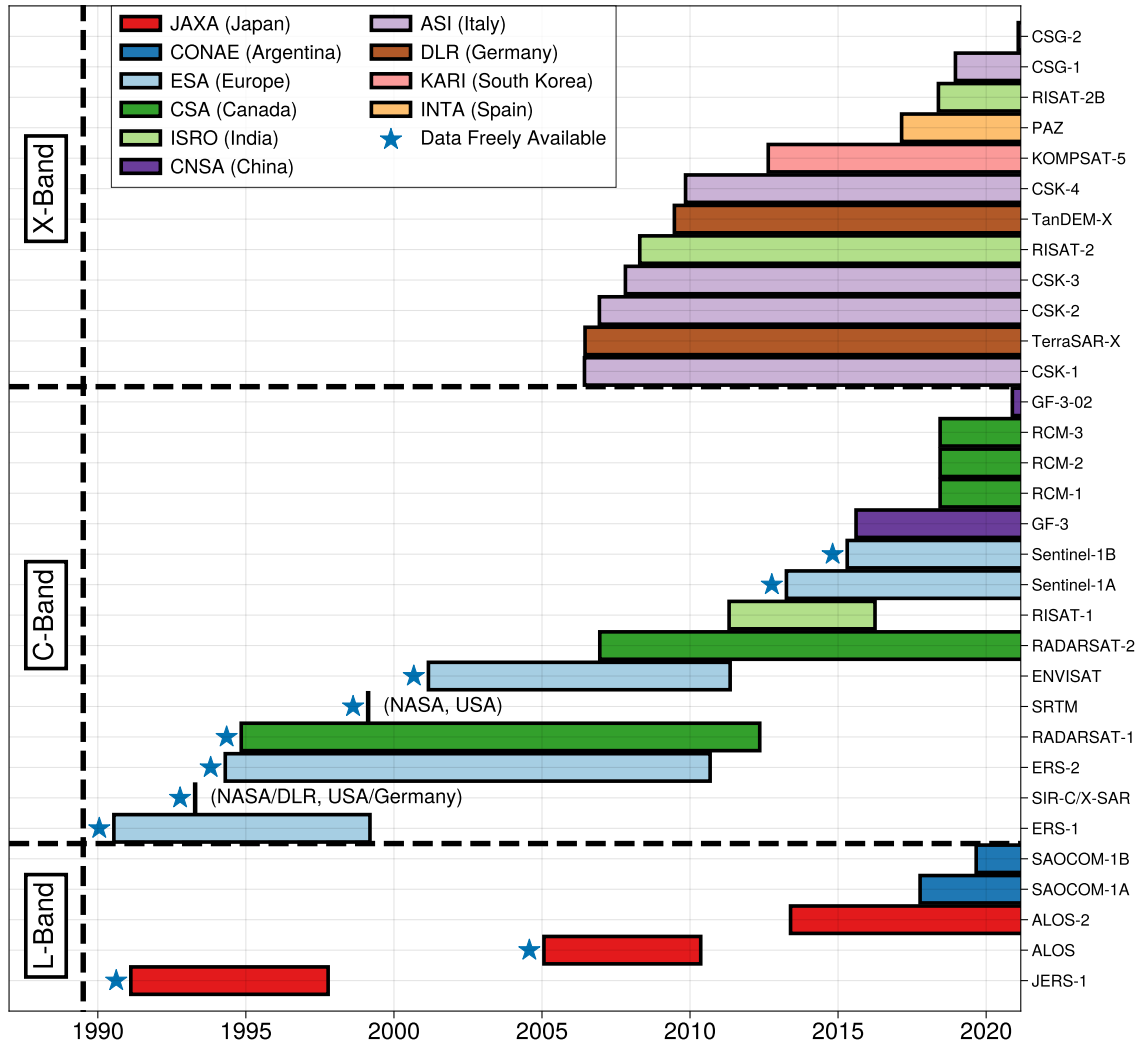
Figure 2.1: Timeline of government-sponsored SAR missions since 1990. Bar lengths indicate life span of mission. Bars which intersect the right edge indicate ongoing missions. Colors indicate the space agency operating the mission. Missions which provide data free of charge to the general public (as of May 2022) are marked with blue stars. Vertical sections of the timeline are divided by the radar frequency of the sensor, showing (from top to bottom) the X-band, C-band, and L-band missions. Note that SIR-C/X-SAR and SRTM were equipped with both C- and X-band sensors.

Figure 2.1 shows a timeline of SAR missions that have been launched by governments and space agencies since 1990. The missions are grouped vertically into the three most commonly used frequency bands for SAR sensors in Earth-observing missions: L-band (wavelengths of $\sim$24 cm), C-band ($\sim$6 cm) and X-band ($\sim$3 cm). During the 90s, the European Space Agency (ESA) launched two C-band SAR satellites: ERS-1 in 1991 and ERS-2 in 1995. The ERS-1 satellite provided the first practical demonstration of spaceborne InSAR's ability to capture surface deformation when Massonnet et al. (1993) mapped the surface deformation pattern caused by the 1992 earthquake in Landers, California. The first L-band SAR satellite, JERS-1, was launched by NASDA[1] in 1992, and the Canadian Space Agency (CSA) launched their own C-band mission, RADARSAT-1, in 1995. In 2000, NASA flew the 11-day Shuttle Radar Topography Mission (SRTM) to generate the first high-resolution near-global topographical map of Earth (Farr et al., 2007).

The most influential recent SAR mission within the science community has been Sentinel-1 (Torres et al., 2012). First launched in 2014, the Sentinel-1 satellites acquire $\sim$240 km wide images (Zan and Guarnieri, 2006), allowing them to revisit any point on Earth every 12 days. Additionally, Sentinel is the first mission of its kind to provide regularly updating free public data. While Sentinel-1 is currently the only active SAR mission with an open data policy, the future NASA-ISRO SAR mission (NISAR) will also provide L-band SAR data free to the public (Rosen et al., 2015).

In the past four years, the first small SAR SmallSats (satellites weighing under 180 kg) have been launched by a series of private companies (Figure 2.2). Finland's ICEYE had its first succesful launch in January 2018, while Capella Space had their first launch 11 months later. Seven other companies have since launched at least 1 SAR satellite, and in the next five years, there are plans to launch over 500 additional SAR SmallSats (Kulu, 2021). While many large SAR constellations expect sub-hourly revisit time for any given point on earth (Stringham et al., 2019), only the large government SAR missions, such as Sentinel-1, ALOS, and NISAR, explicitly plan for consistent global coverage in their mission objectives. However, the possibility of daily or hourly InSAR revisit times opens many new applications previously not possible with the 6-12 day revisit times of large SAR missions (Yague-Martinez et al.,

---

[1]Although JERS-1 is labeled as a JAXA mission in Figure 2.1, it was run by NASDA at the time. In 2003, NASDA merged with two other Japanese space agencies, ISAS and NAL, to form JAXA.
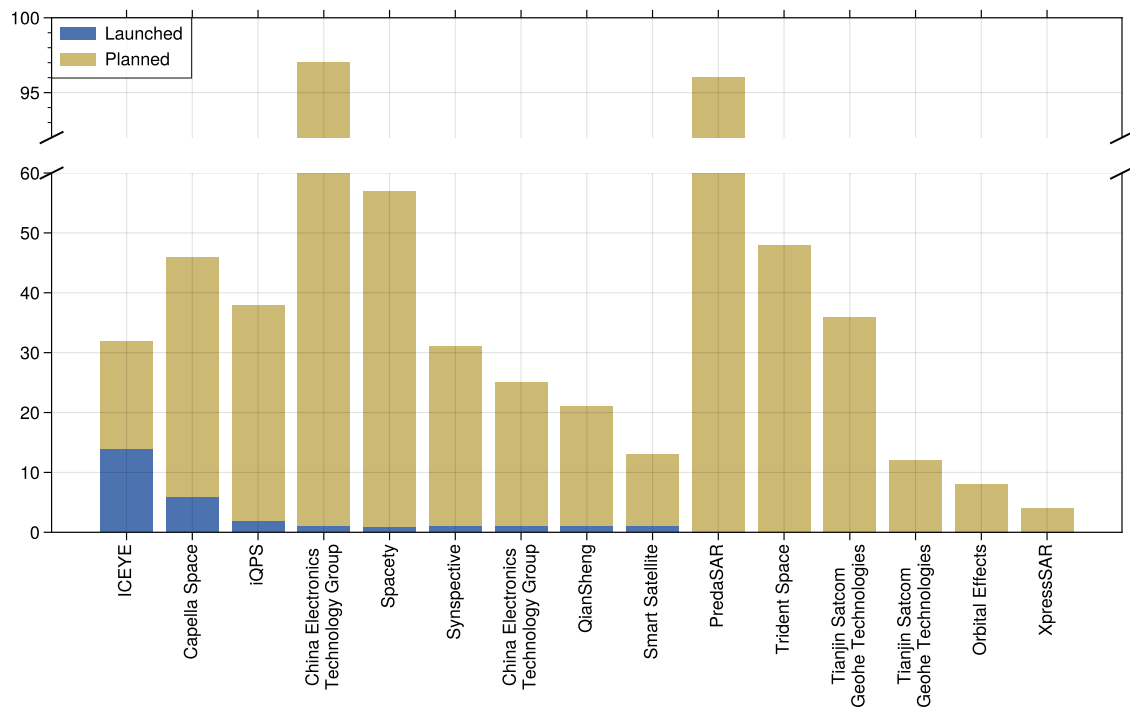
Figure 2.2: SAR constellations run by private companies, showing the number of currently launched satellites (blue) stacked under the number of future planned launches (gold). Note the broken y-axis scale, as two companies are planning constellations of 96 satellites.

2021, Taylor et al., 2021, Kitajima et al., 2021).

2.2   Synthetic Aperture Radar

Synthetic Aperture Radar is an imaging technique that uses a radar mounted on a moving platform. A two-dimensional image is created by coherently processing the returned energy from transmitted pulses. While the images are often displayed in grayscale and may appear similar to optical images, they represent the electrical and geometrical properties of the objects in the scene (Simons and Rosen, 2007).

The SAR imaging geometry is shown in Figure 2.3. A side-looking radar with look angle θ moves in the azimuth direction and repeatedly emits pulses at some interval (called the *pulse repetition interval*, or PRI) which travel in the range direction. The line of sight (LOS) vector is defined as the unit vector pointing from the radar antenna to a point in the illuminated swath. Each pulse illuminates a portion of the ground known as the radar footprint.

The signal-to-noise ratio (SNR) of the system depends on the total energy transmitted. SNR can be increased by either sending a higher peak power (which is often limited by design constraints) or sending pulses with longer duration τ. This choice creates a dilemma: in the absence further processing, sending pulses with a larger τ results in coarser range resolution δ_r, where resolution is the ability to distinguish points illuminated by the same radar pulse. The illuminated size in range is $\delta_r = \frac{c\tau}{2}$, where $c \approx 3 \times 10^8$ m/s is the speed of light. Thus, a pulse with $\tau = 30$ microseconds would have a resolution of approximately 4.5 km.

For this reason, SAR systems usually transmit pulsed waveforms called *chirps* whose frequency f increases or decreases over time. For example, in a linear frequency modulated (LFM) chirp, the frequency can be written as $f(t) = kt$ for $-\tau/2 < t < \tau/2$, where k is the chirp slope (in Hz / s). These special waveforms allow the receiver to correlate the returned echoes with a *matched filter*, or a replica of the transmitted chirp. The improved range resolution depends on the frequency bandwidth of the chirp: $BW = f_{max} - f_{min}$. For a given BW, the range resolution can be written as $\delta_r = \frac{c}{2BW}$.
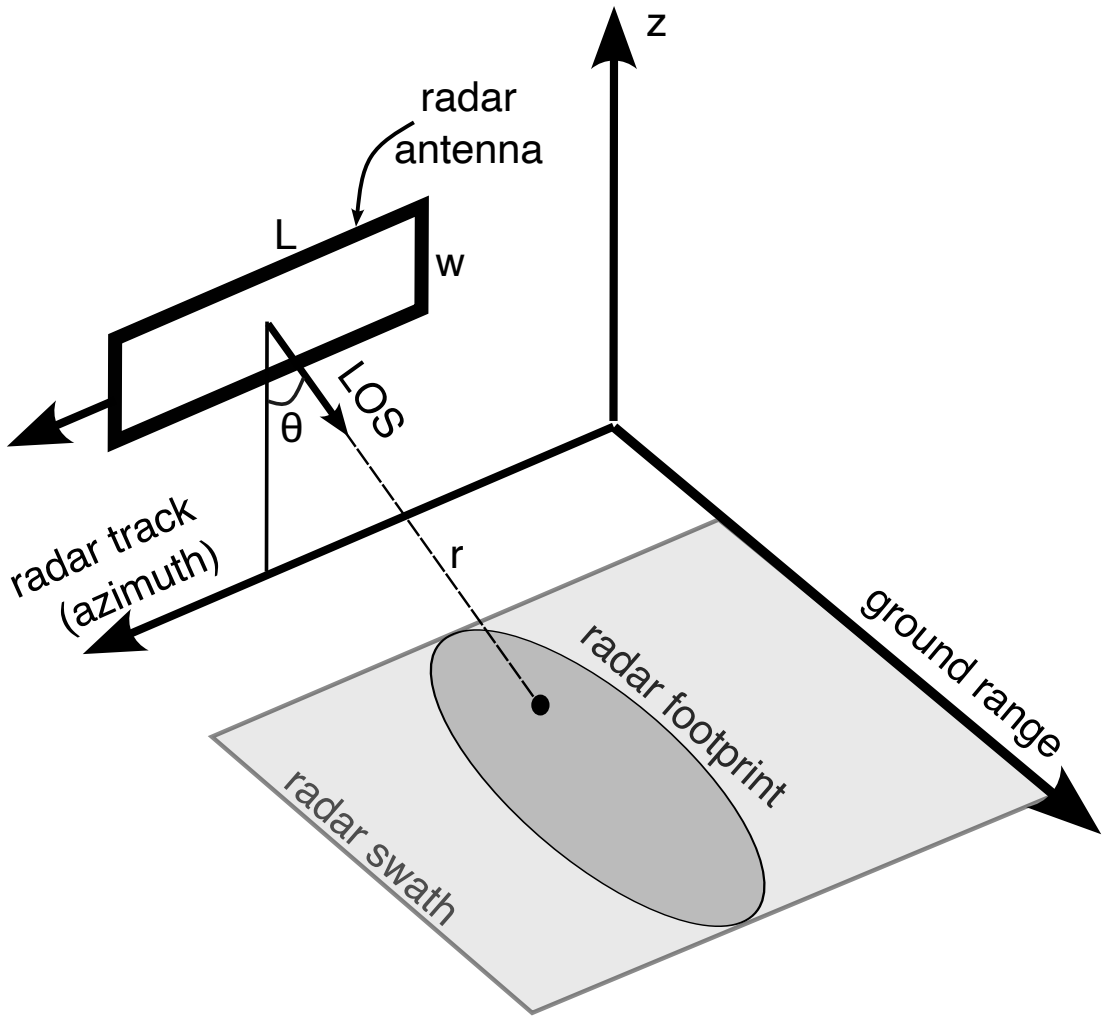
Figure 2.3:   A platform moving in the azimuth/along-track direction contains a radar instrument with look angle θ. The slant range r to the ground point is measured along the line-of-sight (LOS) direction from the antenna to the ground. The radar antenna shown has length L (in the azimuth direction) and width w. As the radar sends out pulses, each one illuminates into an area on the ground called the beam "footprint" (oval shape).

Figure 2.4 demonstrates the effect of using a chirp waveform on range resolution. An example chirp with parameters matching the ERS-1 satellite (Figure 2.4a) has a duration of $\tau \approx 37.12 \mu s$ and chirp slope $k = 4 \times 10^{11} Hz/s$, resulting in frequency bandwidth $BW = k\tau \approx 15.5$ MHz (Figure 2.4b). By convolving the transmitted chirp with its complex conjugate, we get the impulse response of a point scatterer

(Figure 2.4c). If a chirp with the same time duration had a smaller slope k (Figure 2.4d), the bandwidth would shrink by the same proportion (Figure 2.4e), and the impulse response would also have worse resolution (Figure 2.4f). Thus, we see that using chirped waveforms eliminates the original problem, as a longer pulse with larger bandwidth actually has a better resolution than a shorter pulse.
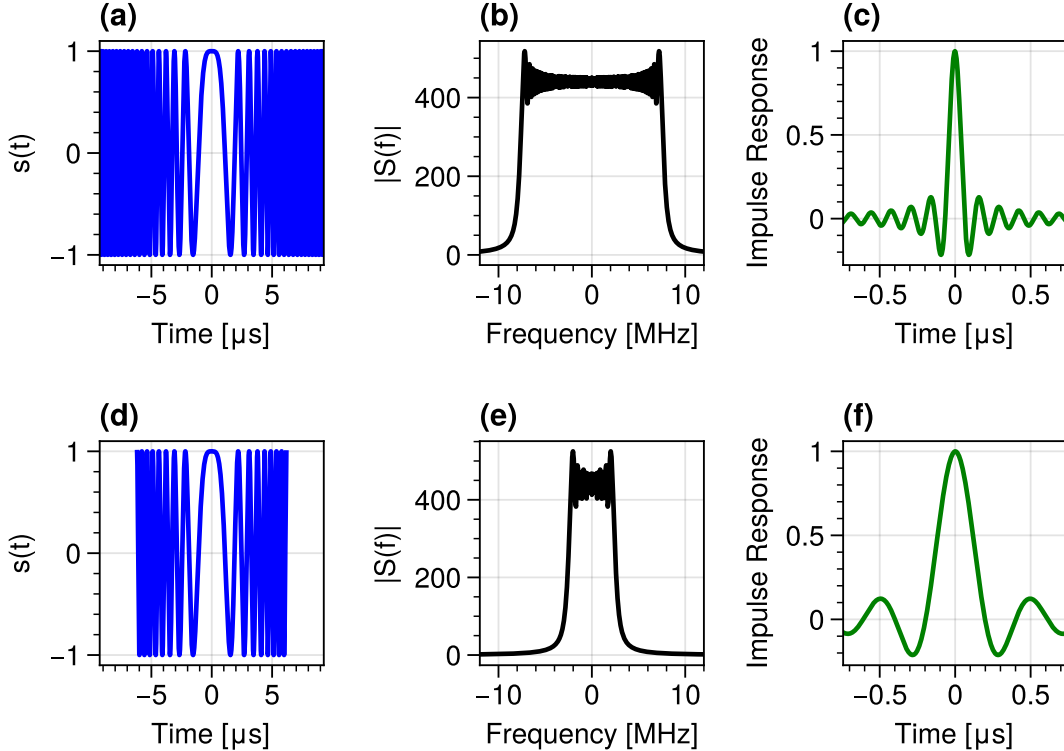
Figure 2.4: (a) The real part of a linear frequency-modulated chirp with a duration of $\tau \approx 37.12\mu s$ and a chirp slope $k = 4 \times 10^{11} Hz/s$. (b) The magnitude of the Fourier transform of the chirp is approximately a rectangle function, which shows the chirp bandwidth $BW = k\tau \approx 15.5$ MHz. (c) Matched filtering of the returned echo from one point scatterer yields the impulse response, which shows the approximate 10 meters of range resolution (or $\sim$65 ns in time). (d) For a chirp with the same slope k and $1/3$ the duration τ the frequency bandwidth is also cut by $1/3$ (e), the corresponding impulse response (f) and range resolution is 3 times worse.

In the azimuth direction, the size of the radar footprint determines which ground points can be distinguished from the echo of one pulse; this is known as the *real aperture radar* (RAR) resolution. The footprint size can be written as $r\lambda/L$, where r is the target range, L is the along-track antenna length, and λ is the radar wavelength.

The earliest imaging radar platforms were limited to this resolution in azimuth. For an airborne platform with a 1 meter antenna imaging at C-band, this would be a $\sim$600 meter resolution. Note that for some applications, such as military detection applications or wide-area ocean mapping, this azimuth resolution is sufficient (Simons and Rosen, 2007); however, the RAR resolution for spaceborne radars is on the order of 10s of kilometers, which is far too coarse for most applications.

The resolution in azimuth is greatly improved by creating a *synthetic aperture*, which is a technique that focuses the image using a series of reflected echoes (Figure 2.5). Coherent processing (i.e. using both magnitude and phase) is possible by carefully tracking each target's phase history, $\phi(t)$, which is related to the range to the target $r(t)$:

$$\phi(t) = -\frac{4\pi}{\lambda} r(t) \,. \tag{2.1}$$

There are multiple signal processing algorithms which use the target's phase history to create a synthetic aperture. One of the first developed and most widely today used is the range-Doppler algorithm (RDA) (Wu, 1976, Cumming and Bennett, 1979). RDA uses the apparent shift in Doppler frequency due to the platform motion to create a matched filter in azimuth, similar to the matched filter used for range compression (Cumming and Wong, 2004). An alternative to RDA is time-domain backprojection (Duersch, 2013), which provides a more exact phase compensation at the cost of being more computationally expensive. The backprojection algorithm collects the energy from every radar pulse containing a ground point and compensates for the range-dependent phase. The complex-valued radar image S (also known as a *single-look complex* image, or SLC) at pixel location (x, y) can be formed by summing over all pulses and applying for a range-dependent term to cancel the propagation phase:

$$S(x, y) = \sum_k s_k (t_k) \, e^{j \frac{4\pi}{\lambda} r_k(x,y)} \tag{2.2}$$

where $j = \sqrt{-1}$, $r_k(x, y)$ is the range distance from the radar sensor to the point (x, y) at the time of the kth pulse, $s_k(t_k)$ is the complex value of the kth range-compressed pulse at time $t_k = r_k(x, y)/c$, and c is the speed of light (Zebker, 2018). If the radar imaging geometry is known precisely so that r_k can be computed for all pulses, the coherent summation can be performed for each pixel to focus the SAR image.

14
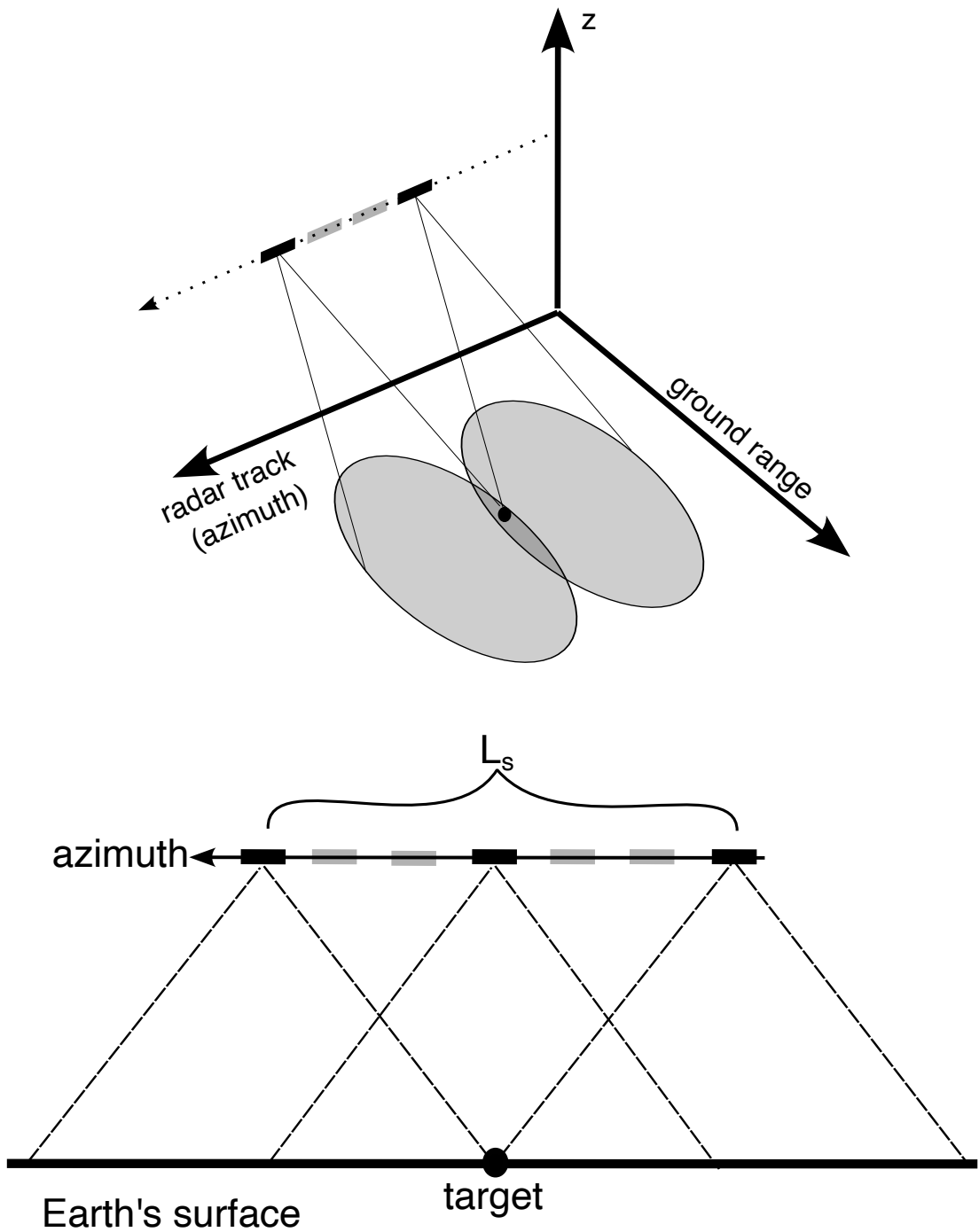
Figure 2.5: (Top) One point on the ground is illuminated by a series of pulses (only first and last pulses shown here). (Bottom) Side view of a series of pulses illuminating a target. Coherently processing all pulses forms synthetic aperture of length L_s.

For all image formation methods, the final achievable azimuth resolution δ_{az} is

$$\delta_{az} = \frac{L}{2} \tag{2.3}$$

where L is the physical antenna length in the azimuth direction. Since typical space-borne satellites have antenna lengths on the order of 5-10 meters, the resulting δ_{az} is around 2.5-5 meters. The intuition behind this surprising result is that, unlike with RAR, a smaller physical antenna size L leads to a wider angular beam width λ/L. This means that a given target is illuminated for a longer time, leading to a greater number of pulses to coherently process. Thus, the azimuth resolution will actually improve with a smaller antenna size.

2.3 SAR Interferometry

Interferometric Synthetic Aperture Radar (InSAR) refers to a broad class of applications that exploit the phase difference between two SAR images to obtain extra information beyond the 2D locations of points (Bamler and Hartl, 1998). The most common applications are generating topography maps (Graham, 1974, Zebker and Goldstein, 1986) and mapping surface deformation (Goldstein and Zebker, 1987, Gabriel et al., 1989, Li and Goldstein, 1990, Massonnet et al., 1993, Rosen et al., 2000). The InSAR measurement is made after precisely coregistering and resampling two SLC images S_1 and S_2 to the same coordinates. The measurement $I_{1,2}$ is formed by multiplying each pixel of the first SLC S_1 by the complex conjugate of the second S_2:

$$I_{1,2} = S_1 S_2^* = A_1 A_2 e^{j\Delta\phi_{1,2}} \tag{2.4}$$

where $S_k = A_k e^{j\phi_k}$, A_k is the amplitude of the kth image, and the phase $\phi_k = -\frac{4\pi}{\lambda} r_k$. The image I is called an *interferogram*, and the quantity $\Delta\phi_{1,2} \triangleq \phi_1 - \phi_2$ is the interferometric phase.

For topography mapping, two SAR antennas are separated by a distance in the across-track direction and each acquires a SAR image simultaneously[2] (Figure 2.6). The baseline causes the two radars to view the same point on the ground with a slight

---

[2]The acquisitions can also be at different times, under the assumption that no ground deformation has occurred.
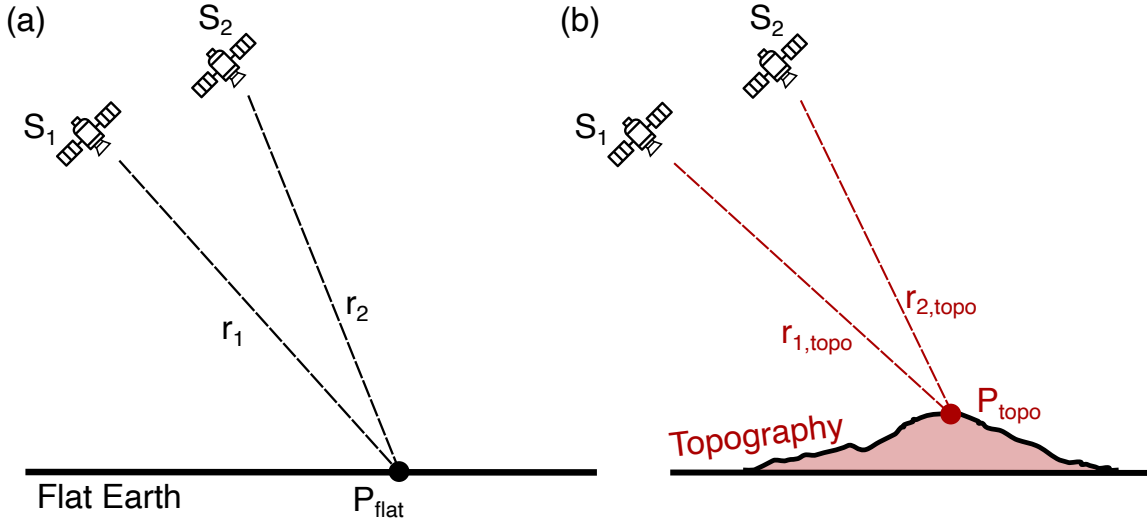
Figure 2.6: InSAR imaging geometry for topography mapping. Two SAR images, S_1 and S_2, are acquired with a slight spatial separation. The measured phase difference between S_1 and S_2 will change depending on whether we are viewing a point (a) on a flat Earth reference, or (b) at some topographic height. The this allows us to use the phase difference to infer the height of P_{topo} above the reference Earth location P_{flat}.

change in angle. The difference in phase $\Delta\phi$ between S_1 and S_2 is related to the difference in the geometrical path length from each radar to the ground. This means that $\Delta\phi$ changes based on whether the satellites are viewing flat ground (Figure 2.6a) or topography (Figure 2.6b). Thus, with precise knowledge of the viewing geometry, the height of the topography can be inferred from the interferometric phase for each point in the interferogram (Simons and Rosen, 2007).

The first widely successful InSAR topography mission was the 11-day SRTM in 2000 (Figure 2.1). The SRTM deployed one radar attached to the body of the Space Shuttle Endeavour and one receive-only radar at the end of a 60 meter retractable mast. The SRTM produced elevation data with 30-meter resolution for all Earth land surface from -60° to 60° latitude. More recently, the TanDEM-X mission by DLR produced a global DEM in 2016 with 12 meter pixels and 2 meter vertical accuracy using two identical satellites flying in formation. However, the TanDEM-X DEM is not publicly available like the SRTM DEM.

In repeat-pass InSAR (sometimes called *differential* InSAR, DInSAR, or occasionally DIfSAR), a radar platform acquires two SAR images over an area at different times, t_1 and t_2 (Figure 2.7). Assuming that the topography is known and can be
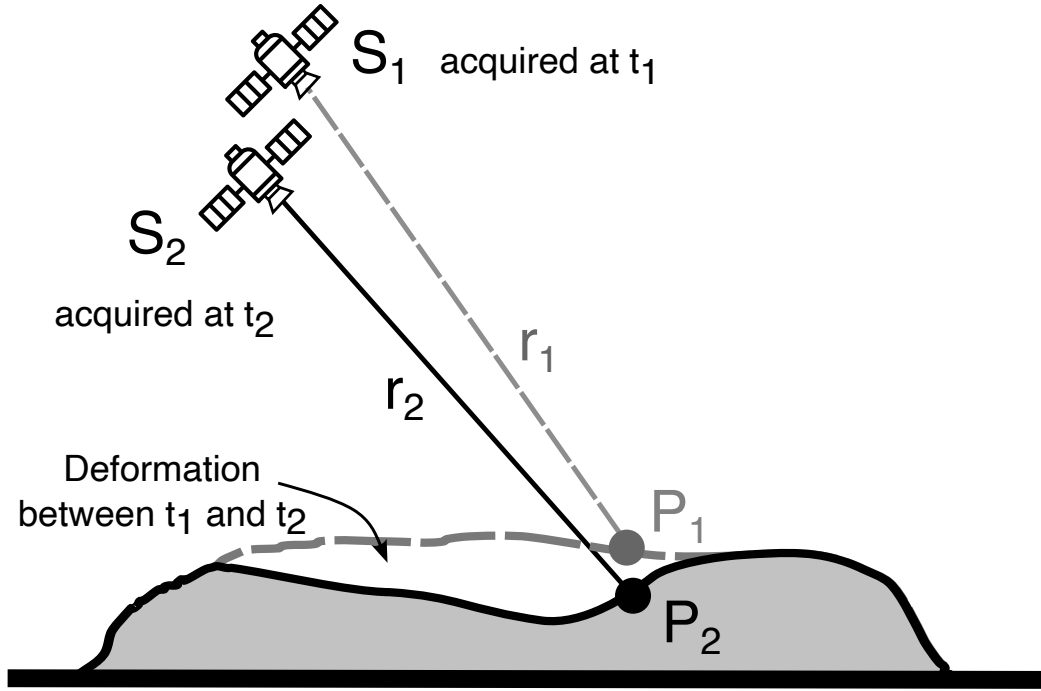
Figure 2.7: InSAR imaging geometry for deformation mapping. (a) Two SAR images, S_1 and S_2, are acquired at different times, before and after a ground deformation event. After removing the contribution from topography, the change in range between times t_1 and t_2 results in a measured phase change $\Delta\phi_{1,2} = \frac{4\pi}{\lambda}(r_2 - r_1)$.

removed from the phase measurement, the remaining InSAR phase at each pixel measures the change in range along the radar LOS direction:

$$\Delta\phi_{1,2} = \frac{4\pi}{\lambda}(r_2 - r_1) \tag{2.5}$$

Since the measurement uses the phase of the propagated radar waves, it is only known modulo 2π; the process of obtaining the full continuous phase is known as *phase unwrapping* (Goldstein et al., 1988, Chen and Zebker, 2001). Note that even after phase unwrapping, the absolute number of 2π cycles from the radar to the ground is not known; thus, an unwrapped interferogram represents the surface deformation *relative* to some point that is assumed to be zero. Additionally, the description of the interferometric phase in Equation (2.5) assumes no noise; in reality there are numerous noise sources which affect either the phase of an individual SAR acquisitions or the phase difference between pairs of images.

18

2.4   InSAR Noise Sources

After removing phase contributions from topography and satellite geometry, the phase at each pixel in an interferogram formed from SLCs S_1 and S_2 can be written as

$$\Delta\phi_{1,2} = \frac{4\pi}{\lambda}\left(\Delta d_{1,2} + \Delta\alpha_{1,2}\right) + \Delta\phi_{iono} + \Delta\phi_{orb} + \Delta\phi_{dem} + \Delta\phi_{decor} + \Delta\phi_{unwrap} + \Delta\phi_{scat} + \Delta\phi_n,$$
(2.6)

where λ is the radar wavelength and $\Delta d_{1,2}$ is the surface deformation between S_1 and S_2 along the radar LOS direction.

The term $\Delta\alpha_{1,2} \triangleq \alpha_2 - \alpha_1$ represents tropospheric noise arising from differences in excess delay induced by the neutral atmosphere. Tropospheric noise is caused by atmospheric pressure, temperature, or water vapor changes between the two radar acquisitions (Zebker et al., 1997). Since tropospheric noise is the dominant noise for the West Texas study of Chapters 4-6, the noise is further detailed in the following section (Section 2.4.2).

Phase errors can also arise from variations in the index of refraction due to ionospheric heterogeneities, $\Delta\phi_{iono}$ (Gray et al., 2000). Since the ionosphere is a dispersive medium, the phase effects are dependent on radar frequency, with lower frequencies seeing more distortion. The effect at C-band is approximately 1/16 the effect at L-band (Liang et al., 2019). Additionally, the dependence on frequency enables mitigation techniques which split the radar spectrum into sub-bands to calculate phase corrections (Rosen et al., 2010).

The terms $\Delta\phi_{orb}$ and $\Delta\phi_{dem}$ represent systematic errors resulting from imprecise knowledge of the platform's orbital position or topographic height, respectively. Orbital errors usually appear as a planar phase ramp in stripmap acquisitions. Although these were common to see in ERS-1 or ENVISAT data, they rarely appear in Sentinel-1 data due to its high precision orbit determination (Fattahi and Amelung, 2014). Errors in the DEM used to remove the topographic phase result in a spatial baseline-dependent phase error (Fattahi and Amelung, 2013). These errors are often small in Sentinel-1 data due to the tight control of the repeat orbit tube, but they can be significant in mountains or regions with sharp topography changes.

Decorrelation errors, $\Delta\phi_{decor}$, arise from a loss of coherence of the phase between S_1 and S_2 due to changes in the surface dielectric properties or scattering characteristics

(Zebker and Villasenor, 1992, Michaelides et al., 2019, Ansari, 2018). The correlation can be estimated from the complex coherence γ of the interferogram (Bamler and Hartl, 1998)

$$\gamma = \frac{\langle S_1 S_2^* \rangle}{\sqrt{\langle S_1 S_1^* \rangle^2 \langle S_2 S_2^* \rangle^2}} \tag{2.7}$$

where S_2^* is the complex conjugate of S_2 and $\langle \cdot \rangle$ denotes the statistical expectation operator. The expectation is defined as an ensemble average, but in practice it is estimated using some spatial window of pixels. The magnitude of this quantity $\rho = |\gamma|$ is called the *correlation* (or sometimes called the coherence), and varies from 0, indicating a complete loss of signal coherence, to 1, indicating perfectly correlated radar echoes. When the correlation is very low, the phase unwrapping processing may fail and produce patches of pixels which have 2π offsets from the correct value. These are known as phase unwrapping errors, $\Delta\phi_{unwrap}$. For study areas which regularly have strong decorrelation (e.g. agricultural areas), the technique known as persistent scatterer interferometry is used to overcome decorrelation by locating the phase-stable pixels which maintain coherence over long periods of time (Ferretti et al., 2001, Agram, 2010, Hooper, 2006, Chen et al., 2016).

The term $\Delta\phi_{scat}$ represents phase introduced by changes to the surface and subsurface scattering properties. This term is separated from the random decorrelation noise, as recent studies have shown that systematic, non-random effects can occur from changes to subsurface dielectric properties (e.g. from changes to soil moisture) (Zan et al., 2014; 2015, Zwieback et al., 2015, Michaelides, 2020, Zheng et al., 2022). Finally, $\Delta\phi_n$ represents other residual noise terms, including thermal noise from the radar antenna system, that are typically an order of magnitude smaller than the other errors listed.

Although these effects have been presented as noise sources for deformation monitoring applications, each one can be a signal of interest in other InSAR applications. For example, the phase variations from the troposphere have been used for atmospheric mapping and meteorological purposes (Hanssen et al., 1999, Liu, 2012). Additionally the presence of decorrelation indicates a change to the scattering surface properties and can be used for coherent change detection (Simons and Rosen, 2007, Jung et al., 2016). Several efforts have attempted to use the $\Delta\phi_{scat}$ term to invert for changes to soil moisture (Zwieback et al., 2017, Zan and Gomba, 2018).

2.4.1   Visualizing Common Noise Sources

In high signal-to-noise ratio (SNR) interferograms (e.g. large magnitude earthquakes such as Massonnet et al. (1993)), one can estimate the deformation magnitude by simply "counting the fringes", where the number of 2π cycles is estimated and converted to centimeters through the factor $\lambda/2$ (the wavelength is divided in half due to the two-way radar travel). However, it is more common for an interferogram to contain many visual features corresponding to noise terms in Equation (2.6). These noise sources can often be visually identified by InSAR experts, but they can add considerable difficulty for newer users without background knowledge of the study area.

To illustrate several common noise sources, Figure 2.8 shows a Sentinel-1 interferogram of the Big Island of Hawaii from April 20th, 2018 to May 2nd, 2018. This time period spans the beginning of the 2018 Kilauea eruption, during which a large subsidence event occurred from subsurface magma flow. However, the diversity in weather conditions, topography, and vegetation lead to many noise artifacts in most interferograms of Hawaii. For example, the coastal region in Figure 2.8b contains dense fringes which could be mistaken as deformation, but in fact is due to turbulent tropospheric noise. The large elevation changes on Mauna Loa and Mauna Kea in the center of the island lead to stratified tropospheric noise, which creates a concentric ring pattern (Figure 2.8c) that is the same shape as a subsidence bowl (see Section 2.4.2). An example of decorrelation noise occurs on the windward side of the island (Figure 2.8d), which contains many dense tropical rain forests (Figure 2.8e).

Finally, a real deformation feature of $\sim 30-40$ cm occurred near the Pu'u 'Ō'ō volcanic cone (Figure 2.8f). In this case, the ground sank down and to the southeast as magma flowed away from Pu'u 'Ō'ō (Figure 2.8g). One can estimate the magnitude of subsidence by counting the number of cycles in the zoomed-in region of the interferogram (Figure 2.8f) and multiplying by $\lambda/2 = 2.8$ cm. However, even this analysis can be difficult due to the high spatial frequency of the fringes, which can cause aliasing of large deformation events. For the Hawaiian case here, the deformation magnitude can be verified using nearby permanent GPS stations.
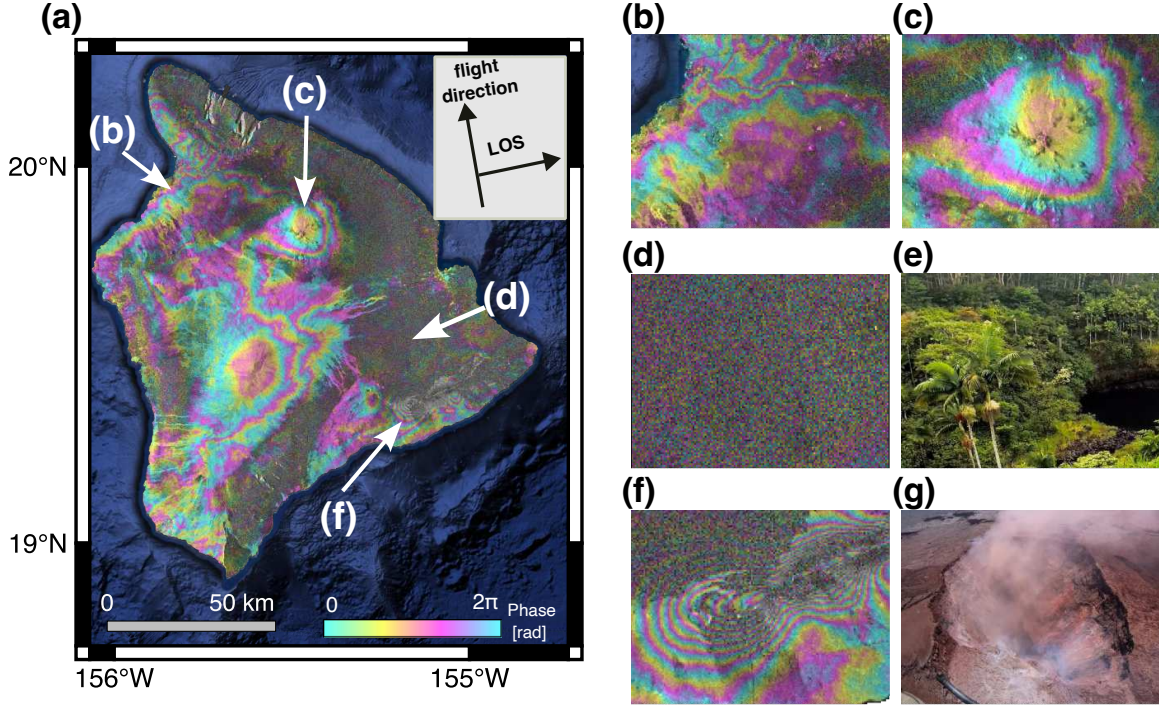
Figure 2.8: (a) Sentinel-1 interferogram (ascending path 124) from April 20th, 2018 to May 2nd, 2018 over Hawaii, spanning the beginning of the 2018 Kīlauea eruption. Each colored phase cycle of 2π radians indicates a range change of 2.7 cm along the radar line-of-sight, which can be caused by real surface deformation or a noise source. (b) The dense fringes near the coast are caused by turbulent tropospheric noise (see Section 2.4.2). (c) Stratified tropospheric noise on the peak of Mauna Kea, the tallest peak in Hawaii at 4,207 m, causes a concentric ring pattern. This pattern is also visible on Mauna Loa in the center of the island, where the phase is strongly correlated with topographic height. See Section 2.4.2 for further details. (d) An example of decorrelation noise caused by dense tropical rain forests (e) located on windward side of the island. (f) Real deformation of $\sim 30 - 40$cm around the Pu'u 'Ō'ō volcanic cone to the east of Kīlauea. In this case, the ground was subsiding down and to the southeast as magma flowed away from Pu'u 'Ō'ō. (g) An aerial photo of Pu'u 'Ō'ō shows the caldera collapse on April, 30th, 2018 after magma migrated eastward underground (image source: HVO / USGS).

22

2.4.2 Tropospheric Noise

The conversion between phase and two-way distance from ground to satellite in Equation (2.1) assumes that the electromagnetic waves travel though a homogeneous medium with constant velocity. In reality, they travel through the atmosphere which has a variable index of refraction n, where n relates to the phase velocity v and speed of light in a vacuum c by $n = c/v$ (Zebker et al., 1997, Hanssen, 2001, Liu, 2012). Since n is always real and slightly greater than 1 for Earth's neutral atmosphere, it is more common to describe fluctuations using the *refractivity* $N = 10^6(n-1)$, which is the additional refractive index beyond unity. Writing N as $N(x, y, z)$ to emphasize the 3D variation, we can express the excess delay D caused by the propagation through the atmosphere as

$$D = 10^{-6} \int_s N(x, y, z) ds \tag{2.8}$$

where ds is the incremental slant length, and the integration runs along the radar line of sight. The excess delay adds a phase of $\phi = -\frac{4\pi}{\lambda}D$ to a radar image acquired with the given atmospheric conditions.

The refractivity of the troposphere is commonly decomposed into hydrostatic, wet, and liquid components (Hanssen, 2001, Bekaert et al., 2015a):

$$N = \left(k_1 \frac{P}{T}\right)_{\text{hyd}} + \left(k_2' \frac{e}{T} + k_3 \frac{e}{T^2}\right)_{\text{wet}} + (k_4 W)_{\text{liquid}} \tag{2.9}$$

where P is the total atmospheric pressure in hPa, T is the atmospheric temperature in Kelvin, e is the partial pressure of water vapor in hPa, and W is the liquid water content of clouds in g/m^3 The coefficients k_1, k_2', k_3 and k_4 are constants estimated from laboratory measurements, commonly taken to be $k_1 = 77.6$, $k_2' = 23.3$, $k_3 = 3.75 \cdot 10^5$, and $k_4 = 1.45$ from Smith and Weintraub (1953) and Solheim et al. (1999). The hydrostatic delay is on the order of a few meters; however, it varies slowly laterally and it is often assumed to be vertically stratified (i.e. varying only with elevation) for study areas roughly 50×50 km or less (Doin et al., 2009). The wet component, caused by variations in water vapor content, is smaller in absolute terms ($\sim$ 10s of centimeters) but has significant lateral variations at short length scales. The delay from the liquid component is often negligible (1-2 millimeters or less) but can be several centimeters in the presence of tall cumulonimbus clouds (Liu, 2012).
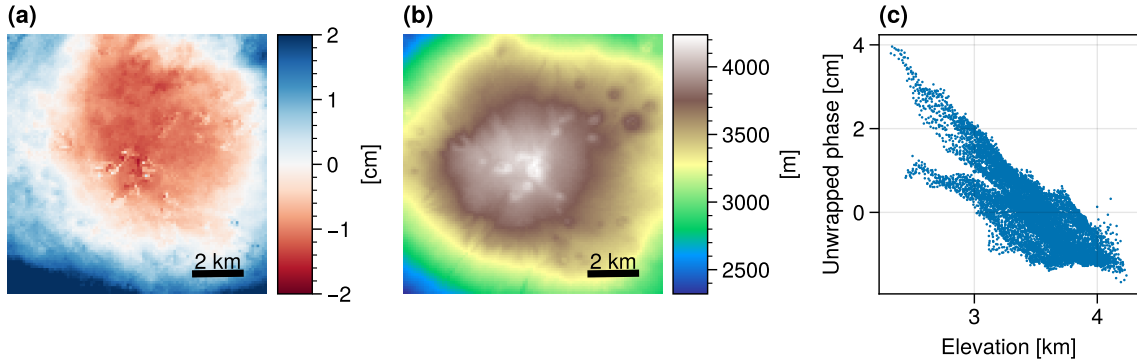
Figure 2.9: (a) Unwrapped interferogram from Figure 2.8c, zoomed in to the top of Mauna Kea. (b) The SRTM DEM heights for same area as panel (a). (c) Scatterplot of unwrapped phase (in cm) from panel (a) vs heights from panel (b).

For the purposes of InSAR analysis, noise from tropospheric delay is usually divided into a stratified component, which correlates with height (Hanssen, 2001, Doin et al., 2009), and a turbulent component that is random at time scales longer than a day (Emardson et al., 2003, Onn, 2006).

Previous studies have advanced correction techniques for the stratified component of tropospheric noise. Several empirical approaches have fit linear or power-law relationships between the unwrapped phase and topographic height of coherent pixels within interferograms (Elliott et al., 2008, Lauknes, 2011, Bekaert et al., 2015b, Zebker, 2021, Murray et al., 2021). Under the assumption that the deformation does not correlate with topography, these approaches can be effective and simple to implement. For example, Figure 2.9 shows the portion of the unwrapped interferogram on top of Mauna Kea from Figure 2.8c. Although the interferogram appears to show a bowl shape deformation (Figure 2.9a), the phase is actually closely correlated with the topography (Figure 2.9b-c). Fitting and removing a linear trend from the phase vs. elevation plot mitigates the stratified atmospheric noise in this case. However, these approaches can be less effective in regions with multiple weather patterns where the phase-elevation correlation can vary dramatically in space (Murray et al., 2021).

Many efforts have advanced stratified noise corrections using auxiliary sources of data, including global atmospheric models (GAMs) (Doin et al., 2009, Jolivet et al., 2011; 2014, Cao et al., 2021), GPS zenith delay measurements (Onn, 2006, Yu et al., 2017), and external satellite measurements from sensors such as the Moderate

Resolution Imaging Spectroradiometer (MODIS) (Li, 2005, Barnhart and Lohman, 2013) or the Medium Resolution Imaging Spectrometer (MERIS) (Ding et al., 2008). Several authors have attempted to create off-the-shelf correction services or toolboxes from these data sources. For example, Yu et al. (2018b) combined information from GAMs and available GPS zenith delay measurements to create the Generic Atmospheric Correction Online Service (GACOS) for estimating tropospheric noise in InSAR data. Maurer et al. (2021) created a library for ray-tracing the LOS paths through GAM-predicted delays to create correction products. While these correction methods show promise in certain study areas, the spatial and temporal resolution can be too low to correct for noise from severe weather or turbulent mixing of water vapor (e.g. Section 3.3) (Murray et al., 2019). Therefore, methods for mitigating the turbulent tropospheric noise often analyze many interferograms over time and exploit the uncorrelated temporal characteristics of the noise.

2.5   InSAR Time Series

Since certain noise sources cannot be distinguished from deformation in a single interferogram (e.g. Figure 2.8), it is common to analyze multiple interferograms using InSAR time series techniques (sometimes called "multi-temporal InSAR" or MT-InSAR). Most multi-temporal methods belong to one of the following categories: 1) stacking (averaging) (Zebker et al., 1997, Sandwell and Price, 1998), 2) small-baseline approaches (Berardino et al., 2002), or 3) persistent scatterer (PS) methods (Ferretti et al., 2001, Hooper, 2006). In the past decade, a fourth category of "phase-linking" approaches have been popularized by the SqueeSAR algorithm (Ferretti et al., 2011); these are based on optimizations or decompositions of the complex covariance matrix of SAR image stacks (Guarnieri and Tebaldini, 2008, Fornaro et al., 2015, Ansari, 2018). Methods (3) and (4) have shown success in extracting high-precision estimates of interferometric phase where decorrelation is the dominant noise source (e.g. in local, high-rate deformation, (Tebaldini and Guarnieri, 2010)); in the following section, we focus on (1) and (2).

For deformation signals which occur as a transient event or with a constant rate, stacking consists of averaging multiple interferograms (possibly with different weights for each interferogram) which all contain the deformation signal (Simons and Rosen,

2007, Zheng, 2019). For example, suppose an earthquake occurred at a known date, and we have a set of M interferograms which all span this date. For each ground pixel, we can collect the phase difference measurements into a vector $\Delta\phi \in \mathbb{R}^M$. To estimate the coseismic displacement θ, the simplest stacking solution is

$$\theta = \frac{\lambda}{4\pi} \frac{1}{M} \sum_i^M \Delta\phi_i, \tag{2.10}$$

where $\Delta\phi_i$ is ith element of the measurement vector, and the factor $\frac{\lambda}{4\pi}$ converts the phase from radians to centimeters. For constant-rate ground deformation, one approach based on (Sandwell and Price, 1998) to calculate the average LOS velocity v_{avg} of each ground pixel is to compute

$$v_{avg} = \frac{\lambda}{4\pi} \frac{\sum_i \Delta\phi_i}{\sum_i \Delta t_i} \tag{2.11}$$

where Δt_i is the temporal baseline of the ith interferogram (i.e. the time span $t_k - t_j$ for interferogram $\Delta\phi_{j,k}$).

The Small Baseline Subset (SBAS) approach from Berardino et al. (2002) formulates a linear estimation problem to solve for the phase at each SAR acquisition. Suppose that the M interferograms are formed from N SAR acquisitions, where $\frac{N}{2} \leq M \leq \frac{N(N-1)}{2}$, and all interferograms have been unwrapped and zero-referenced to a common location. To solve for the LOS phase delay for each SAR acquisition $\phi = [\phi_0, \phi_1, \ldots, \phi_{N-1}]^T$, we write the functional model of the linear system as

$$A\phi = \Delta\phi + \epsilon. \tag{2.12}$$

where A is the system design matrix, and ϵ is the vector of interferogram-specific noise sources (e.g. $\Delta\phi_{decor}, \Delta\phi_{unwrap}, \Delta\phi_{scat}, \Delta\phi_n$ from Equation (2.6)). The matrix A is an incidence-like matrix where the row corresponding to measurement $\Delta\phi_{j,k} \triangleq \phi_k - \phi_j$ has 1 in the kth column and -1 in the jth column. Since interferograms are relative measurements, the first date's phase cannot be constrained and is conventionally taken to be $\phi_0 = 0$. Therefore, we omit the first column of the A matrix containing -1 entries corresponding to ϕ_0, leaving $N-1$ remaining terms in the unknown vector $\phi = [\phi_1, \ldots, \phi_{N-1}]^T$. When A is full column rank, the solution for ϕ can be obtained

through least squares, $\boldsymbol{\phi} = (\boldsymbol{A}^T\boldsymbol{A})^{-1}\boldsymbol{A}^T\boldsymbol{\Delta\phi}$, equivalent to minimizing the L_2 norm of the residual vector $\|\boldsymbol{A\phi} - \boldsymbol{\Delta\phi}\|_2^2$.

A common alternative to Equation (2.12) is to solve for the phase velocity between each SAR acquisition $\boldsymbol{v} = [v_1, \ldots, v_{N-1}]^T$ where $v_i = (\phi_i - \phi_{i-1})/(t_i - t_{i-1})$. The linear system is now written as

$$\boldsymbol{Bv} = \boldsymbol{\Delta\phi} + \boldsymbol{\epsilon}, \tag{2.13}$$

where the row of $\boldsymbol{B}$ corresponding to measurement $\Delta\phi_{j,k}$ has $t_i - t_{i-1}$ in columns i for $j < i \leq k$, and 0 elsewhere. After solving Equation (2.13), $\boldsymbol{v}$ is integrated to obtain $\boldsymbol{\phi}$.

The rationale behind solving for $\boldsymbol{v}$ is that for early SAR satellites, such as ERS-1 and ERS-2, the acquisitions are often grouped as subsets of images with small spatial baselines that are separated from other groups by large temporal or spatial baselines. When $\boldsymbol{\Delta\phi}$ contains an isolated subset of interferograms, A is not full column rank and Equation (2.12) is solved with a pseudo-inverse, $A^\dagger$, generated using the singular value decomposition (SVD) (Strang, 2006). The SVD approach for rank-deficient systems produces a minimum norm solution vector. The authors of Berardino et al. (2002) found that minimizing the norm of the velocity vector $\boldsymbol{v}$ produced more physically plausible deformation results than minimizing the norm of $\boldsymbol{\phi}$. We note that for recent missions like Sentinel-1 with tightly controlled repeat orbits, it is often possible to create a single connected network of interferograms, leading to equivalent results from the formulations of Equations (2.12) and (2.13). However, Equation (2.13) enables alternative regularization strategies for inversion, as shown in Section 4.1.1.

2.6 InSAR Processing Chain

We developed software for an efficient and scalable InSAR processing chain to process geocoded SLC images and output cumulative surface deformation maps (Figure 2.10). An area of interest (AOI) is chosen in latitude and longitude coordinates, and all overlapping Sentinel-1 SLC products from a specified time frame are downloaded from the Alaska Satellite Facility (ASF) Distributed Active Archive Center (DAAC). The 30-meter SRTM DEM is downloaded over the AOI (stitching together tiles for regions larger than 1 x 1 degree) and upsampled (JPL, 2013) . The DEM, along with ESA's precise orbit files, are used by the Stanford processor (Zheng and Zebker,
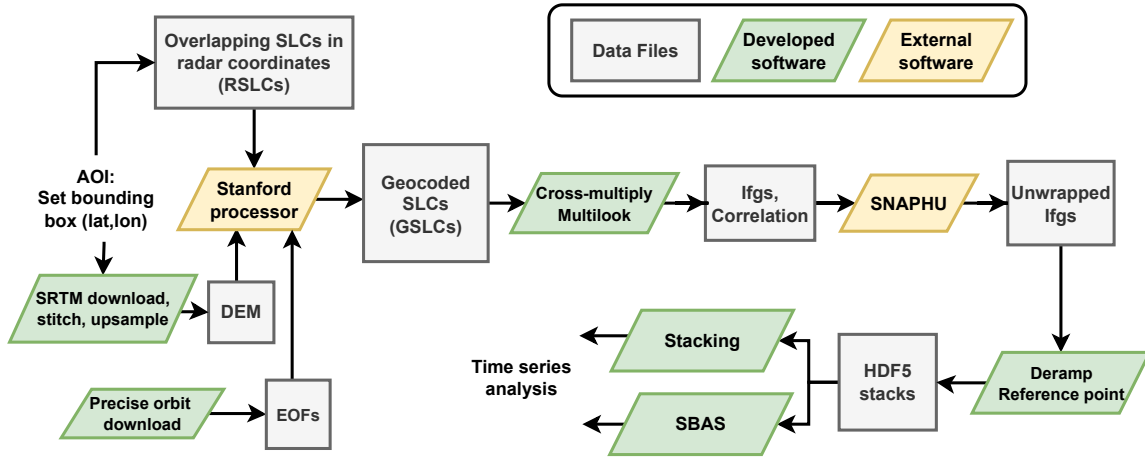
Figure 2.10: Processing chain used to create geocoded unwrapped of interferograms for stacking or SBAS time series analysis. Grey boxes indicate intermediate data products, yellow parallelograms indicate externally developed software packages, green parallelograms indicate software written for this thesis.

2017, Zebker, 2017) to produce topography corrected, geocoded SLCs (GSLCs). We note that working with GSLCs simplifies workflows for merging multiple Sentinel-1 frames over large areas (Zheng, 2019). Interferograms are formed from the GSLCs through a pixel-wise cross multiplication (Equation (2.4)), which are then unwrapped using the Statistical-cost, Network-flow Algorithm for Phase Unwrapping (SNAPHU) (Chen and Zebker, 2001). The unwrapped interferograms are referenced and (optionally) denoised by removing a planar or quadratic phase ramp. These are finally saved using the Hierarchical Data Format 5 (HDF5) data format, which allows user-defined metadata, data chunking, and compression. HDF5 also simplifies and accelerates parallel implementations of pixel-wise SBAS algorithms (used in Chapter 4 and 5).

Chapter 3

Permian Basin Background

In this chapter, we review the scientific background of the induced seismicity problem. We describe the geodetic datasets available to study the problem, and we present strategies and challenges for processing Sentinel-1 InSAR data over West Texas. We demonstrate that tropospheric noise is the dominant InSAR noise source.

3.1 Shale Development and Induced Seismicity

Texas has been a leading producer of oil and gas for over a century (Frohlich et al., 2016a, The Academy of Medicine and of Texas, 2017). It became the nation's largest producer of crude oil after the first successful vertical well was drilled south of Beaumont, TX in 1901. These "conventional" wells were the primary mode of production in multiple oil fields across the state. It wasn't until the early 2000s that advances in horizontal drilling and hydraulic fracturing (also known as fracking, Figure 3.1) opened up vast new shale resources which were previously unworkable (Waters et al., 2006). For example, the Wolfcamp shale in Texas' Permian Basin is the largest continuous oil field that has ever been discovered in the United States, containing 20 billion barrels of oil and 16 trillion cubic feet of gas (Gaswirth and Marra, 2016). While areas of the Wolfcamp shale in the Midland Basin have been traditionally developed using vertical wells, the ability to extend subsurface drilling horizontally (Figure 3.1b) and increase production using enhanced oil recovery (EOR, Figure 3.1d) allowed many new areas to be economically viable for oil and gas production (Figure 3.2).

Despite the economic benefits that the new production technologies provided for Texas, concerns have been raised about possible environmental consequences of shale development (The Academy of Medicine and of Texas, 2017, Scanlon et al., 2020). One concern is the triggering of seismic activity, as it has been recognized that injection or withdrawal of fluids from the subsurface can induce earthquakes along existing faults (Ellsworth, 2013, Simpson et al., 1988). Note that induced earthquakes are not limited to oil and gas operations (Grigoli et al., 2017, Foulger et al., 2018, van der Baan and Calixto, 2017); they have also been associated with geothermal energy development (Deichmann and Giardini, 2009), mining operations (Hasegawa et al.,
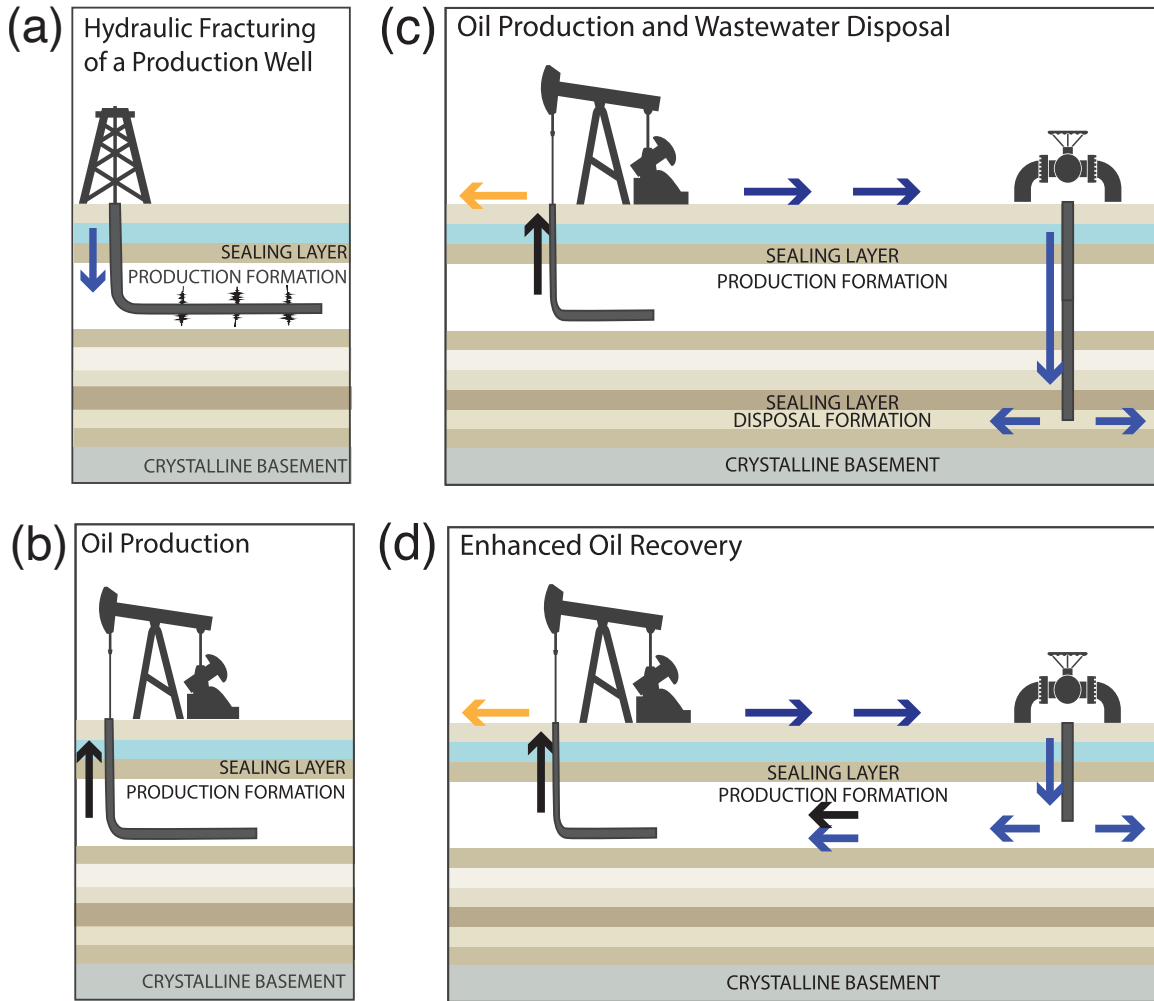
Figure 3.1: Simplified diagrams of oil-field operations. Arrows show the directions of fluid being injected or withdrawn. Arrow color indicates the contents of the fluid: black (oil, gas, and wastewater), yellow (oil and gas), and blue (wastewater). (a) In a hydraulic fracturing operation, fluids are injected at high pressure into a production well, causing fractures in the surrounding rock that increase permeability. Increased permeability allows the extraction of oil or gas from a larger region. Following the hydraulic fracturing of a well, the well goes into production (b). (c) Production wells extract oil and gas, and as a byproduct, salt water (commonly called "produced water" or "wastewater"), which is injected to a different subsurface formation at a disposal well. (d) Enhanced oil recovery (EOR), an alternative to wastewater disposal, involves injecting the water back into the formation holding the oil and gas to sweep oil and gas toward the production well. (Figure adapted from (Rubinstein and Mahani, 2015))
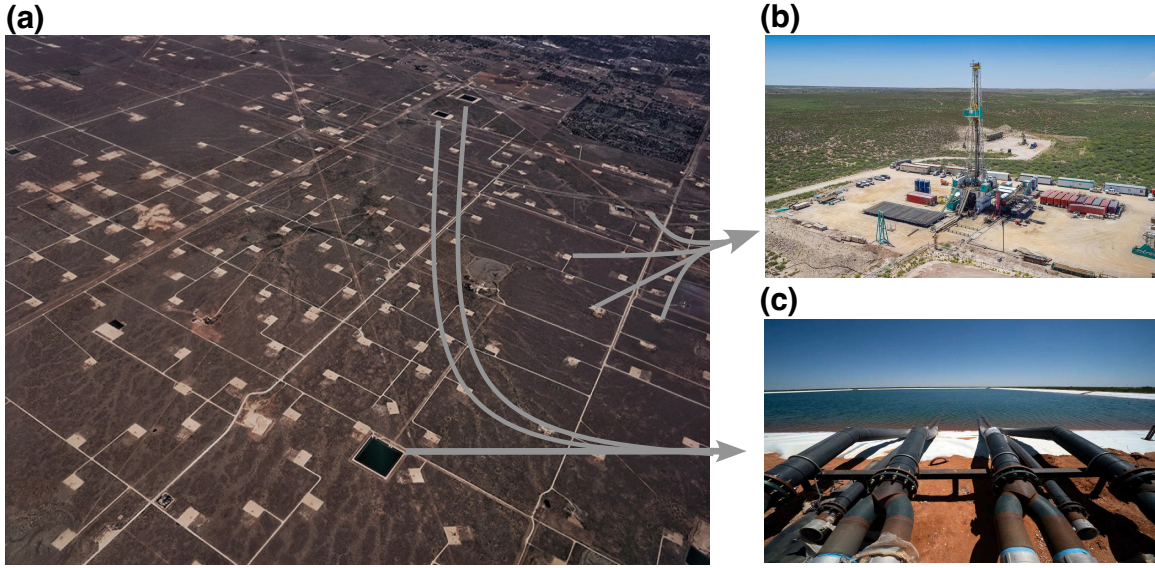
Figure 3.2: (a) Aerial view of drilling pads throughout the Permian Basin (b) Drilling rig set up on one pad (Source: XTO Energy) (c) Water condensate pit used to store fresh water condensed from natural gas or other flowback fluids (photo source: Benjamin Lowy)

1989), water impoundment in reservoirs (Talwani, 1997), and CO_2 sequestration (Gan and Frohlich, 2013).

One conceptual model for triggering earthquakes uses the Mohr-Coulomb failure criterion (Hubbert and Rubey, 1959). The critical shear stress $\tau_{critical}$ required to promote fault slippage can be written as

$$\tau_{critical} = \tau_0 + \mu(\sigma_n - P) \tag{3.1}$$

where τ_0 is the cohesive strength of the sliding surface (often negligible), μ is the coefficient of friction, σ_n is the normal stress, P is the pore pressure (Nicholson and Wesson, 1990, Ellsworth, 2013). Intuitively, increasing the shear stress or decreasing the normal stress "unclamps" the fault and encourages failure (Shearer, 2019). Since increasing pore pressure lowers the effective normal stress, fluid injection can move critically stressed faults to failure and cause earthquakes (Figure 3.3a). Alternatively, poroelastic effects from injection can change the loading conditions on a fault without a direct hydraulic connection, which can cause fault failure through increased differential stress (Figure 3.3b).
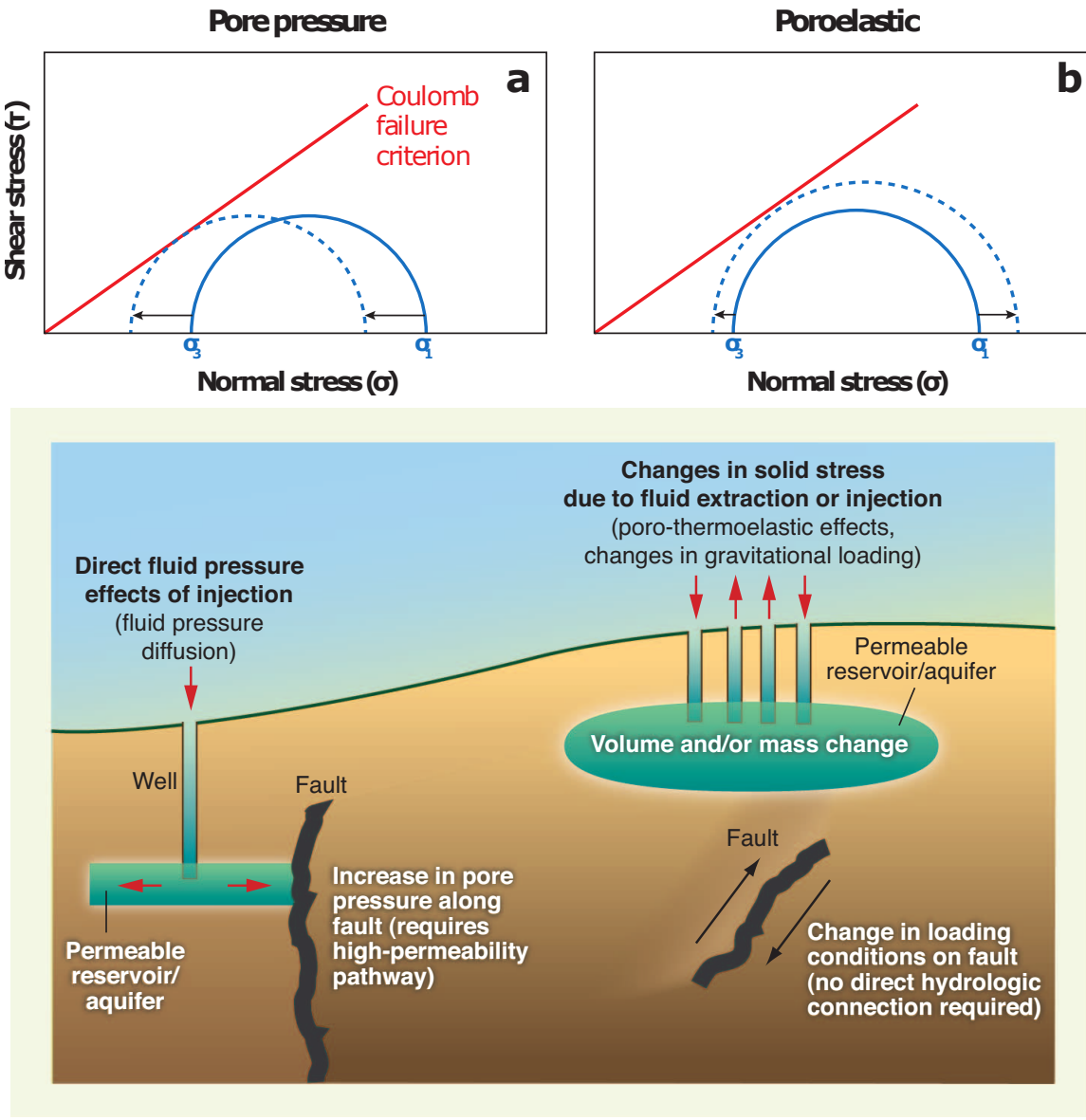
Figure 3.3: Effects of pore pressure perturbations and poroelastic stress changes on fault failure. Solid curves represent the initial stress state, and dashed curves represent the perturbed stress state. (a) Increased pore pressure reduces normal stress on the fault plane, moving the fault closer to the Coulomb failure criterion. (b) Poroelastic stresses increase differential stress. For both (a) and (b), pore pressure perturbations and stress changes, as well as the relative magnitude of changes, depend on parameters including time, distance, injection rate, diffusivity, and poroelastic parameters. (Bottom) Schematic diagram for each mechanism causing injection-induced earthquakes. (Top from Keranen and Weingarten (2018), bottom from Ellsworth (2013))

In Texas, earthquakes have occurred in close association with petroleum activities since 1925, but the rate of earthquakes in the last decade has increased over tenfold (Frohlich et al., 2016a, Skoumal et al., 2020a). To better understand the causes of these earthquakes and to assess the likelihood of infrastructure damage, the State of Texas funded the Texas Seismological Network (TexNet) to record earthquakes down to M2.0 across the state starting in 2017 (Savvaidis et al., 2019). By that time, there were over 130,000 active production wells, 23,000 active EOR wells, and nearly 3800 active saltwater disposal (SWD) wells in the Permian Basin (Figure 3.4 (a)). The volumes of petroleum production (Figure 3.4 (b, c)) and wastewater injection (Figure 3.4 (e, f)) have been rising in many locations; however, the recently cataloged earthquakes are spatially clustered (Figure 3.4 (c)). One significant cluster is near Pecos, TX in the Delaware Basin, which experienced over 2000 earthquakes in 2017 (Frohlich et al., 2019).

Several studies have used spatio-temporal analyses to link certain instances of wastewater injection and hydraulic fracturing to earthquakes (Savvaidis et al., 2020, Skoumal et al., 2020a, Grigoratos et al., 2020), but attributing causation of earthquakes to individual wells and discriminating induced from natural seismicity is extremely challenging (Grigoli et al., 2017, Dahm et al., 2012, Verdon et al., 2019, Frohlich et al., 2016a;b). Understanding the causes of earthquakes and how they are linked to certain production and disposal requires extensive knowledge of the subsurface. Subsurface measurements of pore pressure changes can be difficult or impossible to collect at a regional scale, but measurements of surface deformation derived from geodetic data have been a valuable tool in estimating the distribution of fault slip at depth and inferring associated seismic risk (Segall, 2010, Huang et al., 2017).

3.2 Available Geodetic Data

The coverage of GPS permanent stations in West Texas is sparse, and there are no stations in the Delaware Basin (Figure 3.5). At 14 stations in the Midland Basin and the Central Basin Platform, daily east, north, and up (ENU) surface deformation measurements were processed by the Nevada Geodetic Laboratory (Blewitt et al., 2018). After removing the regional tectonic motion, little motion (0-3 mm/year) was observed at all GPS stations over the study period (Figure 3.6). Because energy-
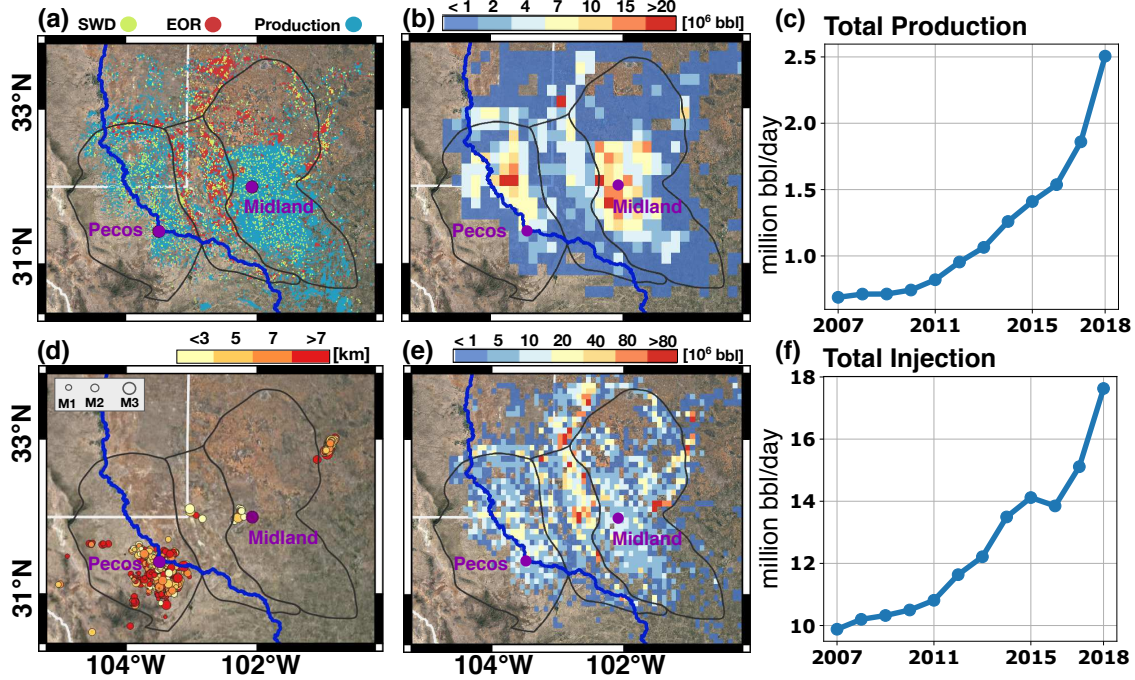
Figure 3.4: Shale development and seismicity in the Permian Basin through 2018. (a) Locations of oil production, EOR, and saltwater disposal (SWD) wells active in 2017. (b) Annual oil production volume on a 10-mile grid in 2017. (c) Permian Basin oil production rate as reported by the Texas Railroad Commission. (d) Locations of earthquake hypocenters detected by TexNet in 2017. The color and size of a circle indicates the estimated earthquake depth and magnitude. (e) Annual injection volume (including both SWD and EOR wells) on a 5-mile grid. (f) Permian region injection rate (including both SWD and EOR wells) as reported by the Texas Railroad Commission.

related injection and extraction activities often occur within deep and rigid subsurface formations, it has been common to assume little deformation can be detected at Earth's surface.

InSAR surface deformation measurements have much broader spatial coverage, and they provide a key observable to fill the gaps left by GPS. They allow us to estimate locations of pressure build up from fluid injection, barriers to subsurface fluid flow, and unmapped faults. However, creating accurate maps of surface deformation using InSAR can be challenging at the scale of the full Permian Basin.
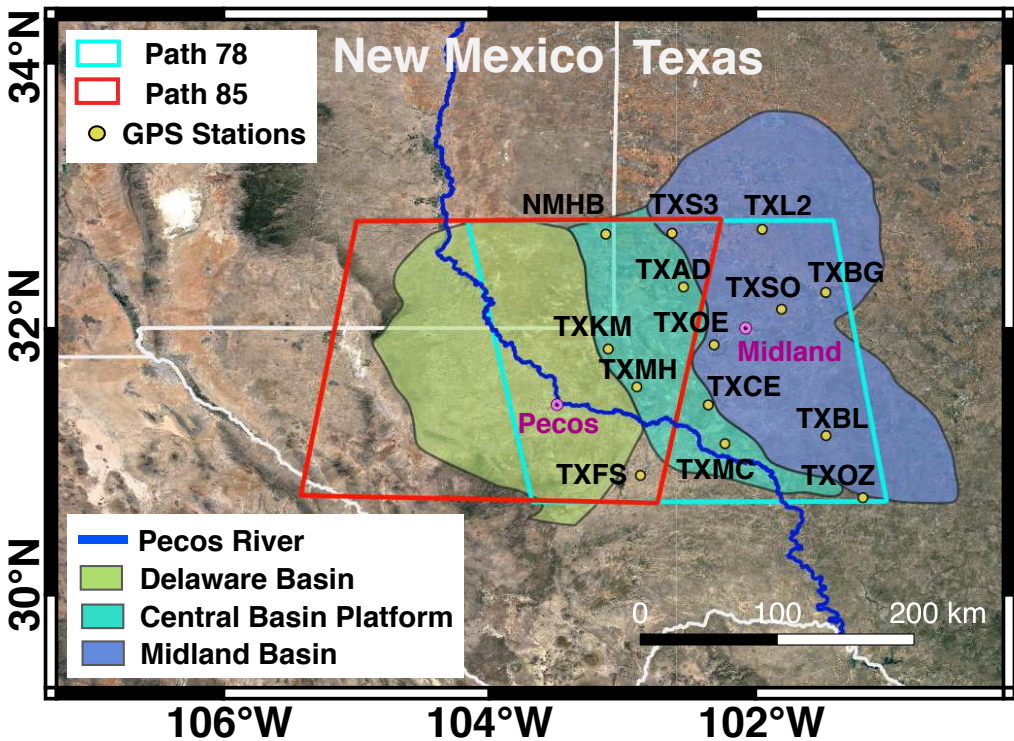
Figure 3.5: GPS and InSAR data coverage over the Permian Basin. Yellow dots indicate GPS permanent stations. Teal and red boxes indicate ascending path 78 and descending path 85 paths of Sentinel 1 InSAR coverage, respectively.
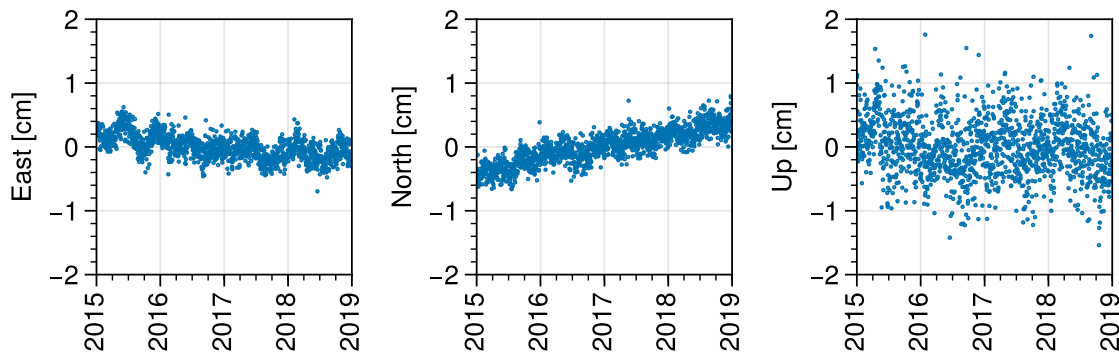
Figure 3.6: Example measurements of east, north, and vertical components of surface deformation from the permanent GPS station TXMC (Figure 3.5). All stations indicated in Figure 3.5 show similarly small deformation during the 2015-2019 period.

3.3 InSAR Processing Strategy and Noise Assessment

Using a geocoded SLC processor (Zheng and Zebker, 2017, Zebker, 2017) (Section 2.6), we processed 91 ascending (path 78, frames 94-104) and 82 descending (path 85, frames 483-493) Sentinel-1 scenes acquired between Nov. 2014 and Jan. 2019 (Figure 3.5). We generated more than 7000 interferograms with 120 meter pixel spacing and a maximum temporal baseline of 800 days. No spatial baseline threshold was imposed in the interferogram formation. Because few decorrelation artifacts were present, we were able to unwrap all interferograms without additional spatial filtering using the Statistical-cost, Network-flow Algorithm for Phase Unwrapping (SNAPHU) (Chen and Zebker, 2001). We removed long-wavelength phase ramps due tropospheric noise using a planar phase model. We chose the GPS station TXKM as the reference point for both ascending and descending InSAR data, and we used the remaining 13 stations as controls to assess InSAR measurement uncertainty (Chapter 4). Comparable interferograms can be generated using other processors such as the InSAR Scientific Computing Environment (ISCE) (Rosen et al., 2012) or GMTSAR (Sandwell et al., 2011).

Interferograms may contain noise from many possible sources (Section 2.4). In our West Texas data, $\Delta\phi_{orb}$ was negligible, and interferograms containing significant decorrelation, $\Delta\phi_{decor}$, or unwrapping artifacts, $\Delta\phi_{unwrap}$, were removed. Because the Permian Basin is located in the middle latitudes and is relatively flat, $\Delta\phi_{iono}$ and $\Delta\phi_{dem}$ are not substantial (Fattahi and Amelung, 2013, Liang et al., 2019). Tropospheric noise $\Delta\phi_{tropo}$ consists of a stratified component that correlates with topography (Doin et al., 2009) and a turbulent component that is random at time scales longer than one day (Emardson et al., 2003) (Section 2.4.2). Since the majority of the oil-producing Permian Basin is flat (less than 700 meters of elevation change), there is not a substantial stratified component of tropospheric noise in our data. The dominant noise source in the West Texas Sentinel-1 data is turbulent tropospheric noise.

We analyzed the effectiveness of tropospheric correction techniques based on auxiliary data using the Generic Atmospheric Correction Online Service (GACOS, (Yu et al., 2018a;b)), which derives its corrections using the High Resolution European Centre for Medium-Range Weather Forecasts (ECMWF) weather model (0.125-degree, 6-hour resolutions) and the GNSS-derived zenith delay maps from the Nevada
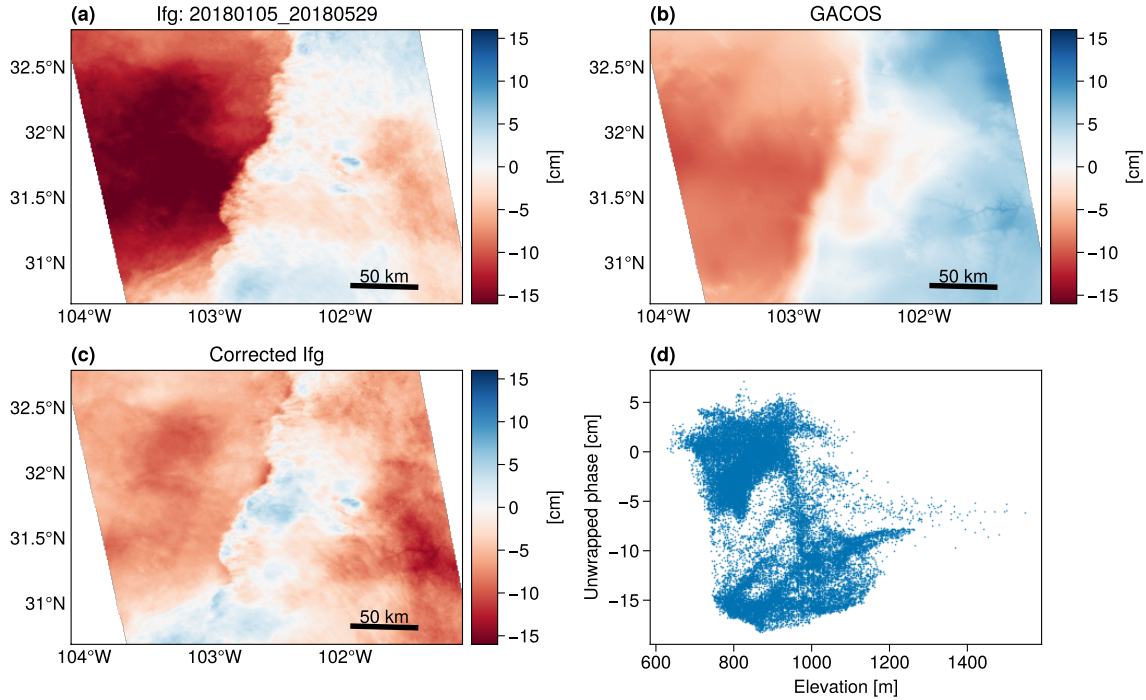
Figure 3.7: (a) Unwrapped interferogram from Jan. 5, 2018 to May 29, 2018. Blue indicates an increase in relative LOS delay. (b) Tropospheric correction predicted from delays computed by GACOS. (c) Corrected interferogram (panel (b) - panel (c)) (d) Unwrapped LOS measurements (in cm) of the 20180105-20180529 interferogram vs. the Digital Elevation Model (DEM) heights.

Geodetic Laboratory. Note that for the West Texas region, GACOS mostly relies on the weather model input due to the sparsity of GPS stations.

We illustrate several correction attempts for Sentinel-1 interferograms over West Texas using GACOS tropospheric corrections. In Figure 3.7, an ascending (Path 78) interferogram from Jan. 5, 2018 to May 29, 2018 contains a mass of dry air moving in from the New Mexico mountains, which creates a ~ 20 cm decrease in LOS delay in half of the interferogram (Figure 3.7a, red). Here the ECMWF weather model used by GACOS predicts the some of the delay change between the dates (Figure 3.7b). The root mean square (RMS) noise drops from 8.8 cm in the original interferogram to 5.7 cm after the GACOS correction (Figure 3.7c), despite the interferogram showing no discernible phase vs. elevation trend (Figure 3.7d).

In other examples, the GACOS corrections provided little benefit, and occasionally added noise to the interferogram. For example, Figure 3.8a shows a descending Path

37
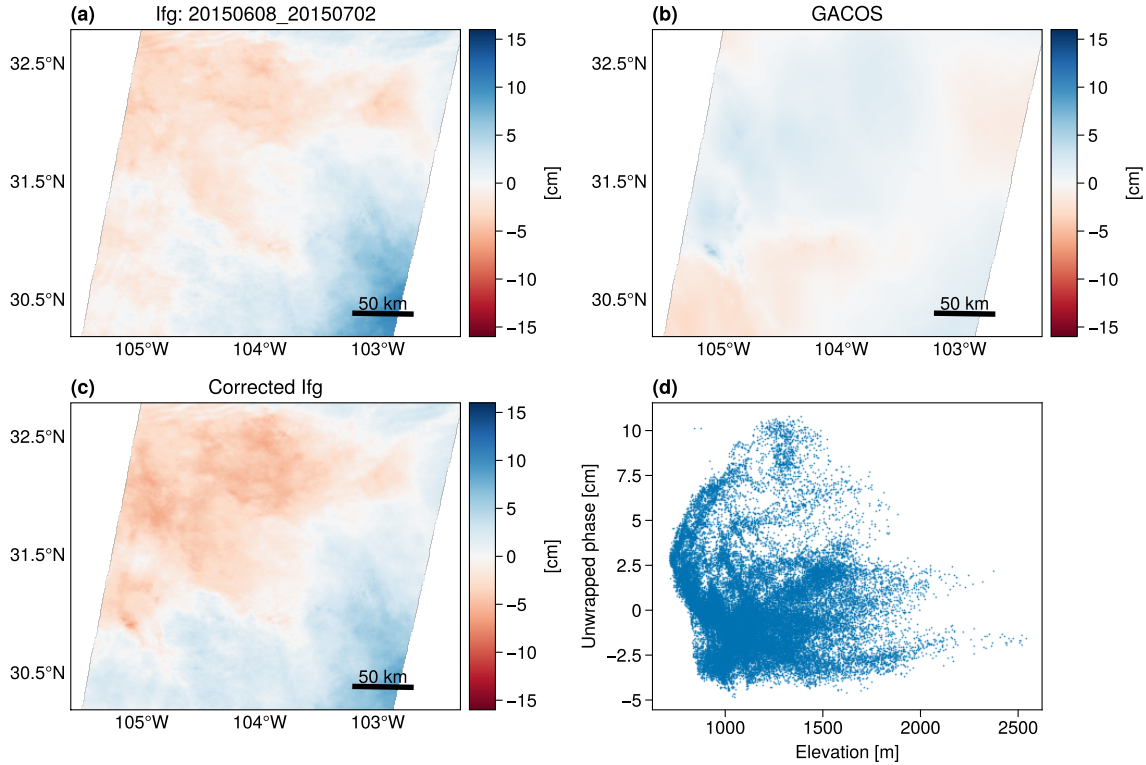
Figure 3.8: (a) Descending Path 85 unwrapped interferogram from June 8, 2015 to July. 2, 2015. Blue indicates an increase in relative LOS delay (b) Tropospheric correction predicted from delays computed by GACOS. (c) Corrected interferogram (panel (a) - panel (b)) (d) Unwrapped LOS measurements (in cm) of the 20150608-20150702 interferogram vs. the Digital Elevation Model (DEM) heights.

85 interferogram from June 8, 2015 to July 2, 2015. The GACOS correction is not correlated with the interferogram noise structure (Figure 3.8b), and the RMS noise in the corrected interferogram (Figure 3.8c) increased from 2.6 cm to 2.9 cm.

Thunderstorms commonly add 10-15 cm of turbulent tropospheric noise to interferograms with a summer SAR acquisition (Figure 3.9). During summer months, the weather conditions at the SAR acquisition time are visible in optical images taken by the Geostationary Operational Environmental Satellites (GOES) (Figure 3.9a). For example, tall cumulonimbus clouds covered much of West Texas on July 23, 2019 at the time of the Sentinel-1 acquisition (Figure 3.9a), which created patches of excess delay of > 10 cm in the interferogram from Jan. 12 to July 23, 2019 (Figure 3.9b). The different imaging geometries of the Sentinel-1 satellites (side-looking, in

38
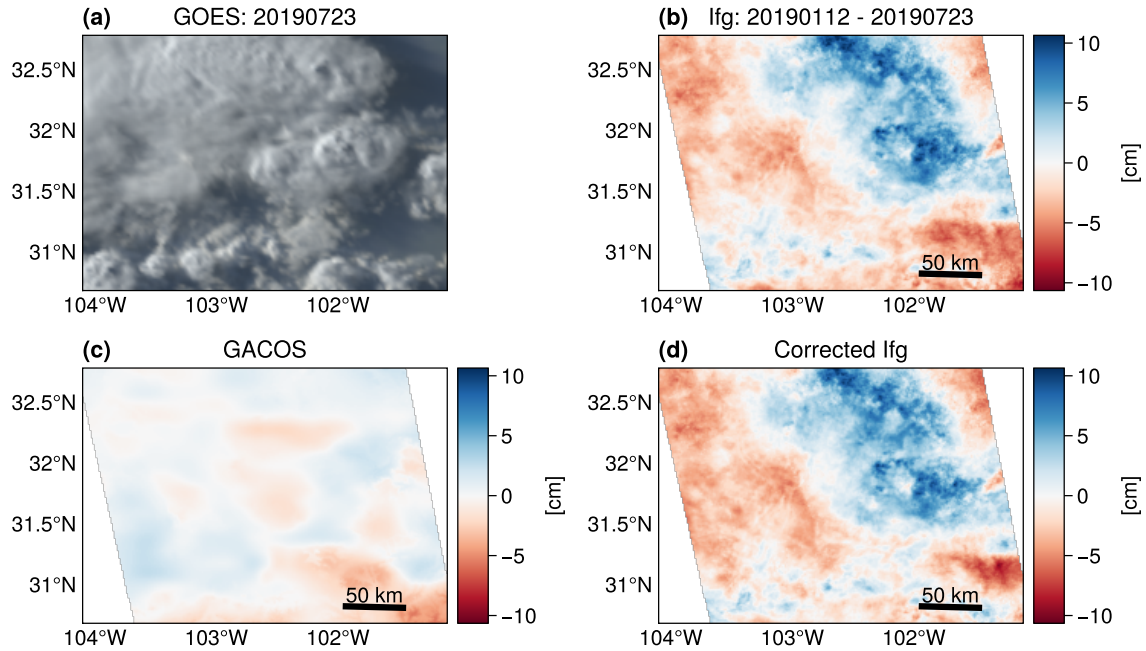
Figure 3.9: (a) Weather conditions visible from the GOES satellite on July 23rd, 2019 at the same time as the Sentinel-1 acquisition (b) Unwrapped interferogram from Jan. 12, 2019 to July 23, 2019. Blue indicates an increase in relative LOS delay (c) Tropospheric correction predicted from delays computed by GACOS. (d) Corrected interferogram (panel (b) - panel (c))

low Earth orbit) and the GOES satellites (nadir-looking, geostationary orbit) mean that the pixels of Figure 3.9a and Figure 3.9b do not fully align, but cover approximately the same area. The ~ 5 km storm cells are not predicted by GACOS due to the relatively coarse spatial and temporal resolution of global weather models (Figure 3.9c). Thus, the corrected interferogram still contains most of the turbulent noise from the storm (Figure 3.9d).

We also created line-of-sight delay estimates from weather models using the Ray-tracing Atmospheric Delay Estimation for Radar (RAiDER) library of Maurer et al. (2021). RAiDER generates a troposphere correction product by integrating the model-predicted delay along the radar LOS path for each InSAR pixel. We compared several weather model corrections to the ECMWF used by GACOS and found only small differences in the results. For example, the RMS noise of the interferogram in Figure 3.7 decreases an additional 0.8 cm by using NASA's Global Modeling and Assimilation Office (GMAO) reanalysis weather model, despite have 5x coarser

spatial resolution than the ECMWF. However, no model that we tested successfully generated corrections for Figure 3.9.

Since the turbulent tropospheric noise is difficult to predict and correct using the auxiliary correction methods, Chapters 4 and 5 present data-driven mitigation strategies for producing robust estimates of surface deformation.

Chapter 4

Cumulative Surface Deformation Solutions with Automated Outlier Removal

Previous InSAR studies have demonstrated the utility of surface deformation data for understanding causes of induced seismicity; however, these studies focused on study areas $\sim$ 60-by-60 km or smaller. Since InSAR tropospheric noise variance increases with the distance away from the reference point, it is difficult to expand the InSAR spatial coverage to the entire Permian Basin while retaining millimeter level accuracy. In this chapter, we present a time series method for creating large cumulative surface deformation maps over areas containing severe tropospheric noise. We developed an outlier detection algorithm that removes InSAR measurements corrupted by severe tropospheric noise (e.g. storms and heat waves). The method reduces the uncertainty in our linear deformation estimates by a factor of 2, down to 1-3 mm/year across the basin. Our results were validated by independent GPS measurements recorded at 13 permanent ground stations. We use the method to create yearly deformation maps from November 2014 through January 2019 over the oil-producing region of the Permian Basin, which are available through the Center for Integrated Seismicity Research (CISR) for the broader scientific community.

4.1 Algorithms

4.1.1 Stacking and InSAR Time Series Analysis

To investigate how InSAR measurement noise influences the line-of-sight (LOS) deformation solutions, we compared the results derived from (1) the stacking method, (2) an SBAS linear deformation (constant velocity) model with L_1 and L_2-norm penalty functions, and (3) unregularized and regularized SBAS deformation time series. We assume there are M small-baseline interferograms that were generated from N SAR scenes acquired over a period of interest. We employed a stacking approach (Sandwell and Price, 1998) to calculate the average LOS velocity v_{avg} of

each ground pixel over a time period of interest T as:

$$v_{avg} = \frac{\lambda}{4\pi} \frac{\sum_{i \in G} \boldsymbol{\Delta\phi}_i}{\sum_{i \in G} \boldsymbol{\Delta t}_i} \qquad (4.1)$$

where G is a subset of interferograms that were formed using two SAR scenes acquired within the time period T. The LOS measurement (in radians) and the temporal baseline of the ith interferogram in G are written as $\boldsymbol{\Delta\phi}_i$ and $\boldsymbol{\Delta t}_i$ respectively, and the factor $\frac{4\pi}{\lambda}$ converts radians to centimeters.

Similarly, the SBAS method outlined in Section 2.5 can be augmented with a linear deformation model. In this formulation, we solve for the average velocity v_{avg} over this period at each pixel of interest as (Berardino et al., 2002):

$$v_{avg} = \frac{\lambda}{4\pi} \cdot \arg\min_{v_{avg}} \|\boldsymbol{BP}v_{avg} - \boldsymbol{\Delta\phi}\|_p \qquad (4.2)$$

where $\boldsymbol{B}$ is the $M \times (N-1)$ SBAS matrix, $\boldsymbol{P}$ is an $(N-1) \times 1$ vector of ones, $\boldsymbol{\Delta\phi}$ is the $M \times 1$ vector of LOS measurements at this pixel, and $p \in \{1, 2\}$ is the norm used to penalize the data misfit. The L_2 linear deformation solution is comparable to the stacking solution (with an assumption of a constant velocity), and the L_1 solution is typically less sensitive to measurement outliers than the L_2 solution.

The full vector of LOS surface velocities between adjacent SAR acquisitions $\boldsymbol{v} = [v_1, \ldots, v_{N-1}]^T$ can be solved as:

$$\boldsymbol{v} = \frac{\lambda}{4\pi} \cdot \arg\min_{\boldsymbol{v}} \|\boldsymbol{Bv} - \boldsymbol{\Delta\phi}\|_2^2 + \alpha \|\boldsymbol{Dv}\|_2^2 \qquad (4.3)$$

where $\boldsymbol{D}$ is a $(N-2) \times (N-1)$ matrix, with 1 on the main diagonal and -1 on the superdiagonal, which approximates the first-order differentiation operator. The first term penalizes the data misfit, the second term is a temporal smoothness constraint, and $\alpha \in \mathbb{R}$ is the weight between the two terms. When $\alpha = 0$, the solution is the unregularized SBAS deformation time series. An additional integration of $\mathbf{v}$ over time yields the LOS deformation time series.

4.1.2 Tropospheric Noise Outlier Removal

We examined interferograms at the 13 control locations and discovered that non-Gaussian tails (outliers) are present. For example, LOS measurements of the ascending interferograms at pixels near the GPS station TXMC show a near zero median (-4 mm) and a standard deviation of 3.2 cm (Figure 4.1 (a)). Due to the absence of substantial deformation signal at this station, the standard deviation of the LOS distribution is a measure of turbulent tropospheric noise. We found that the median LOS turbulent error is close to zero (no systematic noise bias) at all GPS control stations. The standard deviation of the turbulent noise increases as the square root of the distance from the InSAR reference point (Figure 4.1 (b)). Furthermore, we compared the LOS turbulent noise distribution observed at each GPS station to a normal distribution using a normal probability plot (Filliben, 1975) (e.g. Figure 4.1(c)). The probability plot illustrates the deviation of a set of samples from a normal distribution, which in our case occurs at the tails due to occasional severe tropospheric noise events (e.g. storms or heat waves).

Because severe tropospheric noise may only impact a portion of a SAR image, we identified InSAR measurement outliers at each pixel independently as follows. Given N SAR acquisitions, there are up to $N - 1$ InSAR LOS measurements at a pixel of interest that contain the common tropospheric noise of the kth SAR scene. We defined $u_{k,n}$ as the nth such LOS measurement, and $\bar{u}_k$ as the mean absolute measurement:

$$\bar{u}_k = \frac{1}{N-1} \sum_{n=1}^{N-1} |u_{k,n}| \tag{4.4}$$

We labeled $u_{k,n}$ (for all n) as outlier measurements if $\bar{u}_k > \text{median}(\bar{\mathbf{u}}) + 4\sigma_{\text{MAD}}$, where $\bar{\mathbf{u}} = [\bar{u}_1, ..., \bar{u}_N]$, and $\sigma_{\text{MAD}} = 1.483 \cdot \text{MAD}(\bar{\mathbf{u}})$. Here we employed a robust statistics measure, the median absolute deviation (MAD), for estimating the spread of data samples in the presence of outliers (Hampel, 1974, Rousseeuw and Hubert, 2011). Given a vector $\mathbf{x}$ that contains M data samples, $\text{MAD}(\mathbf{x})$ is defined as:

$$\text{MAD}(\mathbf{x}) = \underset{m=1,...M}{\text{median}} \left(\left| x_m - \text{median}(\mathbf{x}) \right| \right) \tag{4.5}$$

where x_m is the mth data sample.
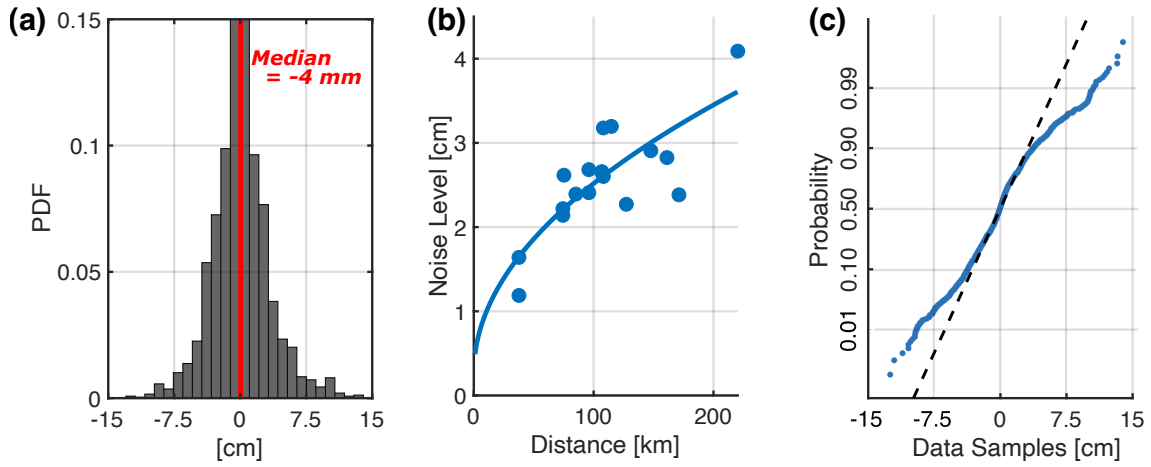
Figure 4.1: (a) LOS measurements (in cm) of all ascending interferograms at the GPS station TXMC. The distribution has a near zero median (-4 mm) and a standard deviation of 3.2 cm. Due to the absence of substantial deformation signals, the standard deviation of the distribution is a measure of LOS turbulent tropospheric noise. (b) The standard deviation of random tropospheric turbulent noise at 13 control locations (blue dots), which increases as the square root of the distance from the InSAR reference point (blue line). (c) A comparison between the tropospheric noise distribution at TXMC with a normal distribution. Dashed line connects the 1st and 3rd quartiles of the data. Troposphere noise following a normal distribution would match the dashed line, but the noise distribution has larger tails.

4.1.3   Line-of-sight Decomposition

An interferogram measures surface deformation between the two SAR acquisition times along the radar LOS direction. The LOS deformation, u_{LOS}, can be written as:

$$u_{LOS} = \alpha_e u_e + \alpha_n u_n + \alpha_u u_u \tag{4.6}$$

where u_e, u_n and u_u are the east, north and up displacements, respectively. The radar look vector $\alpha = [\alpha_e, \alpha_n, \alpha_u]$ can be calculated from the known imaging geometry at every pixel location. This varies significantly for Sentinel-1 due to the $\sim$250 km wide swath (Figure 4.2).

In regions where InSAR data are available from two LOS directions, we can decompose the ground motion into its eastward and vertical components. To perform the decomposition, we first write u_{asc} and u_{desc} in terms of u_e, u_n and u_u:

$$u_{asc} = \alpha_{a,e} u_e + \alpha_{a,n} u_n + \alpha_{a,u} u_u \tag{4.7}$$

$$u_{desc} = \alpha_{d,e} u_e + \alpha_{d,n} u_n + \alpha_{d,u} u_u \tag{4.8}$$

We can express u_e and u_u as:

$$u_e \approx \frac{1}{\beta} \left[\alpha_{d,u} u_{asc} - \alpha_{a,u} u_{desc} \right] \tag{4.9}$$

$$u_u \approx \frac{1}{\beta} \left[\alpha_{a,e} u_{desc} - \alpha_{d,e} u_{asc} \right] \tag{4.10}$$

where $\beta = \alpha_{a,e} \alpha_{d,u} - \alpha_{d,e} \alpha_{a,u}$. Because Sentinel-1 satellites are operating in a near-polar orbit, the north look coefficients $\alpha_{a,n}$ and $\alpha_{d,n}$ are both relatively small. Ignoring 1 cm northward motion in u_n only leads to $\sim$ 0.1-0.2 mm error in u_e and $\sim$ 1 mm error in u_u at most locations.

4.2   Time Series Comparisons and Outlier Removal

Here we used the Sentinel-1 interferograms from Path 78 and Path 85 processed in Section 3.3. We solved for the cumulative LOS deformation using each time series method from Section 4.1.1 over three periods of interest: Nov. 2014 to Jan. 2017, Nov. 2014 to Jan. 2018, and Nov. 2014 to Jan. 2019. For the time series methods
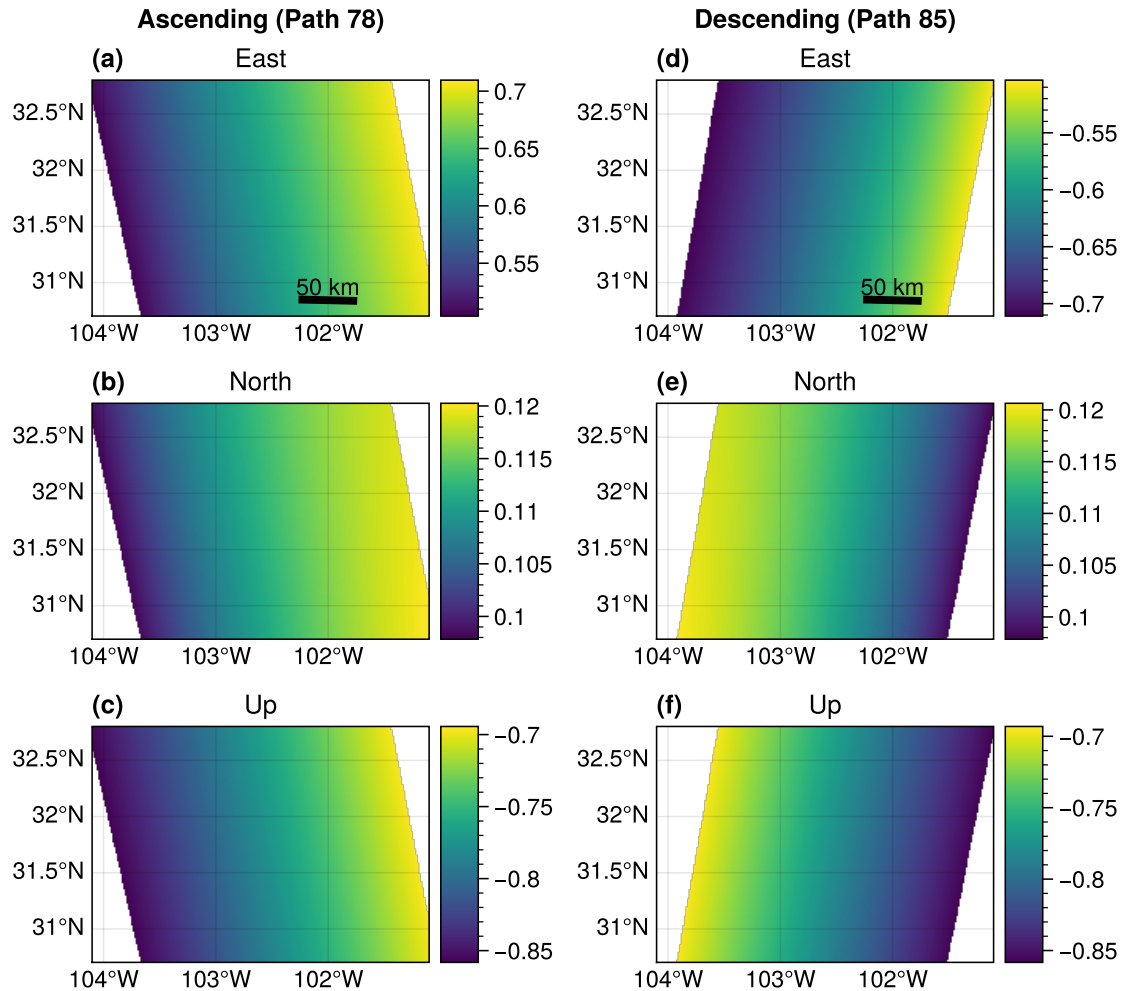
Figure 4.2: East, north, and vertical coefficient of the LOS unit vector of all Sentinel-1 Path 78 and Path 85 pixels. Positive LOS direction points away from the satellite to the ground.
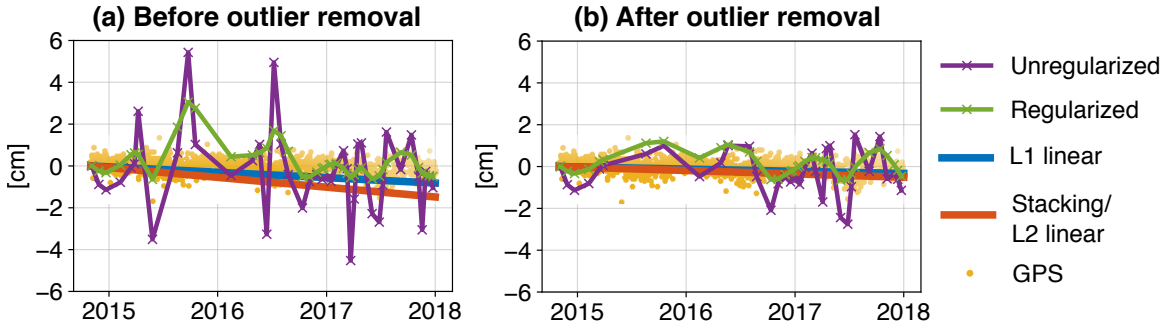
Figure 4.3: Comparisons of InSAR unregularized SBAS time series (purple), regularized SBAS time series (green), linear deformation trend estimated by minimizing the L_1-norm of the residuals (blue), and the L_2-norm of the residuals/ stacking approach (red) (a) before and (b) after removing LOS measurement outliers. ENU GPS data from station TXSO has been projected onto the radar LOS (orange dots).

that calculate an average velocity $v_{avg,j}$ over the jth time period T_j , we computed the cumulative LOS surface deformation as the product $v_{avg,j} \cdot T_j$.

To compare the time series methods, we projected the 13 GPS ENU time series onto the radar LOS. We computed the average GPS LOS velocity using a linear regression and took this as ground truth. We found that InSAR tropospheric noise has a strong influence on all the surface deformation solutions before removing the measurement outliers. As an example, Figure 4.3 (a) shows the ascending Path 78 LOS solutions between Nov. 2014 and Jan. 2018 at the GPS station TXSO before removing InSAR measurement outliers. The random tropospheric noise creates up to ∼6 cm of error in the unregularized SBAS surface deformation time series. This error can be reduced by increasing α in Equation (4.3). As α increases, the LOS deformation time series converge to the L_2 linear deformation (constant velocity) solution.

After removing InSAR outlier measurements associated with local weather events, all SBAS time series methods produce more accurate and consistent deformation trends (Figure 4.3 (b)). The unregularized SBAS time series still contains up to ∼3 cm of tropospheric noise, leading to long-wavelength artifacts in the basin-wide deformation maps. The L_1 and L_2 linear deformation solutions show close agreement (< 2 mm difference) at all GPS stations. Table 4.1 summarizes the differences before and after removing outliers for the four methods using the root mean square (RMS) and the worst-case absolute differences between InSAR and the 13 GPS average velocities.

Table 4.1: Errors (in mm) in four SBAS ascending LOS deformation (Nov. 2014 - Jan. 2018) solutions

	Before the outlier removal (RMS / Worst)	After the outlier removal (RMS / Worst)
Unregularized	22 / 99	14 / 43
Regularized	14 / 63	10 / 27
L1 linear deformation	7 / 11	4 / 8
L2 linear deformation	10 / 22	4 / 8
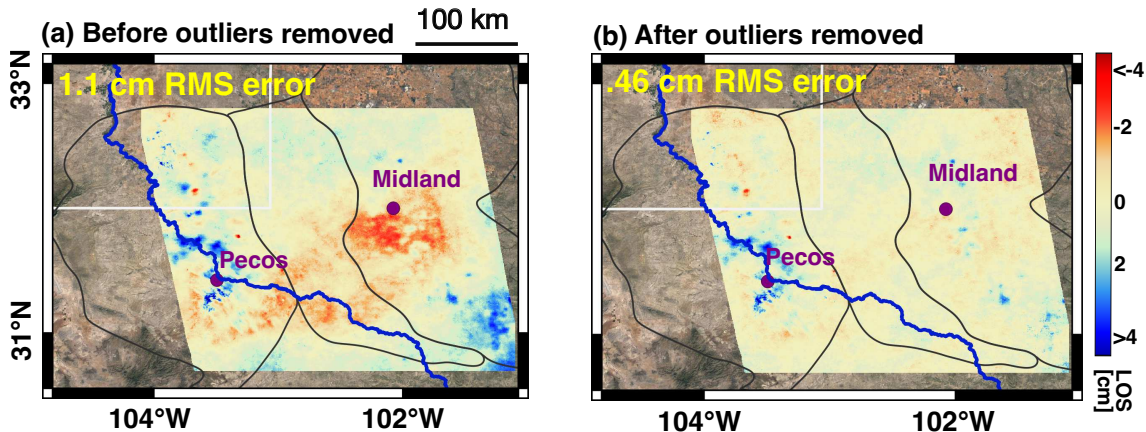
Figure 4.4: Cumulative ascending LOS deformation solutions (Nov. 2014 - Jan. 2018) (a) before and (b) after excluding InSAR outlier measurements. Note that 1.1 cm cumulative error over 3 years is equivalent to 3.5 mm/year RMS error in the velocity estimate.

Since both linear methods suggest a deformation trend consistent with the stacking approach, we chose the simple stacking method as the final processing strategy.

We see a striking visual difference in the Path 78 cumulative deformation map from Nov. 2014 to Jan. 2018 after removing tropospheric outliers (Figure 4.4). There are cm-level tropospheric artifacts in the deformation solution that uses all noisy measurements (Figure 4.4(a)). These long wavelength artifacts (e.g. the red streak near Midland) do not match the GPS stations measurements. However, the artifacts were mitigated using the pixel-wise outlier removal algorithm (Figure 4.4 (b)).

Table 4.2 shows the RMS and the worst-case absolute differences between the ascending Path 78 InSAR and GPS inferred average LOS velocities for all three study periods. For each time period, our outlier removal algorithm reduced the uncertainty

Table 4.2: InSAR ascending Path 78 LOS velocity estimation errors (in mm/year) using the stacking method

	Before the outlier removal (RMS / Worst)	After the outlier removal (RMS / Worst)
Nov. 2014 - Jan. 2017	3.8 / 9.5	1.9 / 5.9
Nov. 2014 - Jan. 2018	3.3 / 7.1	1.3 / 2.5
Nov. 2014 - Jan. 2019	2.0 / 6.1	1.1 / 2.5

Table 4.3: InSAR descending Path 85 LOS velocity estimation errors (in mm/year) using the stacking method

	Before the outlier removal (RMS / Worst)	After the outlier removal (RMS / Worst)
Nov. 2014 - Jan. 2017	7.8 / 13.8	2.9 / 5.0
Nov. 2014 - Jan. 2018	3.7 / 7.5	2.7 / 5.6
Nov. 2014 - Jan. 2019	1.6 / 2.8	0.8 / 1.6

in the InSAR stacking solution by a factor of ~2, down to 1-3 mm/year RMS across the basin. Similarly, Table 4.3 shows the uncertainty in the Path 85 descending stacking solutions using the 5 permanent GPS stations available in the SAR footprint. We also see reduction in noise by a factor of ~2 for Path 85. Note that for a given period of interest T_j, the LOS velocity error $E_{vel,j}$ propagates into the cumulative deformation error $E_{c,j}$ as $E_{c,j} = E_{vel,j} \cdot T_j$.

4.3 Surface Deformation in the Permian Basin

The Sentinel-1 cumulative LOS deformation solutions reveal numerous surface deformation features over the oil-producing region in the Permian Basin (Figure 4.5). From the ascending geometry, we observed no substantial deformation in the Central Basin Platform, where oil and gas are mostly produced from conventional reservoirs. In the Midland and Delaware Basins, we observed an accelerating surface deformation rate between Nov. 2014 and Jan. 2019, which coincides with the sharp rise of oil production from unconventional reservoirs in 2017 and 2018. For example, a 30 km^2 area northwest of Pecos shows approximately 0.5 cm cumulative LOS deformation between Nov. 2014 and Jan. 2017, 1.5 cm between Nov. 2014 and Jan. 2018, and over 5.5 cm from Nov. 2014 to Jan. 2019. The greatest number of observable signals
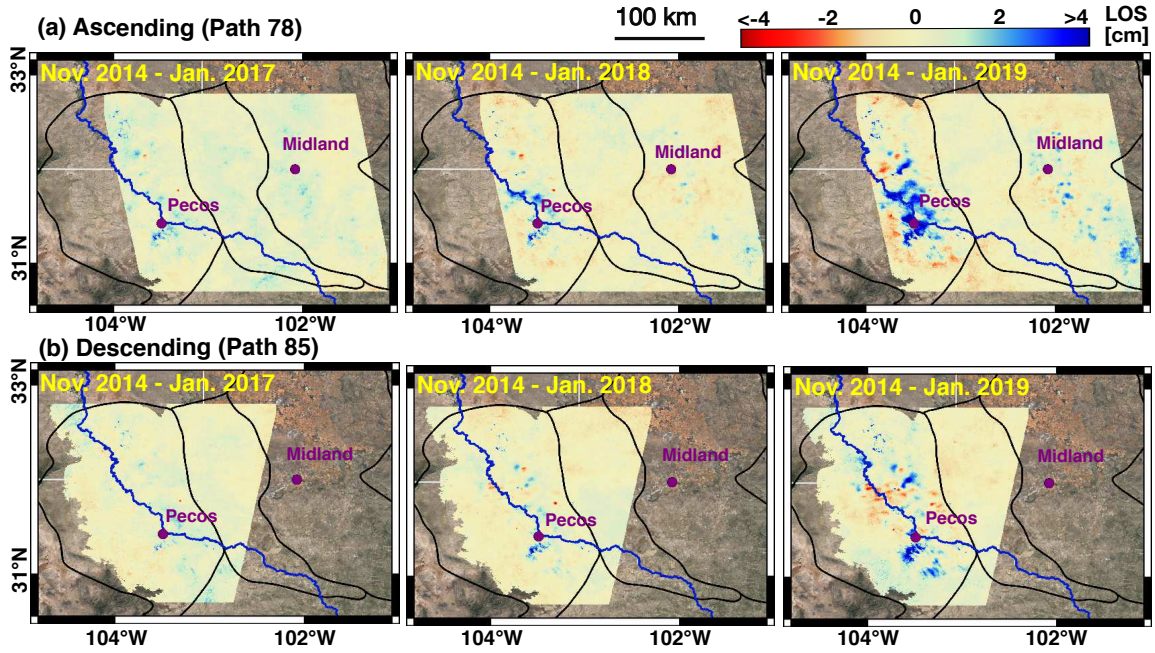
Figure 4.5: Cumulative LOS deformation (Nov. 2014 - Jan.2017; Nov. 2014 - Jan.2018; Nov. 2014 - Jan. 2019) as inferred from Sentinel-1 (a) ascending Path 78, and (b) descending Path 85 data over an 80,000 square km oil-producing region of the Permian Basin. Here a subsidence or eastward deformation signal leads to a positive LOS measurement in the ascending geometry, and a subsidence or westward deformation signal leads to a positive LOS measurement in the descending geometry. Areas with >1200 m altitude are masked due to the low oil production activity in mountainous regions.

are present in 2018 when peak production occurred in the region. Similarly, from the descending geometry, we find no substantial deformation in the Central Basin Platform and an increasing rate of surface deformation in the Delaware Basin.

We also solved for the vertical and eastward deformation in the region where Path 78 and 85 overlap (see Section 4.1.3) using the LOS unit vector at each pixel location (Figure 4.2). To illustrate the decomposition, Figure 4.6 shows a 12 km x 12 km region centered on a wastewater injection well found by Kim and Lu (2018) to have injection-related uplift. We observe similar magnitude deformation toward the satellite in both ascending and descending tracks (Figure 4.6 top). After decomposing the two geometries, we calculated ∼ 5.5 cm of uplift and ∼1.2 cm of east-west motion between November 2014 and April 2017 (Figure 4.6 bottom), similar to the magnitudes found in Kim and Lu (2018).
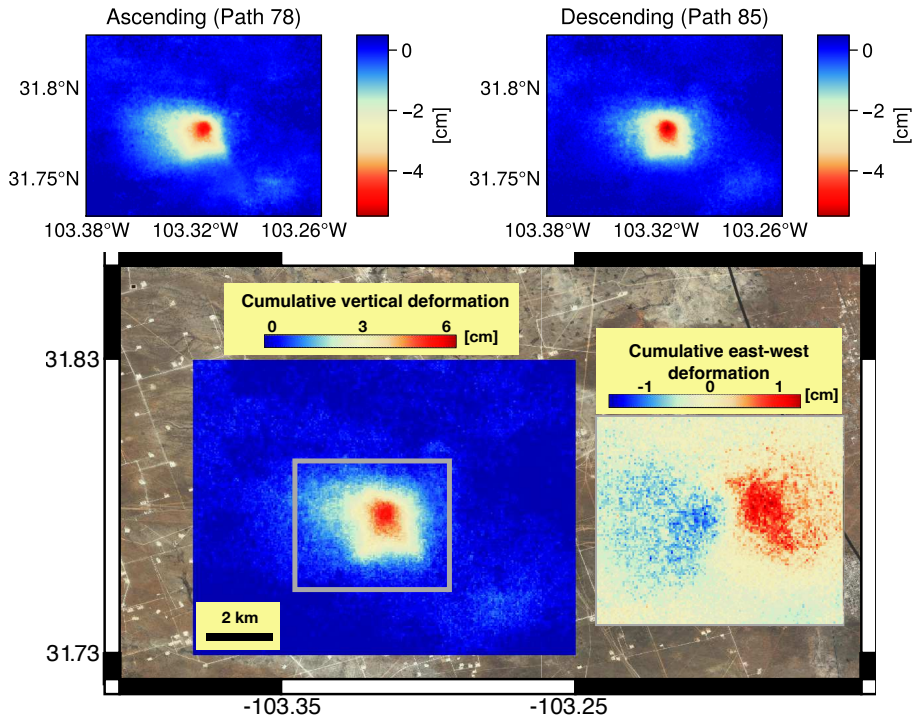
Figure 4.6: (top) Ascending and descending line-of-sight cumulative deformation between November 2014 and April 2017. Red indicates motion toward each satellite. (bottom) Cumulative vertical and horizontal surface deformation due to wastewater injection in Winkler County, TX. The horizontal motion here is $\sim 20\%$ of the vertical motion, with up to ~ 5.5 cm of uplift and ~ 1.2 cm of east-west motion. This localized deformation feature was originally reported in Kim and Lu (2018).

In the northern Delaware Basin, where large volumes of oil production and wastewater disposal occurred, the ascending and descending LOS deformation patterns are similar. This means that the observed deformation in this region is primarily vertical (Figure 4.7 (b) and (e)). The observed subsidence or uplift features between Nov. 2014 and Jan. 2019 are $\sim$ 1-4 cm. In the southern Delaware Basin, Deng et al. (2020) solved for the cumulative LOS surface deformation between Nov. 2014 and Feb. 2019 ($\sim$ 100 km by 60 km) using the ascending Sentinel-1 data (Path 78 frames 99-100). In this study, we found that the observed magnitudes of the ascending and descending LOS deformation are different (Figure 4.5), which suggests that both horizontal and vertical deformation occurred in this region. Previous studies near Mesquite, Nevada have shown that confined aquifer pumping in the presence of faults can produce complex asymmetrical deformation patterns with a non-trivial horizontal component (Burbey, 2008). In the Pecos area, the largest subsidence patterns ($\sim$ 13 cm over 4 years) occurred $\sim$ 15 km south of Pecos, and the largest eastward motion ($\sim$ 3-4 cm over 4 years) occurred near the town of Pecos along a line transect (Figure 4.7 (c) and (f)). The observed linear deformation patterns align with the inferred favorable fault plane orientation proposed by Lund Snee and Zoback (2018) (a strike angle of $\sim$ 300 degrees, lining up with the measured S_{Hmax} direction), and they also align with a cluster of recent shallow earthquakes ($<$ 3 km depth) cataloged by TexNet.
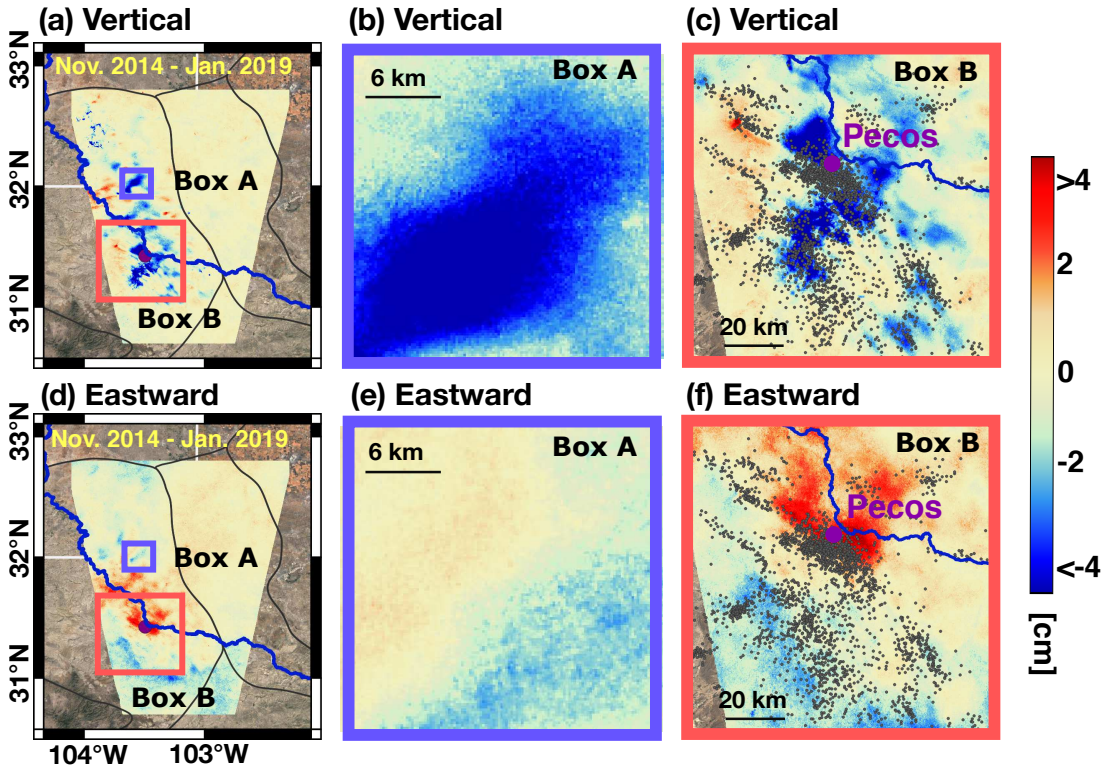
Figure 4.7: (a) Cumulative vertical deformation between Nov. 2014 and Jan. 2019 over the region where Sentinel-1 Path 78 and Path 85 overlap. A zoomed-in view of Box A in the northern Delaware Basin and Box B in the southern Delaware Basin are shown in panel (b) and (c) respectively. (d) Cumulative eastward deformation between Nov. 2014 and Jan. 2019 over the region where Sentinel-1 Path 78 and Path 85 overlap. A zoomed-in view of Box A in the northern Delaware Basin and Box B in the southern Delaware Basin are shown in panel (e) and (f) respectively. In the southern Delaware Basin, the observed vertical and eastward deformation (panel (c) and (f)) show linear patterns along with earthquake hypocenters (gray dots) detected by TexNet in 2018.

4.4 Implications for Geomechanical Modeling

Based on fault plane solutions derived from recent seismic activity and the faulting stress regime interpretations (Lund Snee and Zoback, 2018), the Pecos area is in a normal faulting regime. We employed an elastic dislocation model (Okada, 1992) to demonstrate that the presence of dip-slip normal faults can produce the observed linear subsidence patterns in this area (Figure 4.8 (a)). We solved for the dip angle, depth, width along the dip direction, and slip magnitude of four normal faults by best fitting the forward model to InSAR vertical deformation observations, minimizing the sum of squared residuals, and maximizing the R-squared values (Du et al., 1992) (Appendix A.1). The optimal solution suggests that the depth of the faults ranges from 0.9 km to 1.5 km, which is shallower than most of the TexNet recorded earthquakes (2-6 km in depth). Possible explanations for this discrepancy include: (1) the existence of aseismic fault slippage being responsible for the observed surface deformation (McGarr and Barbour, 2017); (2) bias in earthquake depth estimation in the TexNet catalog (Lomax and Savvaidis, 2019); (3) systematic modeling errors associated with representing a mechanically layered earth as a homogeneous half space (Du et al., 1992).

After removing the best-fit deformation associated with dip-slip faulting (Figure 4.8 (b)), there is still $\sim$ 2 cm residual subsidence in the Pecos area (e.g. Figure 4.8 (f)). Given that shallow groundwater production was minimal in this region for the time period of interest (Deng et al., 2020), we introduced an elastic reservoir compaction model (Geertsma et al., 1973) to our geomechanical analysis (Appendix A.2). We implemented two layers of multiple cylindrical reservoirs corresponding to reported locations and depths of well clusters in the Delaware Mountain Group (DMG) and Wolfcamp reservoirs, which account for most of the recent oil and gas production in the region. We discretized the DMG layer based on a cluster of production wells predominantly perforated over a depth range of 1.5-1.8 km. The Wolfcamp wells are completed over a depth range of 3-3.6 km. We employed an objective function inversion method to solve for the reservoir pressure depletion pattern that best fit the InSAR-observed subsidence (Figure 4.8 (c)) (Du and Olson, 2001).

An important conclusion of this study is that both fault slip and reservoir inflation or compaction can produce observable surface deformation over an 80,000 square kilometer oil-producing region of the Permian Basin. The InSAR-observed subsi-
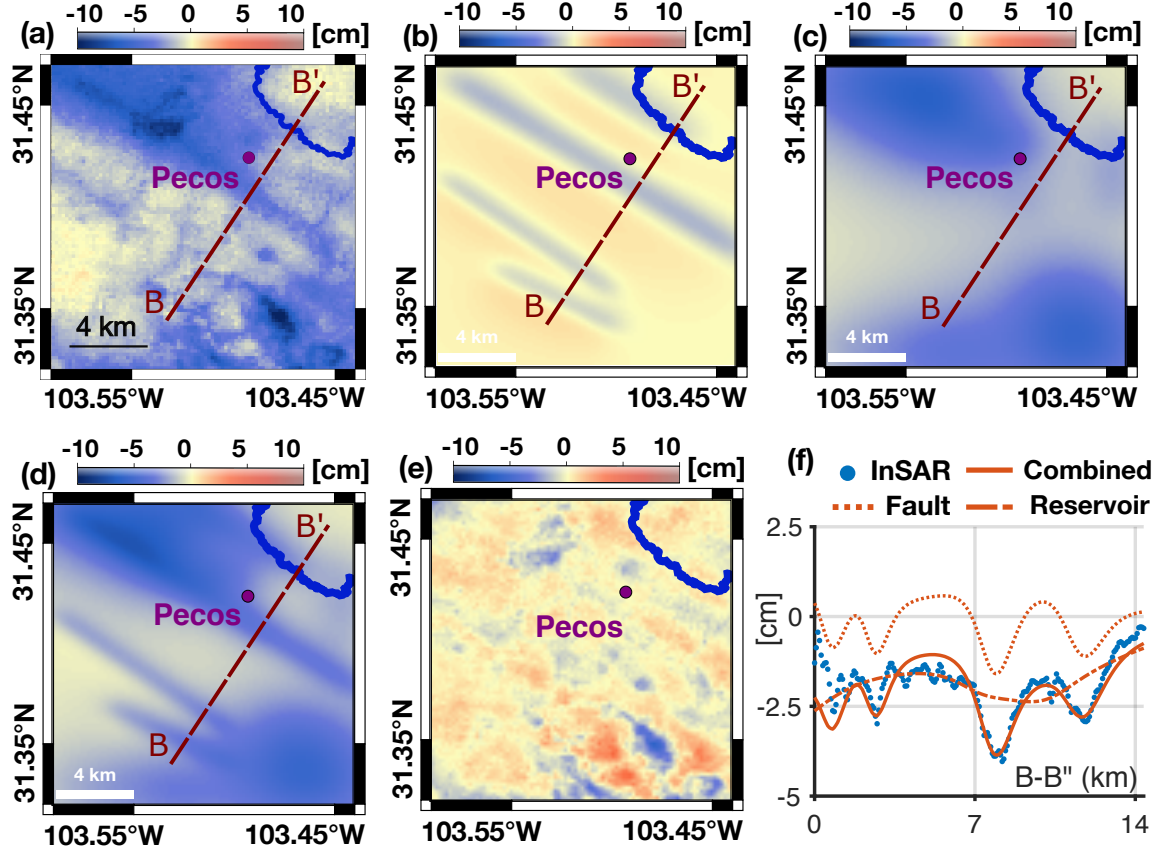
Figure 4.8: (a) InSAR-observed cumulative vertical deformation between Nov. 2014 and Jan. 2019 in the Pecos, TX area. (b) Modeled vertical deformation associated with four dip-slip faults. (c) Modeled vertical deformation associated with reservoir compaction. (d) Modeled total vertical deformation associated with four dip-slip faults and reservoir compaction (panel (b) + panel (c)). (e) Difference between InSAR-observed and model-predicted vertical deformation (panel (a) − panel (d)). (f) Difference between InSAR-observed and model-predicted vertical deformation along the B-B' transect.

dence patterns over the Pecos area can be modeled as slip over multiple faults and discretized cylindrical reservoir compaction (Figure 4.8 (d)-(f)). We note that InSAR subsidence data alone can constrain all pertinent fault and reservoir parameters in our normal faulting and reservoir compaction models. The InSAR observed cumulative surface deformation patterns, which show larger horizontal component than the model prediction, suggest that other factors, such as strike-slip faulting and heterogeneity in subsurface properties, may play a role. There have been extensive studies on how reservoir compaction and inflation as well as fault slippage alter stress fields in the subsurface and produce surface deformation (Geertsma et al., 1973, Segall, 1992, Okada, 1992, Du et al., 1992, Vasco and Ferretti, 2005, Vasco et al., 2008, Khakim et al., 2012). InSAR surface deformation can be combined with this knowledge to evaluate fluid recovery efficiency and monitor disposal wells at low cost. Furthermore, these high-quality geodetic measurements are readily available to complement the TexNet seismic catalog for assessing the likelihood of fault motion and induced earthquake risks in Texas.

Robust Time Series Methods for Estimating Non-Linear Deformation

In this chapter, we present a method for robustly extracting slowly-varying surface deformation. We perform a temporal smoothing using the robust Locally Weighted Scatterplot Smoothing (LOWESS) technique (Cleveland, 1979) on noisy surface deformation time series derived using SBAS. The LOWESS smoothing technique easily accounts for nonlinear deformation while also suppressing the strong summer tropospheric noise. We demonstrate the technique on both synthetic data and on three paths of Sentinel-1 data over the Permian Basin. The cumulative results show subtle basin-wide uplift features arising after 4-5 years of heavy sustained wastewater injection.

5.1 Algorithm

Consider a time series of N LOS phase delays for a single pixel, $\boldsymbol{\phi} = [\phi_0, \phi_1, \ldots, \phi_{N-1}]^T$ sampled at time intervals $\boldsymbol{t} = [t_0, \ldots, t_{N-1}]^T$, solved from the SBAS linear system (Equation (2.12)). We can write each element ϕ_i as a sum of surface deformation and atmospheric delay,

$$\phi_i = \frac{4\pi}{\lambda} (d_i + \alpha_i) \tag{5.1}$$

where d_i and α_i are the surface deformation and atmospheric delay on the ith day, and λ is the radar wavelength. Here we consider the case that the interferogram-specific noise sources (e.g. $\Delta\phi_{decor}, \Delta\phi_{unwrap}, \Delta\phi_{scat}$) have been properly accounted for in the inversion process so that the remaining noise in $\boldsymbol{\phi}$ is predominantly from the atmospheric delay $\boldsymbol{\alpha} = [\alpha_0, \ldots, \alpha_{N-1}]^T$. Our goal is to separate the vector of surface deformation $\boldsymbol{d} = [d_0, d_1, \ldots, d_{N-1}]^T$ from the atmospheric noise $\boldsymbol{\alpha}$.

The most widely used non-parametric methods for separating $\boldsymbol{d}$ from $\boldsymbol{\alpha}$ rely on the fact that the turbulent component of $\boldsymbol{\alpha}$ is uncorrelated in time, while most deformation sources show strong temporal correlation. For example, the authors of Ferretti et al. (2000) and Berardino et al. (2002) estimated $\boldsymbol{\alpha}$ by performing a high-pass temporal filter on each pixel followed by spatially low pass filtering the residual
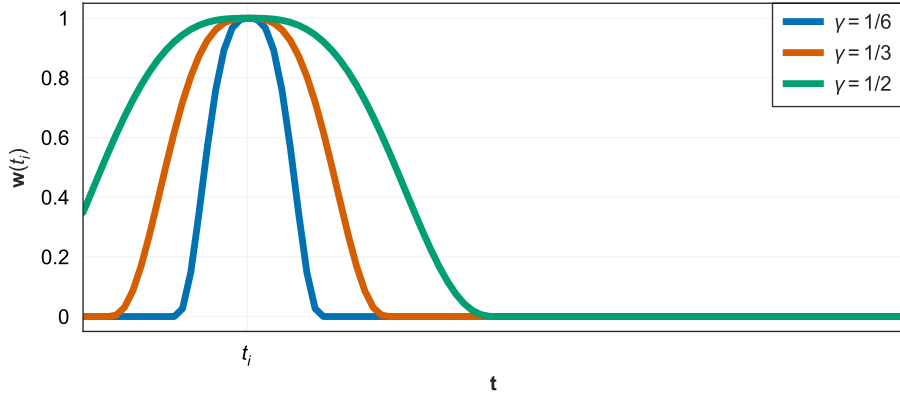
Figure 5.1: LOWESS tricube weighting function $\boldsymbol{w}(t_i)$ for an inclusion fraction of $\gamma = 1/6$ (blue), $\gamma = 1/3$ (orange), and $\gamma = 1/2$ (green).

phase. The temporal high pass filter was implemented by subtracting a low-pass filtered version of $\boldsymbol{\phi}$ (using a triangular filter in Ferretti et al. (2000)) from the original unfiltered version. One difficulty with the triangular filter and linear methods enforcing temporal smoothness is that the filter coefficients are non-adaptive; noisier atmospheric conditions will be weighted the same as calmer conditions (Liu, 2012). This can cause considerable leakage of noise from severe weather conditions into the deformation estimate of adjacent days (e.g. the regularized solution shown in Figure 4.3a).

We can adaptively filter the noisy $\boldsymbol{\phi}$ time series by implementing a robust LOWESS regression (Cleveland, 1979). The LOWESS algorithm fits a local linear regression at every t_i using nearby data points, repeating over multiple iterations to refine the fit and reduce the effect of outliers (Efron and Hastie, 2019). For the first iteration, at each time t_i, we calculate a set of weights $\boldsymbol{w}(t_i)$. The weight function has a maximum value of 1 at t_i and decays to zero at the rth nearest neighbor to t_i, where $r = \lfloor \gamma N \rfloor$, $0 < \gamma \leq 1$ is the fraction of the data chosen to include for each local fit, and $\lfloor x \rfloor$ is rounds x down to the next lowest integer. Let h_i be the rth smallest number of $|t_i - t_k|$ for $k = 0, \ldots, N - 1$. The kth weight $w_k(t_i)$ is defined as

$$
w_k(t_i) = \begin{cases} \left(1 - \left|\frac{t_i - t_k}{h_i}\right|^3\right)^3, & \text{if } \left|\frac{t_i - t_k}{h_i}\right| < 1 \\ 0, & \text{otherwise} \end{cases}
\tag{5.2}
$$

for $k = 0, \ldots, N - 1$. This weight function is known as the *tricube* weighting function. Figure 5.1 illustrates the shape of $\boldsymbol{w}(t_i)$ for $\gamma = 1/6, 1/3$ and $1/2$.

Using $\boldsymbol{w}(t_i)$, we compute a weighted linear regression around t_i by finding the intercept, a_i, and slope, b_i, that minimize

$$\sum_{k=0}^{N-1} w_k(t_i) \left(\phi_k - a_i - b_i t_k\right)^2 . \tag{5.3}$$

The smoothed estimate $\hat{\phi}_i$ at the point t_i is calculated as $\hat{\phi}_i = a_i + t_i b_i$. This process is repeated for all t_i, $i = 0, \ldots, N - 1$.

The second iteration performs another weighted least squares fit, this time further downweighting based on the residuals of the first iteration. Let $\epsilon_k = \left|\hat{\phi}_k - \phi_k\right|$ be the residual at t_k and s be the median residual for all k. We create an additional set of weights δ_k for each $k = 0, \ldots, N - 1$ as

$$\delta_k = \begin{cases} \left(1 - \left(\frac{\hat{\phi}_k - \phi_k}{6s}\right)^2\right)^2, & \text{if } \left(\frac{\hat{\phi}_k - \phi_k}{6s}\right) < 1 \\ 0, & \text{otherwise} \end{cases} \tag{5.4}$$

Equation (5.4) uses a median so that large outliers are clipped to 0, similar to the use of the median absolute deviation from Section 4.1.2. For each new fit in the second iteration, the weights $\boldsymbol{w}(t_i)$ are multiplied point-wise by the residual weights $\boldsymbol{\delta}$ to perform the local regressions.

Finally, we perform a shift of the smoothed $\hat{\boldsymbol{\phi}}$ to compensate for the first day's atmospheric conditions by setting $\hat{\phi}_i = \hat{\phi}_i - \hat{\phi}_0$ for all $i = 1, \ldots, N - 1$. This step is necessary for $\boldsymbol{\phi}$ solved using the SBAS formulation of Equation (2.12), since α_0 is added to all other dates when the first date's phase is assumed to be 0. While Ferretti et al. (2000) use mean value of the common-reference interferogram phases as an estimation of the first date's atmospheric noise, here we use the y-intercept of the smoothed time series, $\hat{\phi}_0$, as an estimate of α_0.

5.2 Synthetic Example

We first illustrate the LOWESS algorithm on a synthetic 3-year deformation time series with a 12-day acquisition interval (Figure 5.2). The true deformation linearly
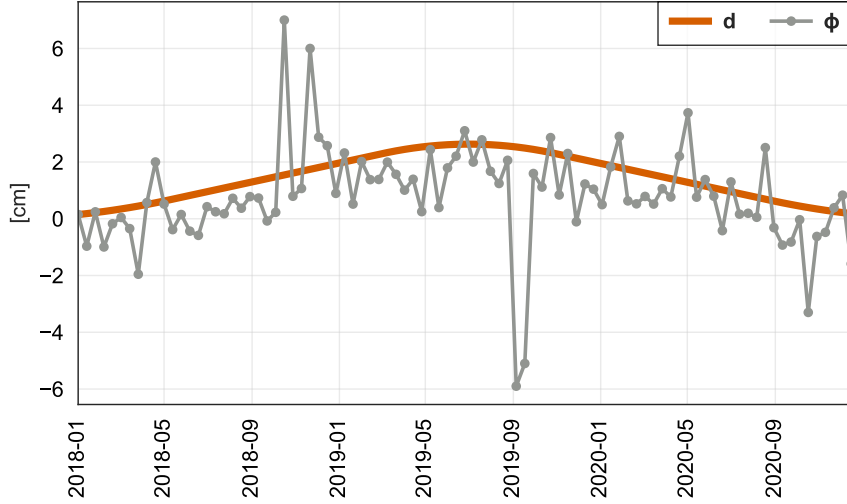
Figure 5.2: Synthetic time series for one pixel ϕ (gray) containing a combination of true deformation $\boldsymbol{d}$ (orange) and non-Gaussian tropospheric noise $\boldsymbol{\alpha}$: $\phi = \boldsymbol{d} + \boldsymbol{\alpha}$. Note that the ϕ time series is offset by an amount equal to the noise on the first date, due to the SBAS assumption that $\phi_0 = 0$.

increases to maximum of ~ 3 cm after 1.5 years and deflates back to zero by the end of 3 years. Non-Gaussian noise containing jumps of up to 8 cm is added to the deformation. The time series is shifted by the noise on the first day so that $\phi_0 = 0$, simulating the result from an SBAS inversion.

Figure 5.3 illustrates two iterations of the LOWESS algorithm the ϕ time series. During the first iteration, each $\hat{\phi}_i$ is calculated using a locally weighted regression with the weight based solely on the proximity to t_i (Figure 5.3a). The resulting fit tracks the general pattern of the data, but outlier points strongly influence the fit (Figure 5.3b). The second iteration multiplies the proximity weighting from Figure 5.3a by the residual weighting, $\boldsymbol{\delta}$, calculated from the previous iteration (Figure 5.3c). The second iteration is influenced less by the outlier points and has fewer spurious bumps in the time series (Figure 5.3d). In general, more iterations may be performed; in this example, further iterations change the fit by ~ 1 mm or less.

After subtracting ϕ_0 from all points, the results of the LOWESS estimate $\hat{\boldsymbol{\phi}}$ are shown in Figure 5.4 (green line). The LOWESS algorithm smooths away the large spikes of turbulence noise in $\boldsymbol{\phi}$ (Figure 5.4, gray) and captures most of the deformation signal (Figure 5.4, orange) For comparison, we have also linearly filtered the noisy
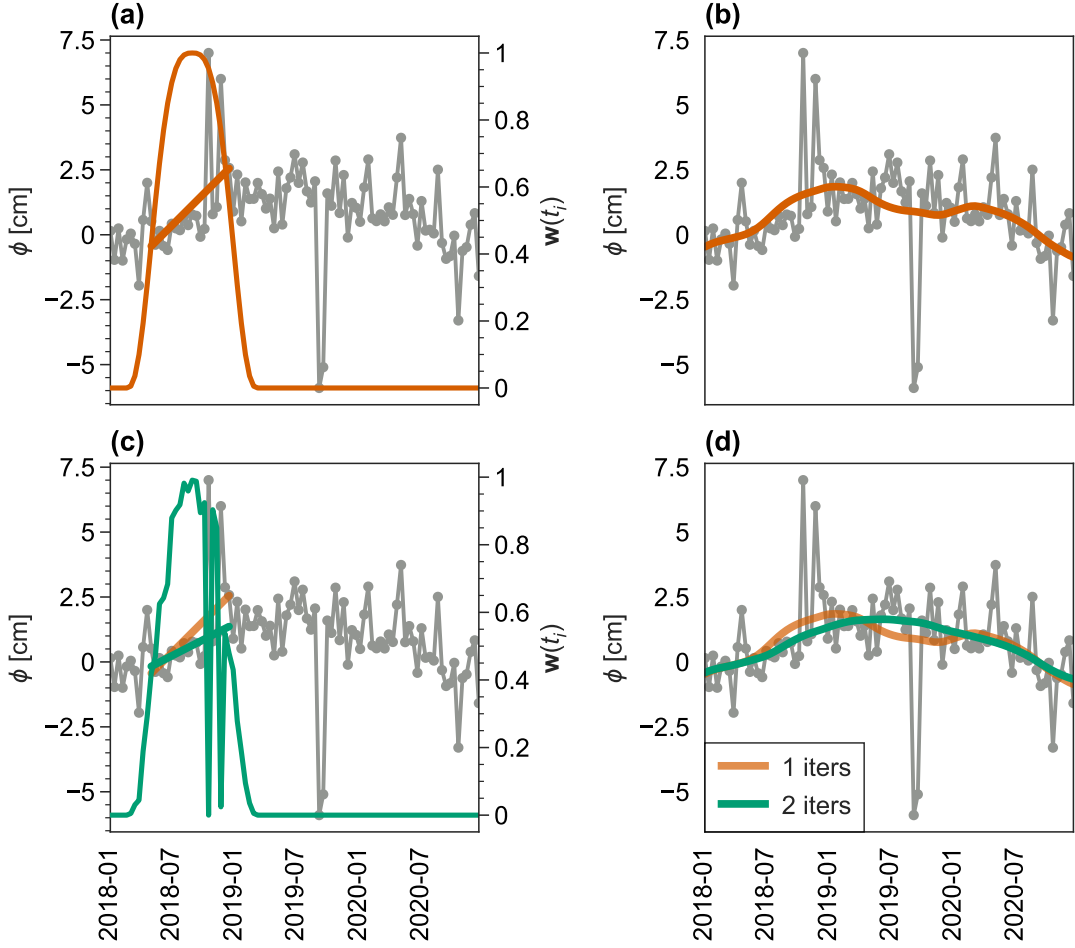
Figure 5.3: (a) First iteration of local fit at t_i, weighted by window (orange) with $\gamma = 0.4$ ($\sim$1.2 year of data). (b) First iteration of smoothed $\hat{\phi}_i$ (orange line) for all i. (c) Second iteration at t_i with the updated residual weighting. The large anomalous points have a smaller effect on the new local fit (green slope) compared to the original (orange slope). (d) Result of second iteration of LOWESS smoothing for all i (green line).
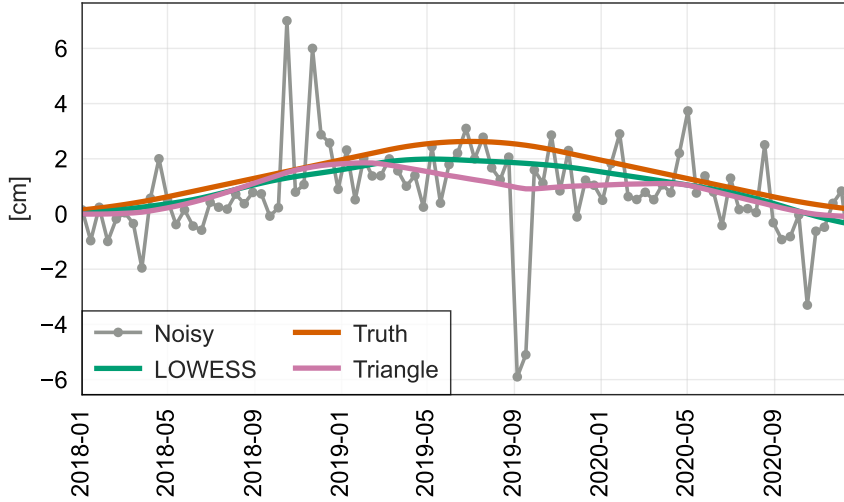
Figure 5.4:   Results of smoothing the synthetic noisy time series ϕ (gray with dots) using the LOWESS algorithm (green) and a triangle filter (pink). True deformation time series is shown in orange. Both the LOWESS algorithm and the triangle filter use 40% of the data (a filter width of $\sim$1.2 years) and have been shifted to compensate the first day's atmospheric noise.

time series with triangle filter of width 1.2 years (Figure 5.4 pink line). The triangle filter performs similarly to LOWESS when the noise is Gaussian; however, the large turbulence jumps in this example cause the triangle filter to be pulled > 2 cm away from the true deformation time series.

5.3   Sentinel-1 7-year Cumulative Surface Deformation

We demonstrate the LOWESS algorithm on real Sentinel-1 data over the Permian Basin. We processed an additional three years of data (Jan. 2019 though Dec. 2021) for Path 78 (Figure 3.5) following the processing strategy outlined in Section 3.3, for a total of 151 SAR acquisitions from Nov. 2014 to Dec. 2021 We performed an unregularized SBAS inversion to get a noisy time series ϕ for each pixel. To mitigate residual long wavelength noise from seasonal tropospheric patterns, we fit and removed a quadratic surface from the deformation map at each SAR acquisition using pixels with <2 cm of estimated deformation (Morishita et al., 2020). We then temporally smoothed each pixel using the LOWESS algorithm with a weighting window covering ≥ 2 years at all time intervals and 2 robust iterations. We similarly pro-

cessed 147 descending Path 85 SAR acquisitions to create a 7-year cumulative LOS deformation time series.

We also processed 148 SAR acquisitions from ascending Path 151 (west of Path 85) to cover the full Delaware Basin with at least 2 paths of data in all location. The Path 151 footprint does not contain GPS station TXKM that was used as the reference location for the other paths; instead, we used the technique presented in Zebker (2021) to fit and remove a phase-elevation trend from all high-coherence pixels in each interferogram and zero-reference the deformation. This method is effective for study areas where only a subset of high-coherence interferogram pixels contain significant deformation.
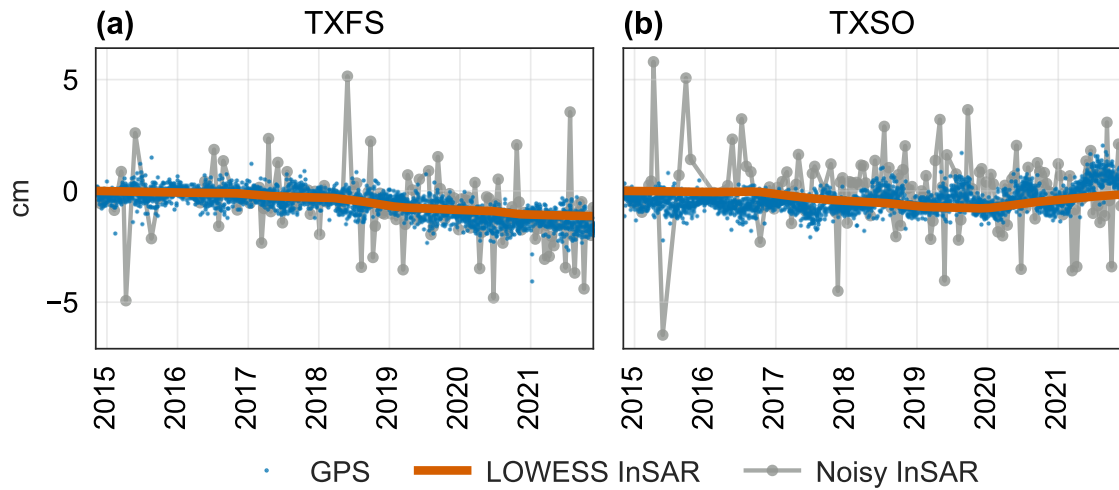
Figure 5.5:   Path 78 LOWESS smoothed algorithm (orange line) plotted against the original noisy time series (gray) at pixels near (a) station TXFS, and (b) station TXSO. GPS time series (blue dots) have been projected onto the radar LOS.

To assess the performance of the LOWESS-smoothed LOS deformation results, we projected the available GPS ENU time series onto the radar LOS. As an example, Figure 5.5a shows the LOS time series (blue dots) for GPS station TXFS. The unregularized InSAR time series (gray) contains up to 5-6 cm of tropospheric noise during the summer months. However, the LOWESS solution (orange line) is unaffected by the spikes and successfully tracks the $\sim$ 1cm of long term motion shown in the GPS data. In Figure 5.5b, the LOS time series for GPS station TXSO shows a combination of a 5-10 mm increase in LOS along with 10-15 mm of seasonal variations. While

the trend is captured by the InSAR LOWESS solution, the seasonal variations are smoothed over due to the 2 year weighting window.
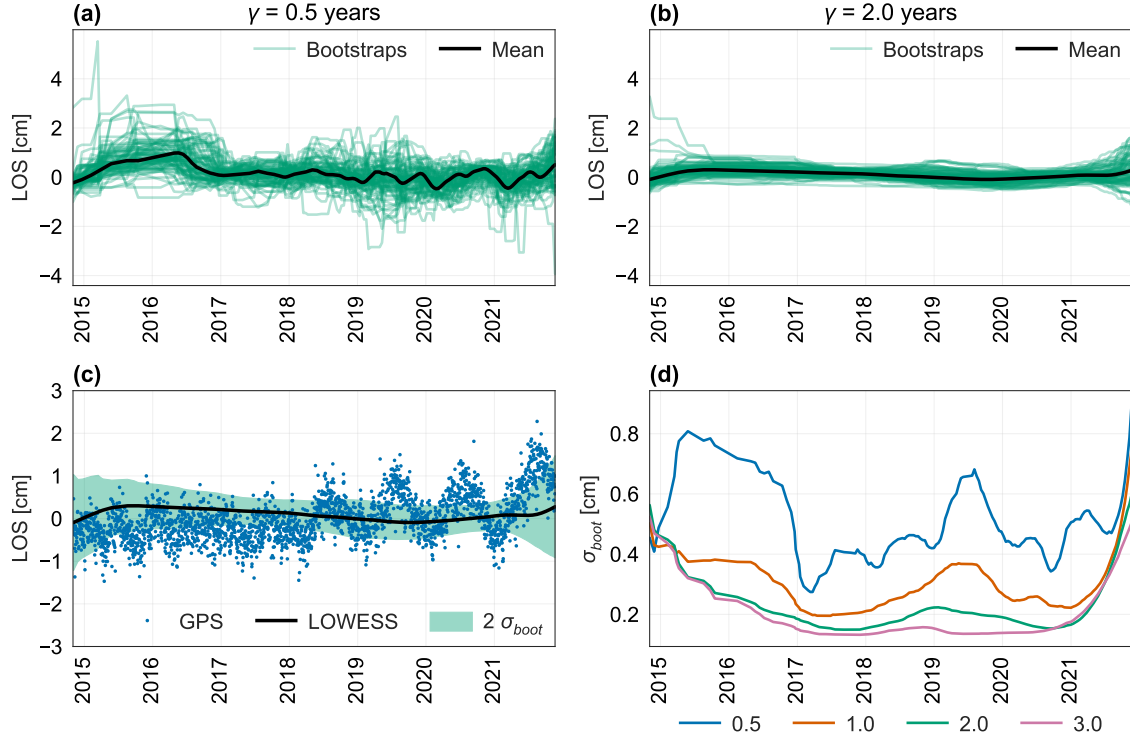
Figure 5.6: LOWESS smoothed solutions of bootstrap resampled noisy InSAR time series at GPS station TXSO using a window size of (a) $\gamma = 0.5$ and (b) $\gamma = 2$ years. Each smoothed resampling is shown as a green line, with the mean of all green lines shown in black. (c) LOWESS InSAR solution compared to GPS stations projected onto the radar LOS for the $\gamma = 2$ year case. Green shaded region shows ± 2 standard deviations as estimated by taking the standard deviation of all resampled solutions from panel (b). (d) Bootstrap estimated standard deviation of LOWESS result for $\gamma = 0.5, 1, 2$, and 3 years of smoothing.

We compared multiple choices of the LOWESS window size to determine an appropriate γ that balances the trade-off between noise reduction and temporal resolution. To estimate the variance of the LOWESS-smoothed solution, we used the bootstrap technique (Efron, 1979, Efron and Tibshirani, 1994). Bootstrapping repeatedly draws a random sample with replacement of size N from $\phi_0, \ldots, \phi_{N-1}$ and computes a quantity of interest on each resample; in our case, we perform LOWESS smoothing on each resample. Bootstrapping has been included in InSAR time series packages such as

GIAnT, MintPy, and LiCSBAS as a method of estimating uncertainty for linear deformation velocities (Agram et al., 2013, Yunjun et al., 2019, Morishita et al., 2020).

We calculated the bootstrap variance using $\gamma = 0.5$ (Figure 5.6a), $\gamma = 1.0$, $\gamma = 2.0$ (Figure 5.6b), and $\gamma = 3.0$ using InSAR data near GPS station TXSO. The variance of the LOWESS smoothing on all resamples (green lines) indicates that using a smaller window (Figure 5.6a) leads to a noisier deformation solutions than a larger window (Figure 5.6b). Since the variance starts to converge after a 2 year window (Figure 5.6d), we chose $\gamma = 2$ for our deformation solutions. Note that as γ increases, the variance in the middle of the time series drops more quickly than at the end points. As with other linear fitting procedures, the uncertainty of the LOWESS estimated slopes propagates into a larger uncertainty at the end points of the data.

The full set of GPS comparisons for Path 78 is shown in Figure 5.7. The additional 3 years of Sentinel-1 data allow for an additional two station comparisons (at TXM5, TXB8) for a total of 15 stations within the Path 78 footprint. There is an average of 3 mm RMS difference between the smoothed GPS time series and the InSAR LOWESS solutions for all time steps across the 15 stations, and a maximum absolute difference of 1.3 cm at any time point (including seasonal variations).
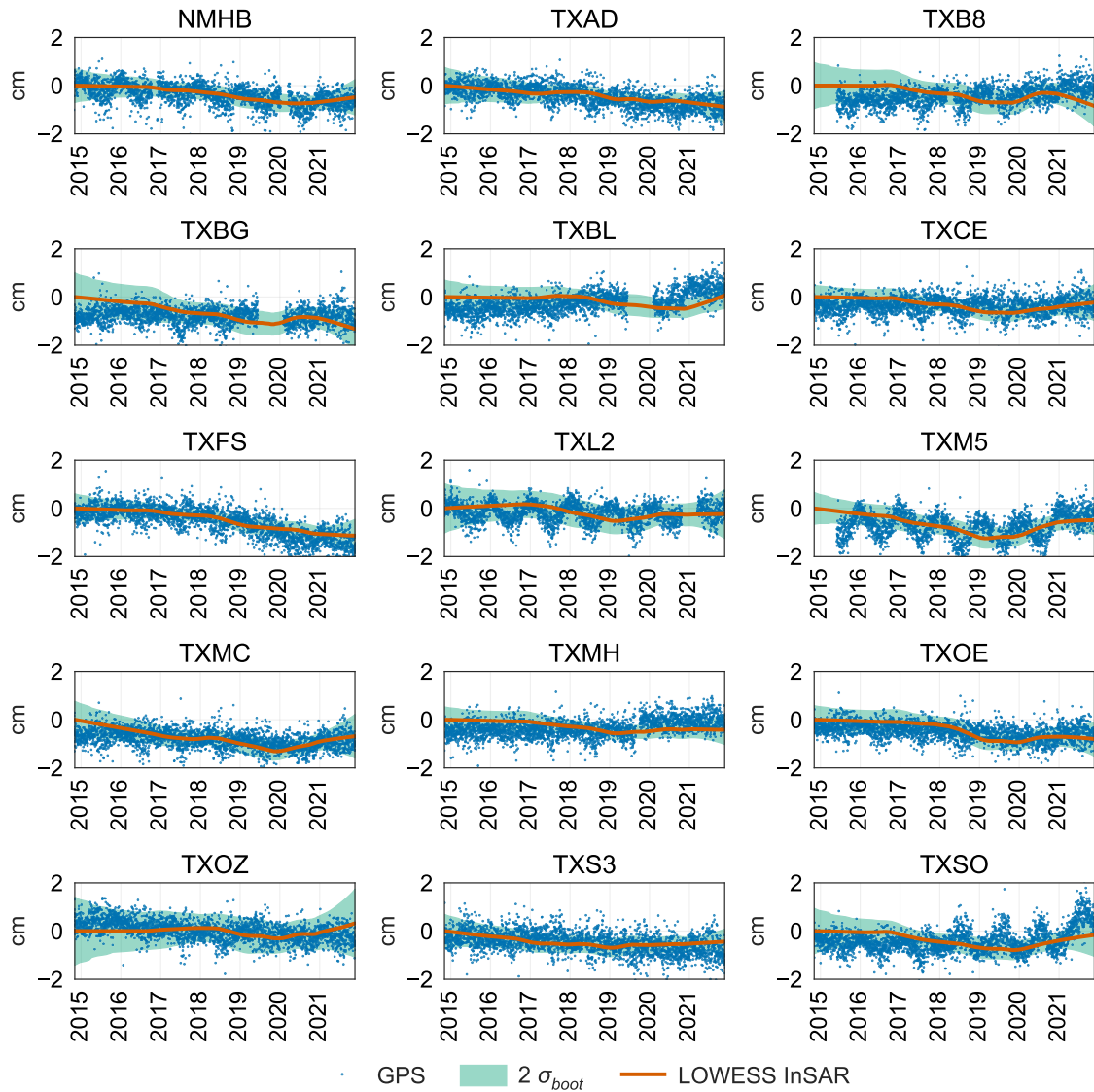
Figure 5.7: Comparison of permanent GPS stations projected onto the radar LOS (blue dots) with Path 78 LOWESS smoothed algorithm (orange lines). Green shaded region shows ± 2 standard deviations as estimated by bootstrap resampling.
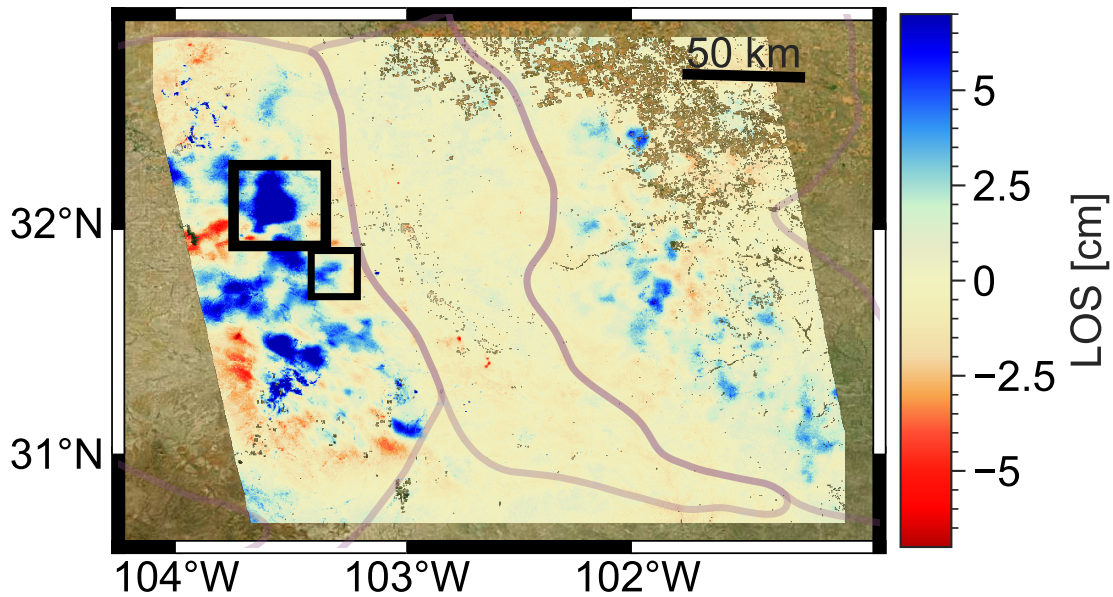
Figure 5.8: Cumulative LOS deformation from Nov. 2014 to Dec. 2021 (ascending Path 78). Blue areas indicate motion away from the satellite (subsidence or eastward). Areas with low correlation have been masked. Black boxes indicate the zoomed-in locations for Figure 5.9 panels (a) and (c). Purple outlines indicate (from west to east) the Delaware Basin, Central Basin Platform, and Midland Basin.

Figure 5.8 shows the 7-year cumulative LOS deformation map for Path 78, where areas with low average spatial coherence (< 0.2) or temporal coherence < 0.75 are masked. While many spatial patterns present in Figure 5.8 are also visible in the 4-year deformation map (Figure 4.5), there are several notable deformation rate changes between the 2015-2018 period and the 2019-2021 period. For example, near the SWD wells identified in Kim and Lu (2018) (Figure 5.9a), there was steady surface uplift as injection volume increased from 2015-2018. After one of the injection wells (API 49533675) shut down operations after 2018, there was a gradual deflation for the next three years (Figure 5.9b). In the northern Delaware Basin, many subsidence patterns present in the 4-year cumulative maps show accelerating rates of subsidence as oil production volumes increased through 2020. For example, a subsidence bowl on the New Mexico side of the TX-NM border (Figure 5.9c) subsided 4-5 cm for the four years of 2015-2018. As both oil and water production increased in the surrounding wells, the subsidence rate increased to > 5 cm per year.
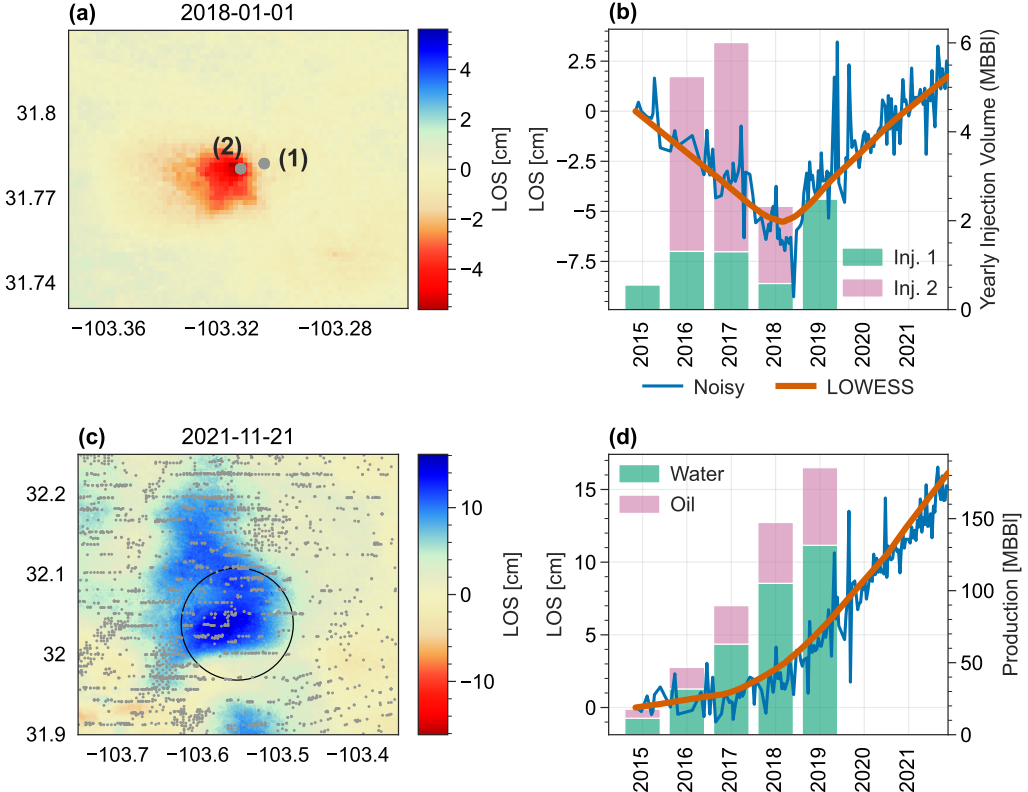
Figure 5.9: (a) Cumulative LOS deformation for ascending Path 78 through Jan. 2018 using LOWESS smoothing algorithm. Red (negative LOS) indicates motion toward the satellite. Grey dots show the locations of salt water disposal wells (Well 1: API 49530150, Well 2: API 49533675). (b) Time series within uplift in panel (a) showing SBAS time series ϕ (blue) and LOWESS result (orange). Green and pink bars show the annual injection volume of wells 1 and 2, respectively, indicating that Well 2 shut down injection operations after 2018. (c) Cumulative LOS deformation for ascending Path 78 from Nov. 2014 to Dec. 2021. Grey dots indicate the location of oil or water production wells that were active between 2014 and 2019. (d) ϕ (blue) and LOWESS result (orange) for InSAR data in the circle region in panel (c). Annual production volumes of water (green) and oil (pink) for all wells contained in circle of panel (c). Well-level production data was unavailable for 2020-2021.
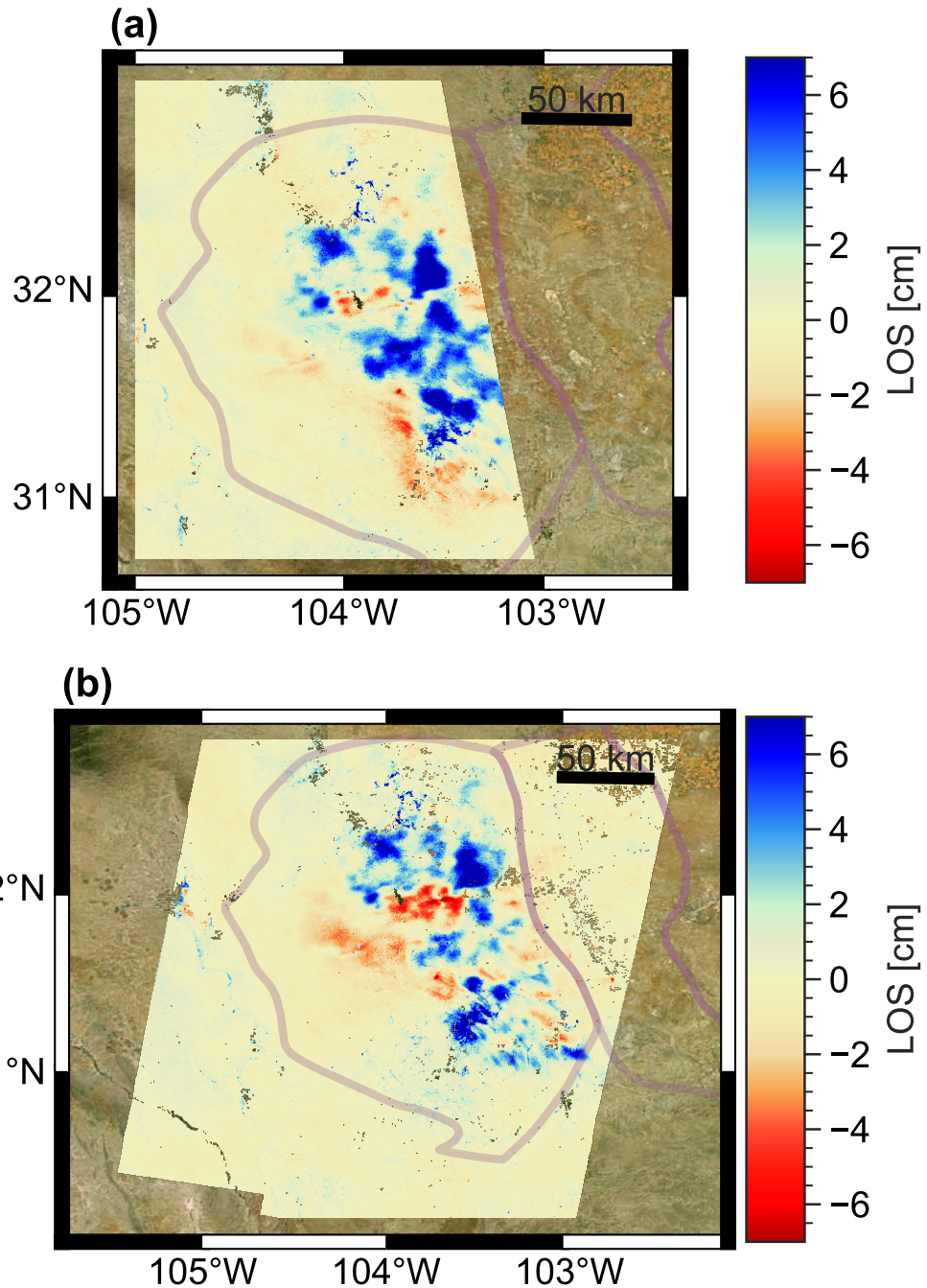
Figure 5.10:   Cumulative LOS deformation from Nov. 2014 to Dec. 2021 for (a) ascending Path 151 and (b) descending Path 85. Blue areas indicate motion away from the satellite, areas with low correlation have been masked. Purple outlines indicate (from west to east) the Delaware Basin, Central Basin Platform, and Midland Basin.

In addition to the LOS decomposition using Paths 78 and 85 described in Section 4.1.3, we performed a second LOS decomposition using the cumulative deformation of descending Path 85 (Figure 5.10a) and ascending Path 151 (Figure 5.10b). We merged the two decompositions by averaging their region of overlap, and we cropped the maps to the western contour of the Delaware Basin to obtain continuous vertical (Figure 5.11a) and eastward (Figure 5.11b) deformation solutions. Note that the two vertical and eastward decompositions show sub-centimeter agreement: the merged deformation maps contain no visible artifacts at the path boundaries despite incorporating data from independent SAR acquisitions.
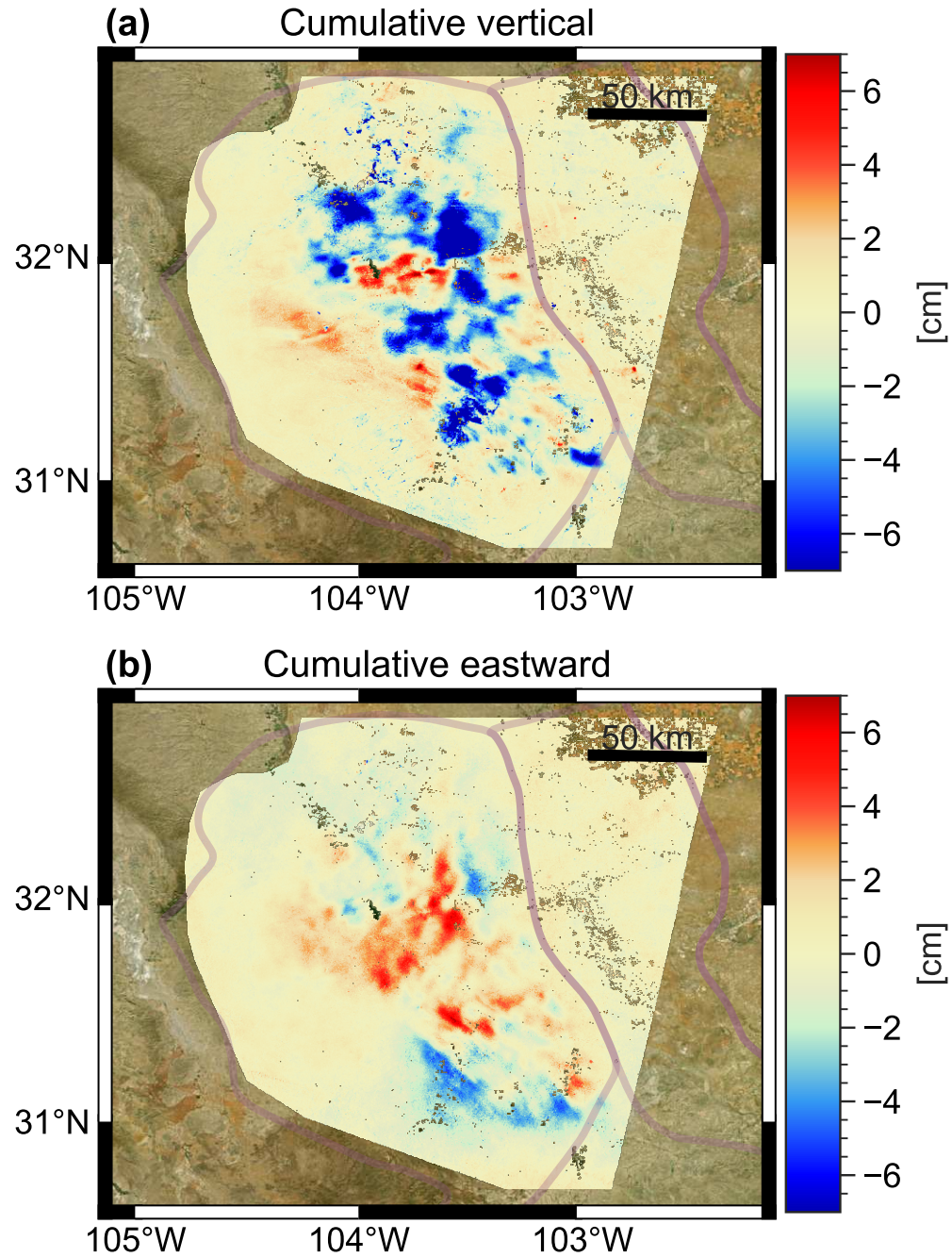
Figure 5.11: Cumulative (a) vertical and (b) eastward deformation from Nov. 2014 to Dec. 2021. Blue areas indicate subsidence (westward motion in panel (b)), red indicates uplift (eastward). Purple outlines indicate the Delaware Basin (to the west) and Central Basin Platform (east).
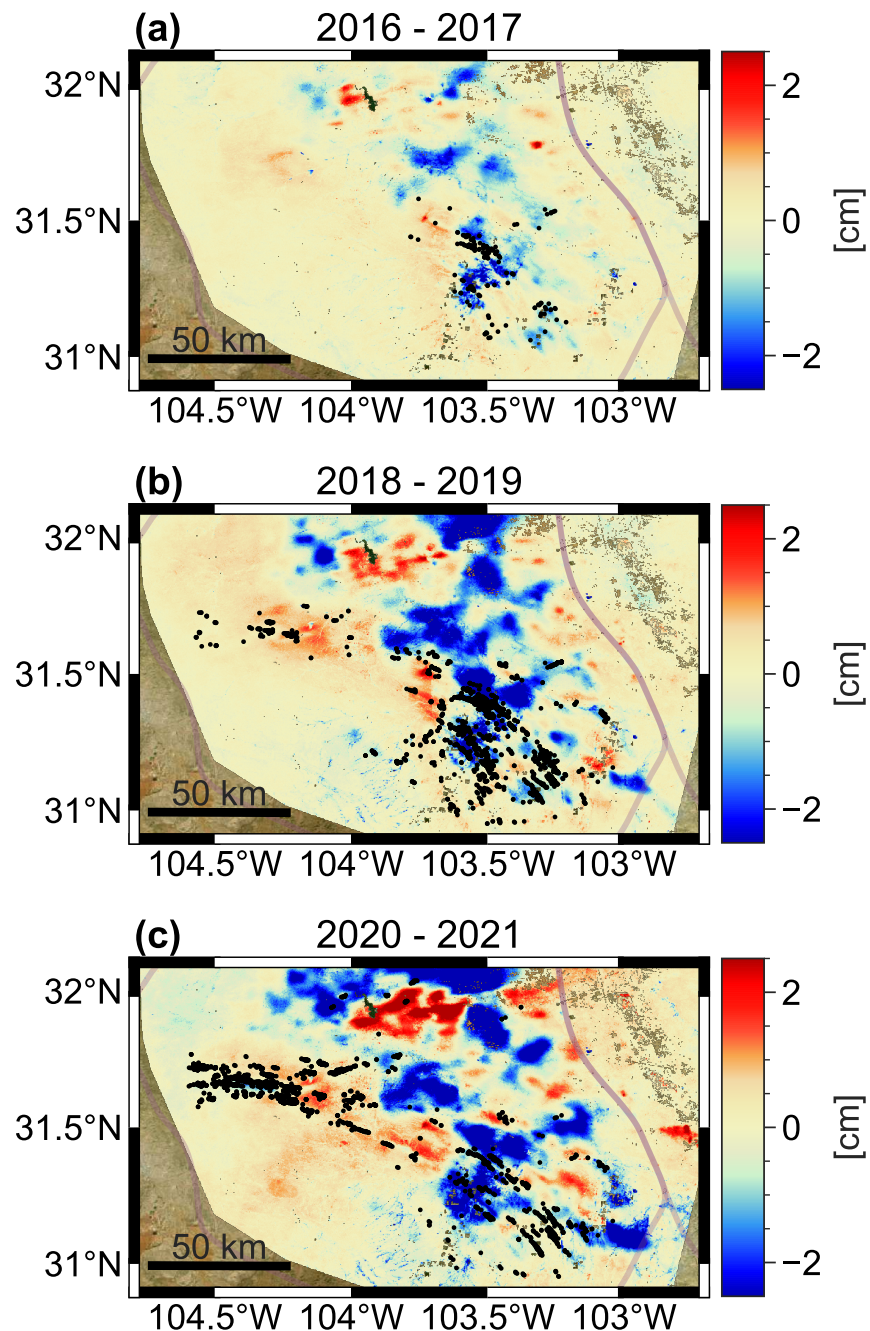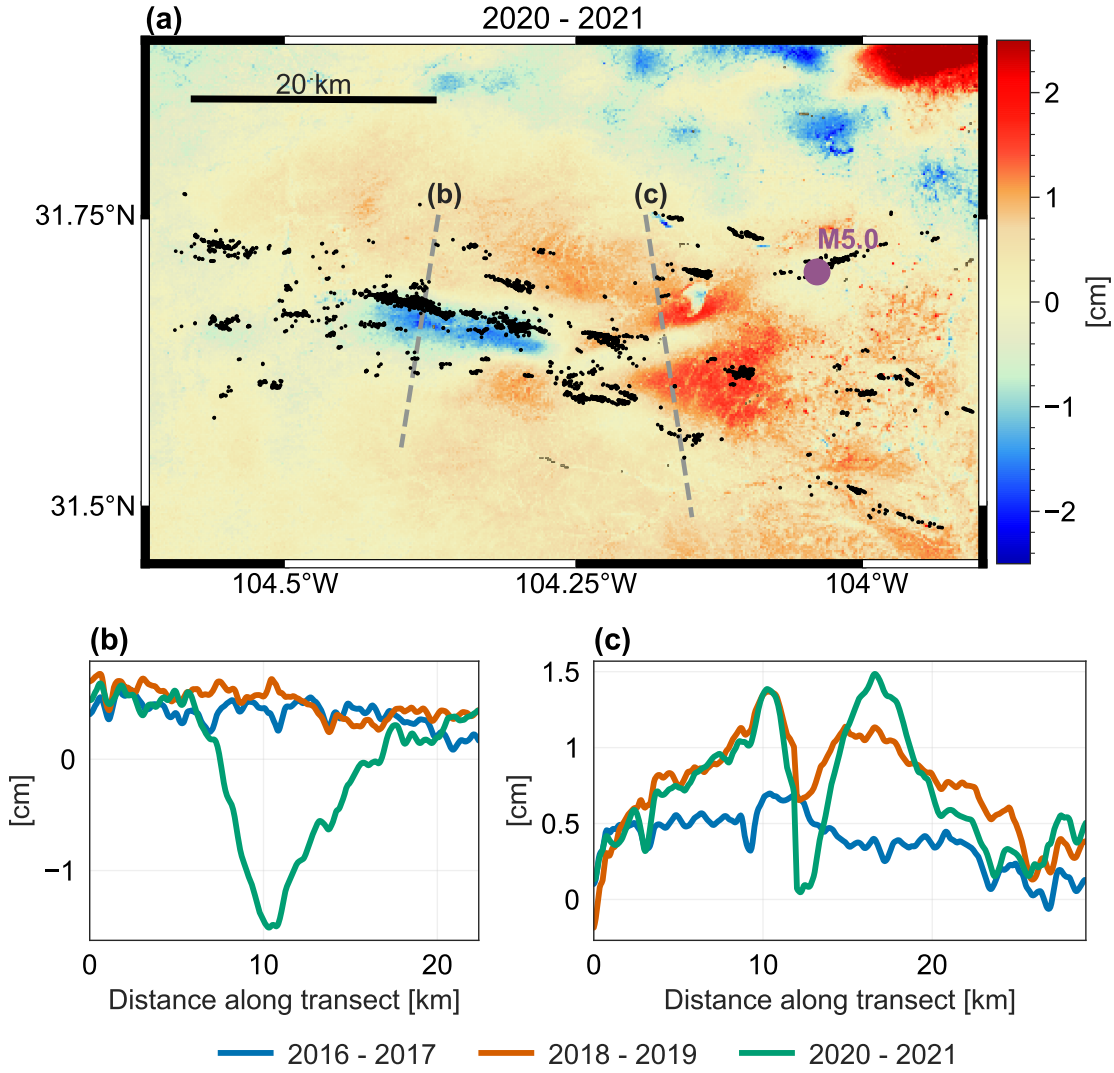
Figure 5.12: InSAR-derived vertical surface deformation for the two-year intervals of 2016-2017 (a), 2018-2019 (b), and 2020-2021 (c). Hypocenters of >M2.0 earthquakes recorded by TexNet (2017 and later) are shown as black dots. The hypocenters pictured are from the high-resolution catalog (availabe at https://hirescatalog.texnet.beg.utexas.edu/) that were relocated using GrowClust (Trugman and Shearer, 2017).

By examining two-year increments of the cumulative LOWESS time series, we observe changes to the spatial deformation patterns (Figure 5.12). We divide the data into two-year intervals to match our choice of smoothing window size γ. During 2016-2017 (Figure 5.12a), the largest subsidence occurred in the southern portion of the Delaware Basin. In this region, linear deformation features are visible near an earthquake cluster recorded by TexNet. The volumes of oil production and wastewater injection increased during 2018-2019 (Figure 5.12b), leading to substantially more total uplift and subsidence. During this period, we observe 2-3 cm of uplift in areas where Ge et al. (2022) modeled an increase in pore pressure within the Delaware Mountain Group due to wastewater disposal. We also observe an uplift pattern near a new cluster of earthquakes in the western portion of the Delaware Basin within the Culberson-Mentone Earthquake Zone (CMEZ, Hennings et al. (2021)). The CMEZ contained the largest increase in recorded earthquakes during the 2020-2021 period (Figure 5.12c), including the M5.0 Mentone earthquake (Skoumal et al., 2020b).

The surface deformation in the CMEZ during 2020-2021 contains multiple linear patterns aligning with clusters of earthquakes (Figure 5.13). For example, there was 1.5-2 cm of subsidence along transect (b) (Figure 5.13) which showed no deformation prior to 2020. Previous studies have suggested that faults within the southern Delaware Basin are producing linear deformation patterns due to aseismic slip (Pepin et al., 2022); however, further modeling is needed to attribute causes to the most recent deformation in the western Delaware Basin.

.

Figure 5.13: (a) Vertical surface deformation and TexNet recorded earthquakes (black dots) for during 2020-2021 in the Culberson-Mentone Earthquake Zone (CMEZ). The M5.0 earthquake (purple dot) occurred on March 26, 2020. Vertical surface deformation along transects (dashed lines) are shown in panels (b) and (c) for two-year intervals of 2016-2017 (blue), 2018-2019 (orange), and 2020-2021 (green). Both transects run from north to south as distance increases.

Chapter 6

Automatic Detection of InSAR Surface Deformation Signals in the Presence of Severe Tropospheric Noise

Automatic detection of surface deformation features from a large volume of Interferometric Synthetic Aperture Radar (InSAR) data is challenging, because the magnitude of InSAR measurement noise varies substantially in both space and time. In this chapter, we present a computer vision algorithm based on Laplacian of Gaussian (LoG) filtering for detecting the size and location of unknown surface deformation features. Because our algorithm detects spatially coherent "blob-like" features, tropospheric noise artifacts that share similar spatial characteristics may also be detected. We estimate the tropospheric noise spectrum directly from data, which allows us to simulate new instances of noise that resemble the actual InSAR observations. Based on these simulations, we quantify the likelihood that a detected feature is a real deformation signal. We demonstrate the performance of our algorithm using ascending and descending Sentinel-1 data from Chapter 4 acquired between 2014 and 2019. We detect clusters of deformation features associated with oil production, wastewater injection, and fault activities. The number of detected deformation features increases substantially over the study period, which is consistent with the overall rise in oil production within the Permian Basin since 2014.

6.1 Algorithm

6.1.1 Automatic Feature Detection

Given a surface deformation map M derived from InSAR data, the value M_{ij} at the ith row and j^{th} column represents the magnitude of a cumulative, seasonal, or transient deformation signal at this pixel. Because the earth can be considered as a stratified elastic-viscoelastic medium, surface deformation features are often spatially coherent (Segall, 2010). In this study, our goal is to automatically detect these features in an InSAR deformation map M that covers a very large region (Algorithm 1).

There have been many computer vision algorithms that were designed to automatically detect spatially coherent "blob-like" features in 2D image data (Lindeberg,
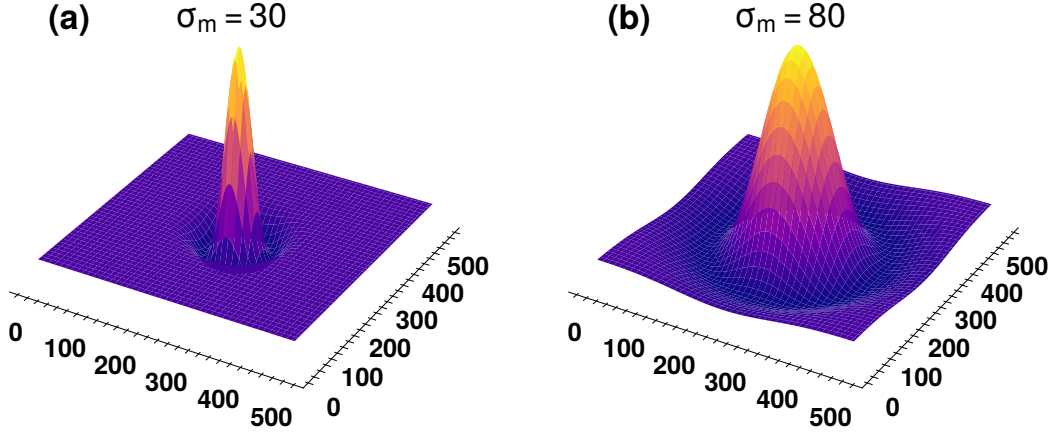
Figure 6.1: Laplacian of Gaussian (LoG) kernels with (a) $\sigma_m = 30$ pixels and (b) $\sigma_m = 80$ pixels for an image of size of 500-by-500 pixels.

1993; 1998, Lowe, 2004). In this study, we employ the Laplacian of Gaussian (LoG) filters as a blob detector. An LoG kernel $K^{(m)}$ with a size σ_m is written as:

$$K_{ij}^{(m)} = \left(\frac{(i-l)^2 + (j-l)^2 - 2\sigma_m^2}{2\pi\sigma_m^4} \right) e^{-\frac{(i-l)^2+(j-l)^2}{2\sigma_m^2}} \tag{6.1}$$

where pixel indices $ij \in \{0, 1, \ldots, 2l\}$. The unit of σ_m is given in pixels, which can be scaled to meters based on the pixel spacing of the InSAR deformation map M.

We generate a set of LoG kernels $K^{(1)}, K^{(2)}, \ldots$ with progressively larger σ_m (Figure 6.1), and calculate the mth filter response $L^{(m)}$ as:

$$L^{(m)} = M * K^{(m)} \tag{6.2}$$

Here $*$ denotes the 2D discrete convolution, which is typically computed using the Fast Fourier Transform (FFT) algorithm because of its superior computational efficiency (Szeliski, 2022).

To demonstrate how to estimate the size of an unknown deformation feature from the filter responses, Figure 6.2 (a) shows a 500×500 synthetic deformation map M that contains one Gaussian-shaped uplift feature in the upper left and one elliptical Gaussian subsidence feature in the lower right. We filtered this deformation map
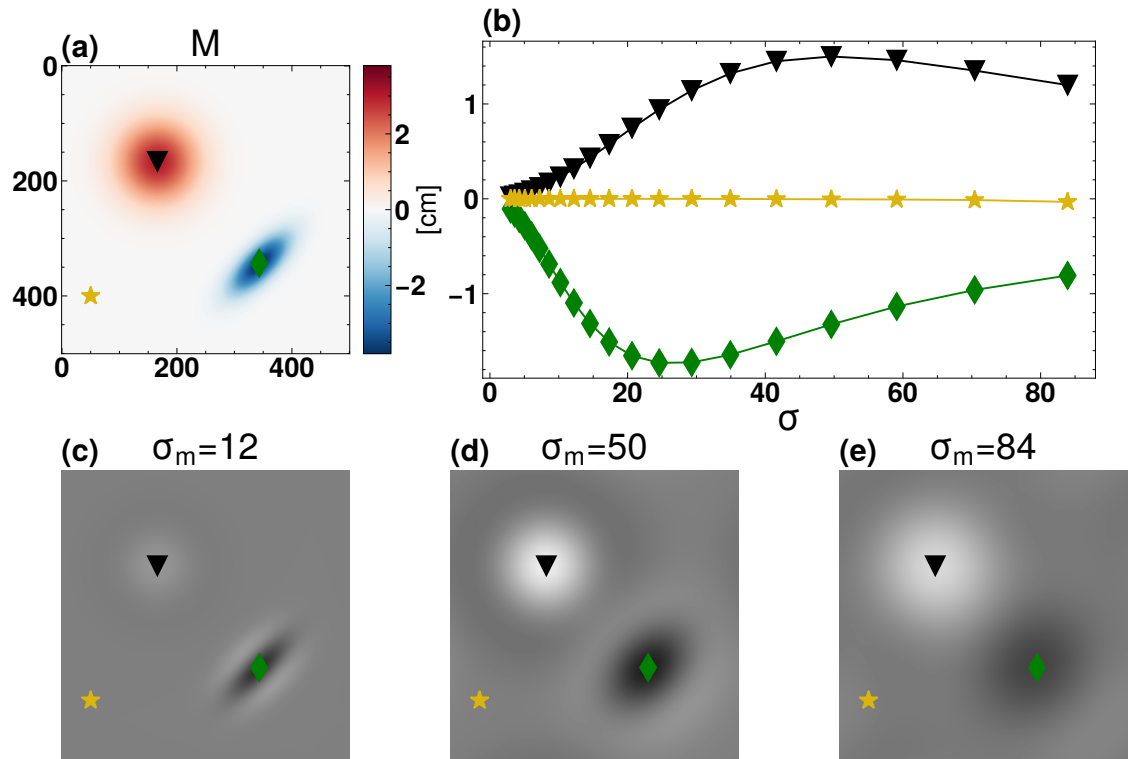
Figure 6.2: (a) A synthetic deformation map that contains one Gaussian-shaped uplift feature in the upper left and one elliptical Gaussian subsidence feature in the lower right. (b) LoG response amplitudes for 20 filters with various sizes (σ_m) at three marker points. The marker locations are shown in panel (a). (c)-(e) The LoG filter responses for $\sigma_m = 12$, 50, and 84.

using 20 LoG kernels of sizes ranging from $\sigma_1 = 3$ pixels to $\sigma_{20} = 100$ pixels with a base-2 logarithmic spacing, and the filter responses are shown in Figure 6.2 (b)-(e). For the round uplift case, the filter response $L^{(m)}$ (the black curve in Figure 6.2 (b)) is strongest when the kernel size σ_m matches the deformation feature radius r as $r = \sqrt{2}\sigma_m$. This is known as the extreme point, or the local maximum points of $|L^{(m)}|$ for all attempted σ_m. For the elliptical subsidence case, the extreme point is reached when the average length of the two primary axes of the deformation feature is $\sim \sqrt{2}\sigma_m$ (the green curve in Figure 6.2 (b)). For the case of no deformation, no substantial filter response is generated for any filter size (the gold curve in Figure 6.2 (b)).

In the case that two candidate blobs have more than 50% overlapping area, the blob with a smaller size is discarded. Additionally, the LoG filter may falsely flag ghost blobs at the edges of real deformation features. This is because deformation features with strong curvature at the center also contain a strong opposite-signed curvature near the border (Lindeberg, 1998). To remove those false positives, we use the distance from the candidate blob's center location to the nearest deformation amplitude extremum as a measure. If this distance is close to the blob radius, the detection is likely a ghost blob. In our test case, we discarded blobs with local extremum distances larger than 75% of the blob radius, which effectively removed all visible false positives near the edge of real deformation features.

For the kth detected deformation feature, our algorithm outputs the blob center location (i_k, j_k), the blob radius r_k, the filter response magnitude $|g_k|$ at the extreme point, and the deformation magnitude $|\bar{d}_k|$ defined as the weighed maximum of all pixels within the kth blob:

$$\bar{d}_k = \max_{kk} |w_{kk} M_{kk}| \tag{6.3}$$

Here the weight w_{kk} equals $\exp\left[-(r_{kk}/r_k)^2\right]$, where r_{kk} is the distance between a pixel within the blob and the blob center. The exponential weighting prevents pixel outliers from distorting the measure of feature magnitude.

We can exclude undesired deformation features by setting magnitude thresholds on $|g_k|$ and $|\bar{d}_k|$ based on users' interest. Furthermore, we need to determine whether a detected deformation feature has a signal magnitude above the noise level of the InSAR deformation map, which is the focus of the following method sections.

Input: 2D InSAR deformation map M

Result: For each $k \in 1, \ldots, N_d$ detections, the algorithm outputs the blob center location (i_k, j_k), the blob radius r_k, the filter response magnitude $|g_k|$ at the extreme point, the deformation magnitude $|\bar{d}_k|$

// Calculate filter responses:

foreach $\sigma_m \in \{\sigma_{min} \ldots \sigma_{max}\}$ **do**
| $L^{(m)} = M * K^{(m)}$
end

// Find candidate blobs from local extrema:

for $(i, j, m) \in L$ **do**
| **if** $L[i, j, m]$ *is local extremum* **then**
| | Compute $r = \sqrt{2}\sigma_m$
| | Add (i, j, r) to list of candidate detections
| **end**
end

// Prune blobs with overlap:

foreach $b_1 := (i_1, j_1, r_1), b2 := (i_2, j_2, r_2) \in candidates$ **do**
| **if** $Overlap(b_1, b_2) > 0.5$ **then**
| | Remove smaller of b_1, b_2
| **end**
end

// Prune edge blob false positives:

foreach $b_k := (i_k, j_k, \sigma_k) \in candidates$ **do**
| Find coordinates (u, v) of local max of M within radius r_k around (i_k, j_k)
| **if** $\sqrt{(x - u)^2 + (y - v)^2} > 0.75$ **then**
| | Discard b_k
| **end**
end

// Prune with thresholds γ_g, γ_d:

foreach $b_k := (i_k, j_k, r_k, |g_k|, |\bar{d}_k|) \in candidates$ **do**
| **if** $|g_k| < \gamma_g$ *or* $|\bar{d}_k| < \gamma_d$ **then**
| | Discard b_k
| **end**
end

Algorithm 1: LoG Based Deformation Feature Detection

6.1.2   Tropospheric Noise Spectrum

InSAR measurement noise can also produce spatially coherent "blob-like" features that are detectable by our algorithm. Here we focus on characterizing the tropospheric turbulence noise in each SAR scene. This is because tropospheric turbulent noise (1) is correlated in space (Emardson et al., 2003, Lohman and Simons, 2005); (2) is present in all InSAR data sets with greatly varying magnitudes (Barnhart and Lohman, 2013, Hooper et al., 2012); and (3) is often the primary noise source that limits InSAR measurement accuracy (Jolivet et al., 2014, Bekaert et al., 2015a, Parker et al., 2015).

Consider an interferogram formed using two SAR scenes acquired at times t_1 and t_2. In the case that tropospheric turbulence noise is the dominant noise term, the measured interferometric phase $\Delta\phi_{1,2}$ (in radians) at a pixel of interest can be written as (Zebker et al., 1997):

$$\Delta\phi_{1,2} \approx \frac{4\pi}{\lambda} \left(\alpha_2 - \alpha_1 + \Delta d_{1,2} \right) \tag{6.4}$$

where λ is the radar wavelength, α_1 and α_2 represent the tropospheric delay at the two SAR acquisition times t_1 and t_2, and $\Delta d_{1,2}$ is the Line-Of-Sight (LOS) deformation $(d_2 - d_1)$ between t_1 and t_2. The units of λ, α_1, α_2, and $\Delta d_{1,2}$ are centimeters.

Given N SAR acquisitions, we can estimate the tropospheric noise on the nth SAR acquisition date by averaging $N-1$ interferograms that share the common reference SAR scene n (Tymofyeyeva and Fialko, 2015):

$$\bar{\alpha}_n = \frac{\lambda}{4\pi} \frac{1}{N-1} \left(\sum_{k=1,k\neq n}^{N} \Delta\phi_{k,n} \right) = \alpha_n + \frac{1}{N-1} \left(\sum_{k=1,k\neq n}^{N} \Delta d_{k,n} - \sum_{k=1,k\neq n}^{N} \alpha_k \right) \tag{6.5}$$

Because tropospheric turbulence noise is uncorrelated in time for scales longer than one day (Emardson et al., 2003, Onn, 2006), the term $\frac{1}{N-1}\sum \alpha_k \rightarrow 0$ when N is sufficiently large. Under the assumption that $\frac{1}{N-1}\sum \Delta d_{k,n}$ is relatively small comparing to α_n, we compute $\bar{\alpha}_n$ at each pixel to obtain a tropospheric turbulence noise map $A^{(n)}$ for the nth SAR acquisition date over the entire study area. In Section 6.3.1, we further discuss the impact of the deformation signals on our tropospheric noise analysis.

We next compute the 2D Power Spectral Density (PSD) of the nth tropospheric

noise estimates at wavenumber k_x, k_y (with units $1/m$) as (Jacobs et al., 2017):

$$\text{PSD}_n(k_x, k_y) = \frac{|\widehat{A^{(n)}}|^2}{N_x N_y (\frac{1}{\Delta x \Delta y})} \tag{6.6}$$

where $\widehat{A^{(n)}}$ is the Discrete Fourier transform (DFT) of the nth tropospheric noise map $A^{(n)}$, Δx and Δy are the interferogram pixel spacings (in meters) in the x and y directions, N_x and N_y are the total number of pixels in the x and y directions, and the squared absolute value and division are pixel-wise operations.

As an example, Figure 6.3 (a) shows a synthetic 2D tropospheric turbulence noise map. We calculate the 2D PSD of the noise map following Equation (6.6) (Figure 6.3 (b)). Under the assumption that tropospheric noise is isotropic, we average all pixels with a distance $k = \sqrt{k_x^2 + k_y^2}$ from the origin to generate a 1D PSD as a function of k (Hanssen, 2001). We plot the 1D PSD on a log-log scale, which rolls off following a power law at higher frequencies (Figure 6.3 (c)). By contrast, the power spectrum of spatially uncorrelated while noise is relatively flat across all frequencies k (Figure 6.3 (d)-(f)).
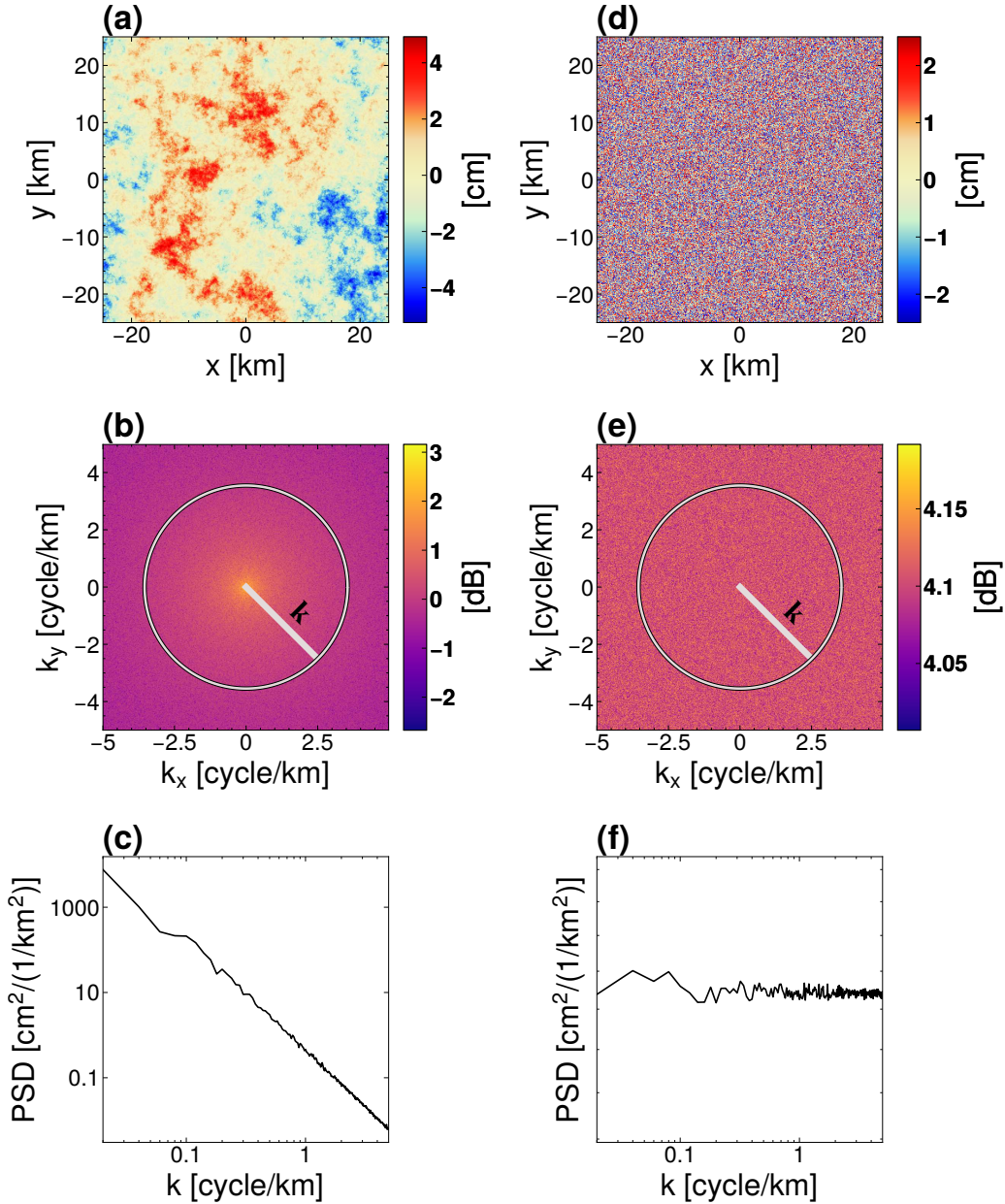
Figure 6.3: (a) A simulated 2D turbulent atmospheric noise map with $500{\times}500$ pixels at 100 meter pixel spacing. (b) 2D Power Spectral Density (PSD) of the tropospheric noise map in panel (a). (c) 1D PSD as a function of wavenumber $k = \sqrt{k_x^2 + k_y^2}$, under the assumption that tropospheric noise is isotropic. (d) A simulated 2D white noise map (spatially uncorrelated) with the same dimension and pixel spacing as panel (a) (e) 2D PSD of the white noise map in panel (d). (f) 1D PSD as as a function of wavenumber $k = \sqrt{k_x^2 + k_y^2}$. Here we averaged the 1D PSD of 50 2D white noise instances to improve the statistical stability of the spectral estimates.

6.1.3 Uncertainty Quantification

Using the average 1D PSD of all N InSAR-observed tropospheric turbulence noise maps, we can simulate N 2D noise incidences $S^{(1)}, \ldots, S^{(N)}$ that closely resemble the real tropospheric noise over the study area (Hanssen, 2001). Using these simulated noise maps, we form up to $N(N-1)/2$ noise-only interferograms, and derive a time series solution following the same method for generating the real InSAR deformation map M (e.g. (Sandwell and Price, 1998, Berardino et al., 2002)). Because these synthetic interferograms contain no deformation, any "blob-like" features in the simulated time series solution are associated with tropospheric noise. We record the radius r_k, the filter response magnitude $|g_k|$ and the magnitude $|\bar{d}_k|$ of each noise feature using our automatic blob detection algorithm.

Similarly, we generate many synthetic InSAR data sets that share the same noise spectrum derived from data, and record all detected noise blobs. We create 2D histograms of the noise attributes (filter response magnitude vs. radius and deformation magnitude vs. radius), which allows us to remove candidate blob features in the real deformation map M that are likely due to tropospheric noise artifacts.

6.2 Test Site

We tested our automatic detection algorithm using three cumulative LOS deformation maps (Nov. 2014 to Jan. 2017, Jan. 2018, and Jan. 2019) derived from 84 Sentinel-1 acquisitions from ascending Path 78 (see Figure 4.5(a) in Chapter 4). For each SAR acquisition date used to create the deformation maps, we estimated the tropospheric turbulence noise using all interferograms that contain the SAR scene based on Equation (6.5). We removed a quadratic ramp in each noise map, and we calculated the average 1D PSD of all 84 noise maps as described in 6.1.2. Using the average noise spectrum, we generated 29 synthetic noise maps, which corresponds to the 29 Sentinel-1 acquisition dates between November 2014 and January 2017. We formed noise-only synthetic interferograms and calculated the cumulative stacking solution through the stacking method (Equation (4.1)).

We ran our blob detection algorithm on the noise-only stacking solution, and we recorded the size, the filter response magnitude, and the magnitude of each noise blob feature. We repeated this process until the number of recorded detections exceeded

100,000. We smoothed the resulting histograms using a kernel density estimate (KDE) (Scott, 2015) and generated 2D empirical Probability Density Functions (PDFs) of the noise attributes for the November 2014-January 2017 cumulative LOS deformation map. Similarly, we ran additional simulations to generate 2D histograms of the noise attributes for the November 2014-January 2018, and November 2014-January 2019 cumulative deformation maps. These histograms were then used to remove candidate blob features in the real Sentinel-1 InSAR deformation maps that are likely due to tropospheric noise artifacts.

We also tested the detection algorithm using in the three descending cumulative deformation maps spanning November 2014 to January 2017, January 2018, and January 2019 data derived from 81 SAR acquisitions from Path 85 (Figure 4.5(b)). We characterized the tropospheric noise from InSAR data, and identified deformation features in the cumulative deformation maps that are likely real.

6.3 Results and Discussion

6.3.1 Path 78 Detections

Figure 6.4 (a)-(c) shows three estimated tropospheric noise maps for Sentinel-1 ascending Path 78 acquisitions 2017-12-12, 2018-09-14, and 2017-06-15. We observe blob-like turbulence features ranging from a few kilometers up to tens of kilometers in diameter, and the magnitude of the tropospheric turbulence noise varies substantially on different days (Figure 6.4 (d)). For example, the maximum absolute tropospheric noise observed on 2017-12-12, 2018-09-14, and 2017-06-15 are 1.8 cm, 3.2 cm, and 12.6 cm, respectively. Overall, $\sim 50\%$ of Path 78 scenes were acquired in quiet atmospheric conditions with a maximum noise level under 4 cm. Approximately, 35% scenes were acquired in moderate turbulence conditions (a maximum noise level of 4-10 cm), and 15% scenes were acquired in strong turbulent noise conditions (a maximum noise level of 11-15 cm).

Because InSAR phases are measured with respect to a reference point, we calculated tropospheric noise estimates relative to the center of the map (the noise reference point). We plotted the mean absolute tropospheric noise vs. distance to the noise reference point (Figure 6.4(e)). For the majority of the Path 78 acquisitions, tropospheric turbulent noise increases as the square root of the distance for the first ~ 50
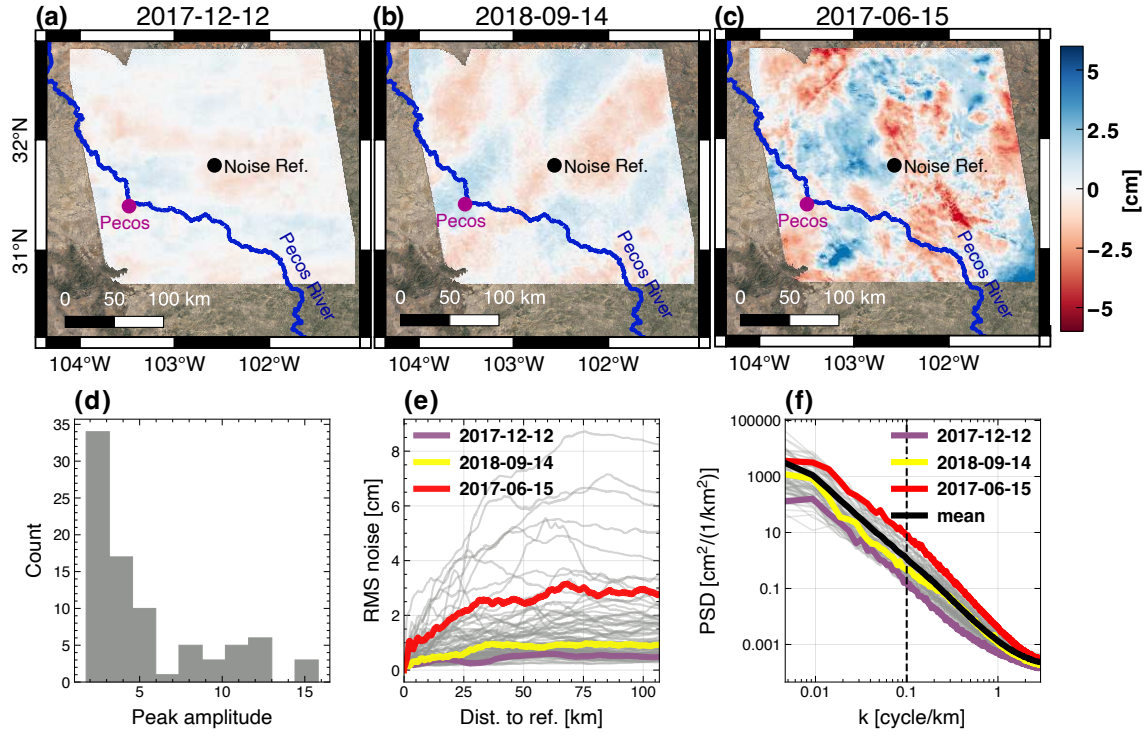
Figure 6.4: InSAR-estimated tropospheric turbulence noise maps for three Path 78 SAR acquisitions: (a) 2017-12-12 (up to 1.8 cm noise), (b) 2018-09-14 (up to 3.2 cm noise), and (c) 2017-06-15 (up to 12.6 cm noise). (d) The distribution of peak tropospheric noise magnitude (in centimeters), (e) the root mean squared value of tropospheric noise vs. distance from the center of the map, and (f) the estimated 1D PSDs for 84 Sentinel-1 Path 78 acquisitions used in this study. In panel (e) and (f), the color lines represent three SAR acquisitions (panel (a)-(c)) with different tropospheric noise levels. The black line in panel (f) represents the mean PSD of all 84 acquisitions.

km, and then the magnitude of the tropospheric noise does not change much as the distance increases. This means that the tropospheric noise is spatially correlated with a correlation length of ~ 50 km, and the tropospheric noise magnitude over the flat portion of the curve is a measure of the noise activity level.

The 1D PSDs for the 84 tropospheric turbulence noise maps give an alternative view of the distribution of noise power over different frequencies (Figure 6.4 (f). For most spatial frequencies, the PSDs decay following the -8/3 power law described in previous studies (Hanssen, 2001, Onn, 2006). This slope flattens at the low frequencies because we removed the quadratic phase in the noise solutions. The slope also flattens
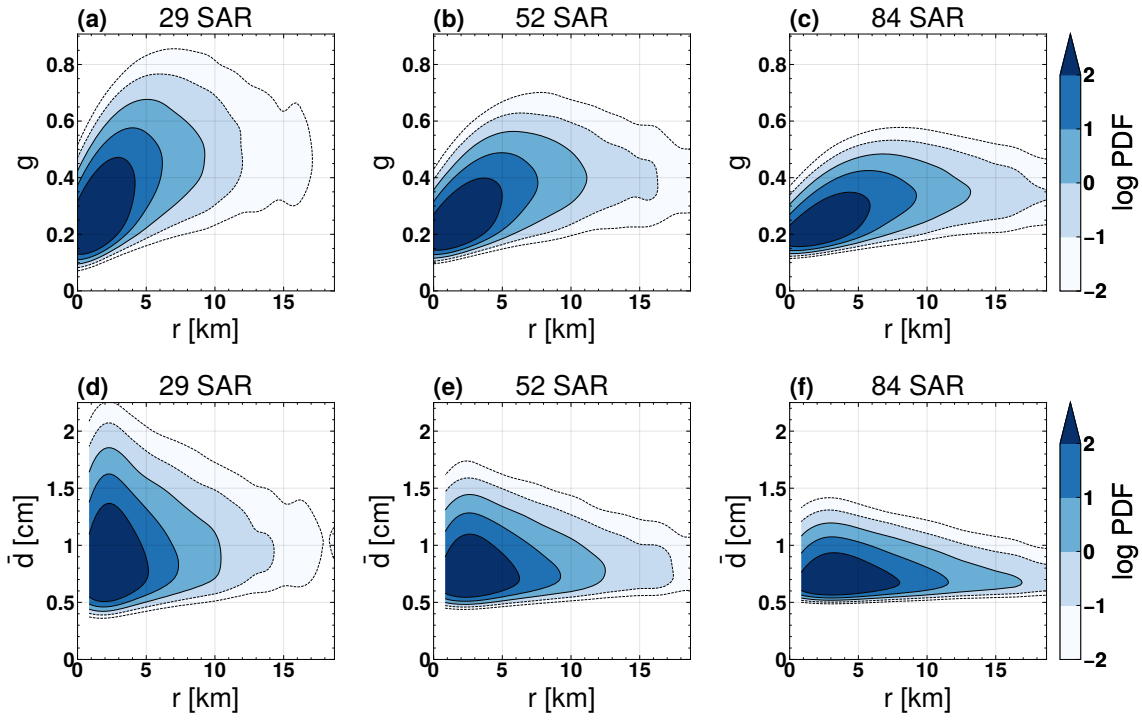
Figure 6.5: (a)-(c) Log Probability Density Function (PDF) of detecting tropospheric noise blobs as a function of feature size r and filter response magnitude $|g|$ for three cumulative LOS deformation maps: November 2014 - January 2017 (29 SAR scenes from Path 78), November 2014 - January 2018 (52 SAR Scenes from Path 78), and November 2014 - January 2019 (84 SAR Scenes from Path 78). (d)-(f) Log Probability Density Function (PDF) of detecting tropospheric noise blobs as a function of feature size r and deformation magnitude $|d|$ for the same three cumulative LOS deformation maps. The PDFs were generated from 2D histograms using a kernel density estimate (KDE) (Scott, 2015).

at high frequencies, where decorrelation noise introduces pixel-level variations in the noise map.

Using the mean 1D PSD shown in Figure 6.4 (f), we simulated instances of tropospheric turbulence, and computed the empirical PDFs of the noise attributes for each deformation map (Figure 6.5). Most of detected noise features have small radii ($r < 5$ km). For the 29 SAR acquisition case, the noise features are unlikely to be larger 2 cm in magnitude or have a filter response stronger than 0.7 (Figure 6.5 (a), (d)). For the 52 SAR acquisition case, the noise features are unlikely to be larger 1.5 cm in magnitude or have a filter response stronger than 0.6 (Figure 6.5 (b), (e)).

For the 84 SAR acquisition case, the noise features are unlikely to be larger 1.2 cm in magnitude or have a filter response stronger than 0.5 (Figure 6.5 (c), (f)). Note that the maximum and minimum sizes of detected features in Figure 6.5 (d)-(f) are determined by the choice of maximum and minimum kernel sizes σ_{max} and σ_{max} in our automatic detection algorithm. By imposing the prior knowledge that oil and gas-production related deformation bowls are unlikely to be larger than 30-40 km in the Permian Basin (Staniewicz et al., 2020), σ_{max} was set so that the maximum detected feature radius r was approximately 20 km. Thus, large-scale tropospheric noise features (radius > 20 km) were not recorded in the noise simulations.
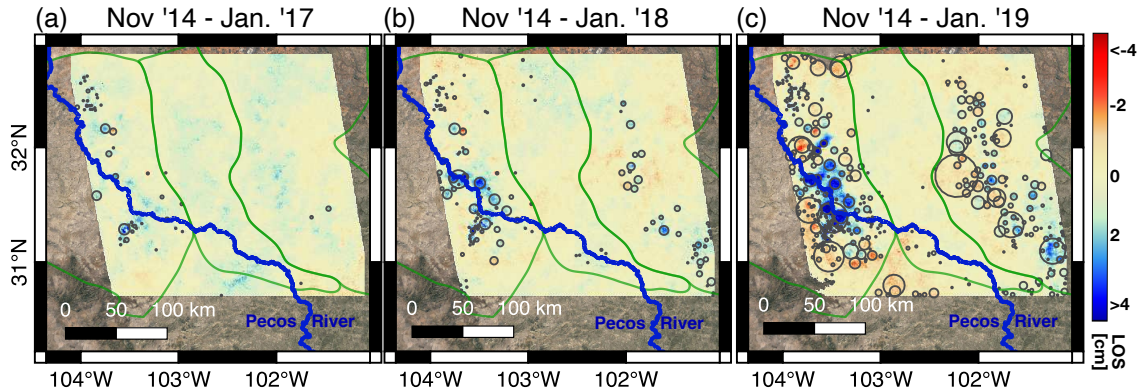
Figure 6.6: Detected deformation features (gray circles) from the three Path 78 cumulative LOS deformation maps. Features with more than 5% chance of being noise for their radius, according to either the filter magnitude or image magnitude PDFs (Figure 6.5), have been removed. Green lines correspond the boundaries of the Delaware Basin, Central Basin Platform, and Midland Basin from west to east.

Using the empirical PDFs of the noise attributes, we removed detections with more than 5% chance of being noise from three Path 78 cumulative deformation maps (Figure 6.6). We identified 57 deformation features in the Nov. 2014-Jan. 2017 cumulative deformation map, 147 features in the Nov. 2014-Jan. 2018 map, and 268 features in the Nov. 2014-Jan. 2019 map. The increasing number of detected deformation features is due to (1) the oil and gas production rate experienced a sharp rise over the study period (Staniewicz et al., 2020); and (2) a larger number of SAR acquisitions reduces the noise level in the InSAR cumulative deformation solutions.

The detected features are mainly clustered in regions within the Midland Basin and the Delaware Basin. Here oil production and wasterwater injection caused many centimeter-level subsidence and uplift features. In the Southern Delaware Basin,

the observed linear deformation features parallel the inferred favorable fault plane orientation proposed by (Lund Snee and Zoback, 2018), and they align with a cluster of recent shallow earthquakes cataloged by TexNet (Savvaidis et al., 2019). Very few deformation features were detected in the Central Basin Platform, where oil and gas are mostly produced from conventional reservoirs and the subsurface pressure was well maintained.

For the West Texas case, the residual deformation term $\frac{1}{N-1}\sum \Delta d_{n,k}$ in Equation (6.5) does not significantly influence our noise simulations. To demonstrate this, Figure 6.7 (a) shows the tropospheric noise estimates on a quiet atmospheric date (2018-09-04) and Figure 6.7 (b) shows the cumulative LOS deformation solution between Nov. 2014 and Jan. 2019. The 1D PSDs for the noise-only map and the noise plus deformation map are very similar (Figure 6.7 (c)). This is because the total integrated power of the noise map is five times larger than the total power of the deformation map. Since the residual deformation contribution in Equation (6.5), $\frac{1}{N-1}\sum \Delta d_{n,k}$, is much less than the total cumulative deformation over the entire study period, we conclude that this term in the tropospheric noise estimates has negligible effects on the detection confidences derived from the noise simulations.
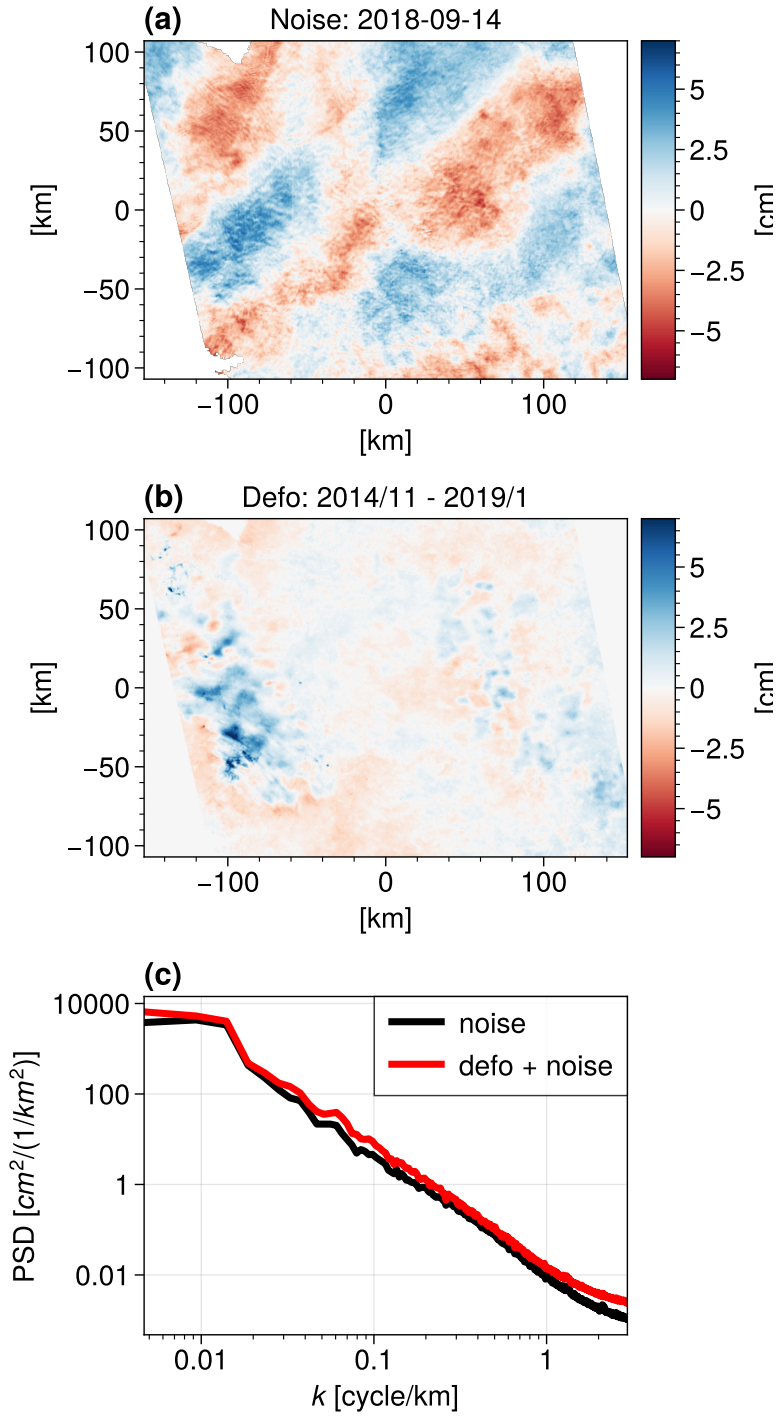
Figure 6.7: (a) InSAR-estimated tropospheric noise map for the Path 78 SAR acquisition 2018-09-14. (b) Cumulative LOS deformation from Nov. 2014 to Jan. 2019 as inferred from Sentinel-1 Path 78 InSAR data. (c) 1D PSDs derived from the tropospheric noise map (black) and the tropospheric noise plus deformation map (red).

6.3.2 Path 85 Detections
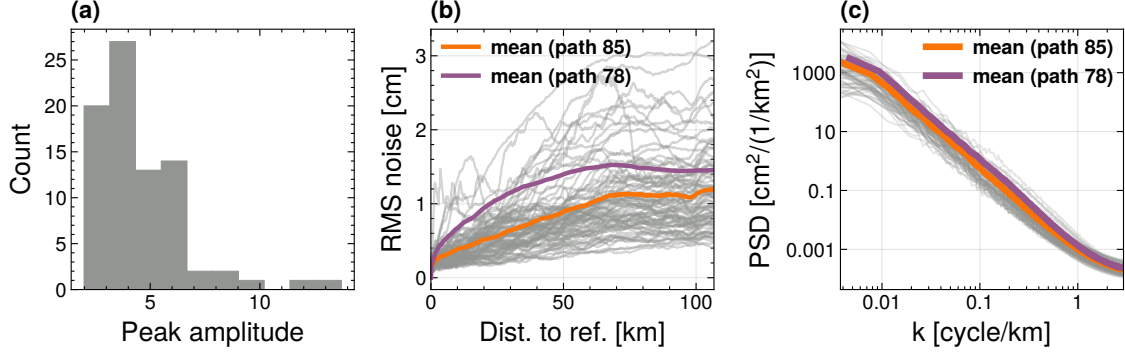
Figure 6.8: (a) The distribution of peak tropospheric noise magnitude (in centimeters), (b) the root mean squared value of tropospheric noise vs. distance from the center of the map, and (c) the estimated 1D PSDs for 81 Sentinel-1 Path 85 acquisitions used in this study. In panel (b) and (c), the color lines represent the average estimates for Path 85 (orange) and Path 78 (purple).

Table 6.1: Tropospheric noise characteristics for Sentinel-1 Path 85 and Path 78 data over West Texas

	Path 78	Path 85
Average Variance $[cm^2]$	1.38	0.78
Variance of the Noisiest Date $[cm^2]$	10.68	3.74
Average Peak Amplitude [cm]	5.36	4.58
Peak Amplitude of the Noisiest Date [cm]	15.81	13.72

Similar to the ascending Path 78 results, approximately 50% of descending Path 85 scenes were acquired in quiet atmospheric conditions with a maximum noise level under 4 cm (Figure 6.8 (a)). However, only 2 out of 81 descending scenes were acquired in strong turbulent noise conditions (a maximum noise level over 10 cm), while 14 out of the 84 ascending scenes were acquired in such conditions. We also found that the average tropospheric noise level is lower for Path 85 than Path 78 (Figure 6.8 (b)-(c)). For example, the mean absolute tropospheric noise is 50% larger for Path 78 than Path 85 at 50 km, and the mean noise PSD is more than 2 times larger for Path 78 than Path 85 at a spatial frequency of 0.1 cycles/km. We summarized the noise statistics of Path 78 and Path 85 acquisitions in Table 6.1. The differences are
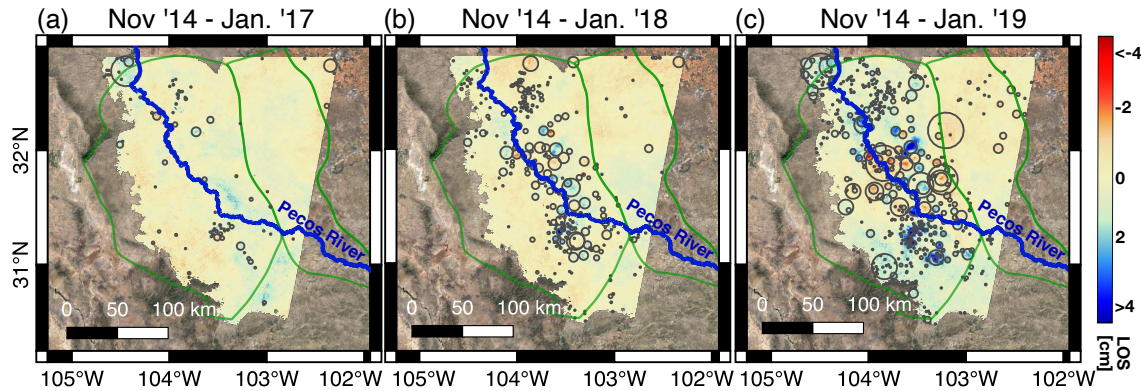
Figure 6.9: Detected deformation features (gray circles) from the three Path 85 cumulative LOS deformation maps. Features with more than 5% chance of being noise for their radius, according to either the filter magnitude or image magnitude PDFs (Figure 6.5), have been removed. Green lines illustrate the boundaries of the Delaware Basin and Central Basin Platform, from west to east.

due to the fact that Sentinel-1 satellites acquire Path 78 data over West Texas at 7:50 p.m. local time, and Path 85 data at 6:55 a.m local time. The expected tropospheric noise signatures are typically more substantial in late afternoon than early morning.

Our algorithm identified similar numbers of blob features from the ascending and descending cumulative LOS deformation maps that span the same period of interest. Because the tropospheric noise level is generally lower in Path 85 data, fewer Path 85 detections need to be removed for having > 5% chance of being tropospheric noise. As a result, we detected more deformation features from the Path 85 dataset than the Path 78 dataset. It is also worth noting that the number of detected deformations in both paths increases substantially over the study period. This is consistent with the overall rise in oil production within the Permian Basin during this time period (Figure 6.10) .
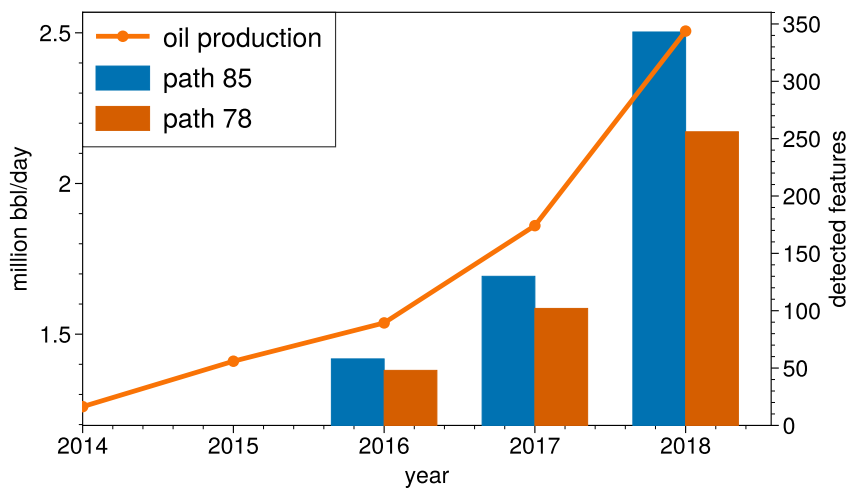
Figure 6.10: The number of deformation features ($< 5\%$ chance of being tropospheric noise) detected from three Path 78 cumulative LOS deformation maps (Figure 6.6) and three Path 85 cumulative LOS deformation maps (Figure 6.9). Only detections from the overlapping region of the two paths are counted. The Permian Basin average daily oil production from 2014 and 2018 is shown as the orange line.

Chapter 7

Summary and Conclusions

In this dissertation, we demonstrated the ability to derive accurate surface deformation maps over broad areas from InSAR measurements corrupted by severe tropospheric noise. We further demonstrated techniques for estimating uncertainty of automatically detected deformation features. Specifically, we have made the following contributions:

1. We developed Python-based InSAR time series analysis software that processes geocoded SAR images acquired from multiple imaging geometries and reconstructs surface deformation in eastward and vertical directions.

2. We performed a rigorous analysis of all noise sources in the Permian Basin Sentinel-1 InSAR data. We identified that the dominant noise term is the tropospheric turbulence noise with up to 15 cm non-Gaussian outliers. We developed methods for characterizing tropospheric noise and its power spectral density directly from InSAR data, as well as methods for mitigating the impact of the troposphere noise outliers.

3. We designed scalable, robust time series algorithms for reconstructing the temporal evolution of surface deformation over very wide regions. Based on independent validation from GPS permanent stations, we achieved millimeter-level accuracy in the cumulative surface deformation solutions.

4. We developed a computer vision algorithm for automatically detecting surface deformation signals of unknown sizes in basin-scale InSAR maps. The detection algorithm produces uncertainty measures for each detected feature based on a realistic tropospheric turbulence noise model.

5. InSAR reveals numerous subsidence and uplift features near active production and disposal wells, as well as linear deformation patterns associated with fault activities near clusters of seismic activity. Our InSAR deformation maps are now openly available through the Center for Integrated Seismicity Research (CISR) for the broader scientific community and stakeholders.

With multiple government and commercial SAR missions scheduled in upcoming years, there will be opportunities for creating continental and global deformation products from InSAR data. For example, the Observational Products for End-Users from Remote Sensing Analysis (OPERA) project at NASA JPL has been tasked to produce a North America land-surface displacement product from Sentinel-1 and NISAR data (Bekaert et al., 2021). Since the processing and analysis techniques required for such a product must be scalable and robust, the techniques developed here can contribute to these efforts.

Future work beyond extending the results presented here may include:

- Combining subsurface pore pressure models using the wastewater disposal history (e.g. Ge et al. (2022)) with the recent changes to surface deformation to determine subsurface flow barriers and locations of elevated pressure. This effort could leverage the recent detailed compilation of known faults in the Delaware Basin (Horne et al., 2021).

- Simulating both seasonal and stratified tropospheric noise to more accurately estimate uncertainty. The noise simulations presented in Chapter 6 used tropospheric turbulence, which was the dominant error source for West Texas. The seasonal variations of tropospheric noise may be important to accurately infer uncertainty for other study areas.

- Incorporating additional error sources into the noise simulations, including unwrapping errors (Yunjun et al., 2019), closure phase bias (Zheng et al., 2022), and speckle-induced uncertainty (Zwieback and Meyer, 2022).

- Combining auxiliary data sources with the automatically detected deformation features of Chapter 6 to classify/categorize possible causes of deformation.

- Increasing accessibility of InSAR-derived products by leveraging new, cloud-friendly data formats (e.g. Kellndorfer et al. (2022)).

Appendix A

Geomechanical Modeling of Pecos

Here we present details of the geomechanical modeling performed by Hunjoo Lee (Staniewicz et al. (2020)) using the surface deformation data from Chapter 4.

A.1 Dislocation (Fault Slip) Model

Okada (1992) derived the analytical surface displacement field due to a finite rectangular fault slip in an elastic half-space. The Okada solutions provide three cases of displacement on a fault: strike-slip, dip-slip, tensile opening. In this study, we focused on the dip-slip case, because the Pecos area is in a normal faulting regime (Lund Snee and Zoback, 2018). The assumption of predominant dip-slip along normal faults is also supported by fault plane solutions (TexNet Earthquake Catalog).

Considering the case of dip slip on a finite rectangular fault (Figure A.1), the vertical surface displacement $u_z(x, y, 0)$ can be expressed as:

$$u_z(x, y, 0) = \frac{U_2}{2\pi}[u_2^B \sin \delta + u_3^B \cos \delta] \tag{A.1}$$

where U_2 is the magnitude of dip slip. The rest of terms on the right are determined by fault geometry parameters: the fault dip angle (δ), the depth to the top of the fault (Z), the fault width along the dip direction (W), and the fault length along the strike direction (L).

We located four faults based on InSAR observations, and assumed a uniform slip on each fault. We estimated the best-fit fault parameters for each fault independently by minimizing the objective function (Du et al., 1992):

$$\arg \min_{U_{2,i}} \|\mathbf{G_i} U_{2,i} - \mathbf{d_i}\|_2^2 \tag{A.2}$$

where $\mathbf{G_i}$ is the discrete Green's function that maps a dip slip, $U_{2,i}$, on the ith rectangular fault to the observed vertical deformation at specific surface locations. $\mathbf{G_i}$ is a function of fault geometry parameters as shown in Equation (A.1). $\mathbf{d_i}$ is a vector of vertical deformation observations associated with the ith fault from InSAR data.

Table A.1: Best-fit fault parameters as derived from the dislocation model

	Fault #1	Fault #2	Fault #3	Fault #4
1-Longitude (°)	-103.563	-103.589	-103.585	-103.529
1-Latitude (°)	31.367	31.413	31.463	31.470
2-Longitude (°)	-103.503	-103.505	-103.440	-103.468
2-Latitude (°)	31.337	31.355	31.374	31.432
Dip Angle (°)	60	60	50	57.5
Depth (km)	0.91	0.91	1.07	1.52
Width (km)	0.61	0.30	1.07	0.61
Slip (cm)	9.1	15.2	9.1	15.2

Through a grid-search, we solved for the fault dip angle, the depth to the top of the fault, the width along the dip direction, and the magnitude of dip slip on each fault to minimize the sum of squared residuals normalized by the data error of 1 cm (Normalized Sum of Squared Residuals; NSSR). The fault length in the strike direction is set to be sufficiently long to satisfy the plane strain condition. As an example, Figure A.2 shows how the data misfit varies with fault parameters for fault #3. The maximum R-squared (R^2) values for the best-fit fault parameters are in the range of 0.95 and generally agree with the fault parameters that satisfy the minimum NSSR.

The best-fit fault parameters of the four faults are listed in Table A.1, which produce 3D surface deformation patterns as shown in Figure A.3. To illustrate how surface deformation observations are related to the model parameters, Figure A.4 shows the estimated surface subsidence associated with the fault #3 long the B-B' transect with various fault properties. The ratio of the uplift volume to the subsidence volume is a function of the seismic potency and the fault dip angle (Segall and Heimisson, 2019). Based on the results in Figure A.4 (a), the fault dip angle dominantly controls the uplift volume relative to the subsidence volume. The slope from the uplift on the footwall to the subsidence on the hanging wall becomes steeper as the fault becomes shallower (Figure A.4 (b)). The fault width, as measured along the the dip direction, mostly contributes to the width of the subsidence bowl (Figure A.4 (c)). The dip-slip magnitude only has impact on the amplitude of the curve without any influence on the shape of the surface deformation (Figure A.4 (d)).
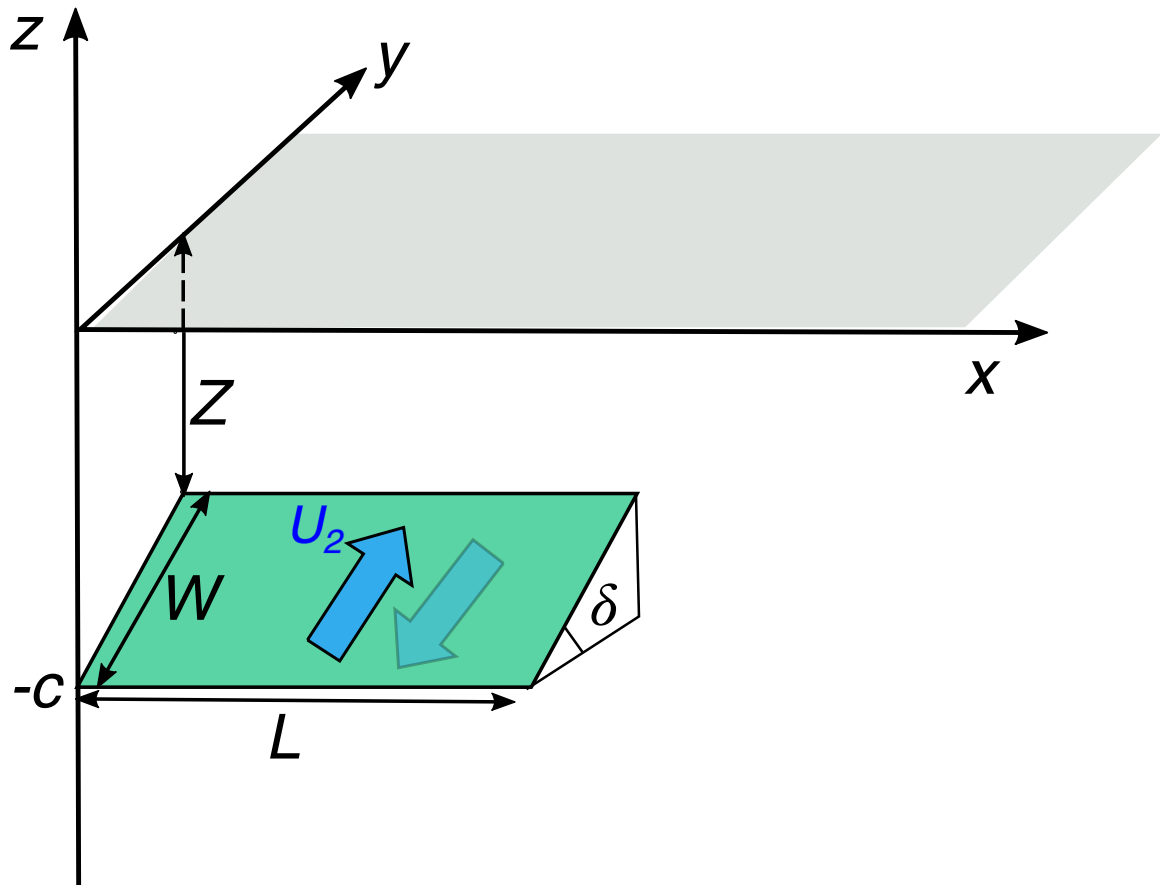
Figure A.1: A finite rectangular fault model from Okada (1992). Here U_2 is the magnitude of dip slip (positive in reverse fault direction), δ is the dip angle, Z is the depth to the top of the fault, c is the depth to the bottom of the fault, L is the length along the strike direction, and W is the width along the dip direction.
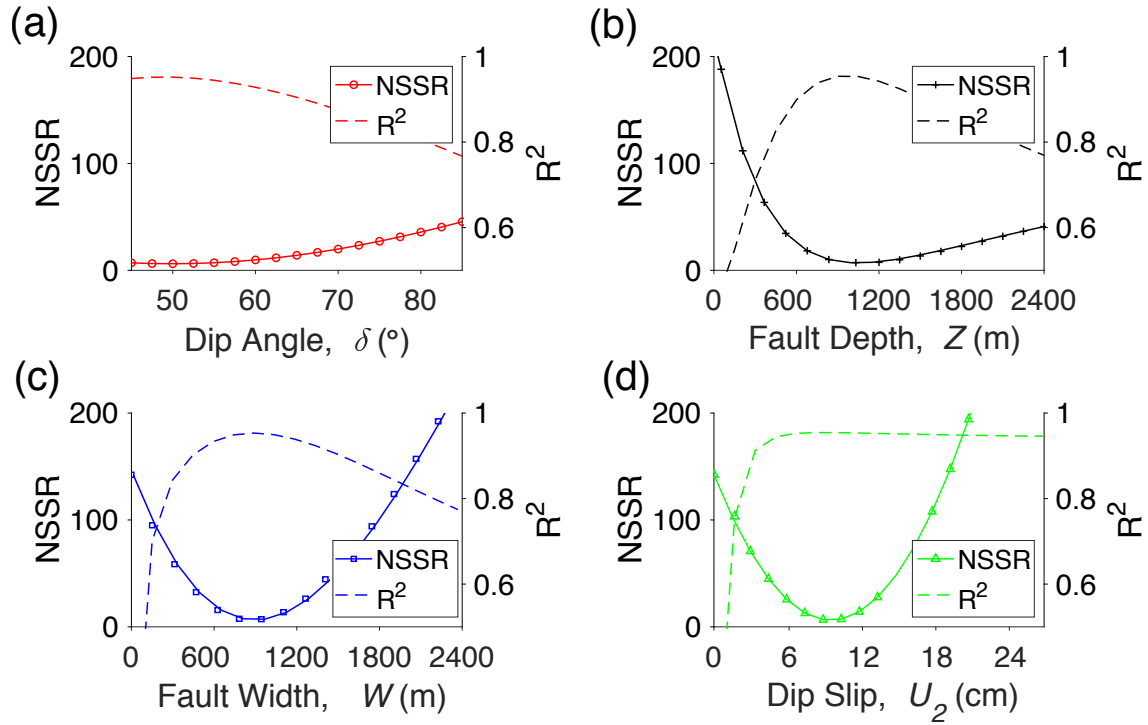
Figure A.2: The Normalized Sum of Squared Residuals (NSSR) and R-squared (R^2) of fault #3 relative to (a) fault dip angle (δ), (b) fault depth from the surface to the top of the fault (Z), (c) fault width along the dip direction (W), and (d) net dip slip magnitude (U_2).
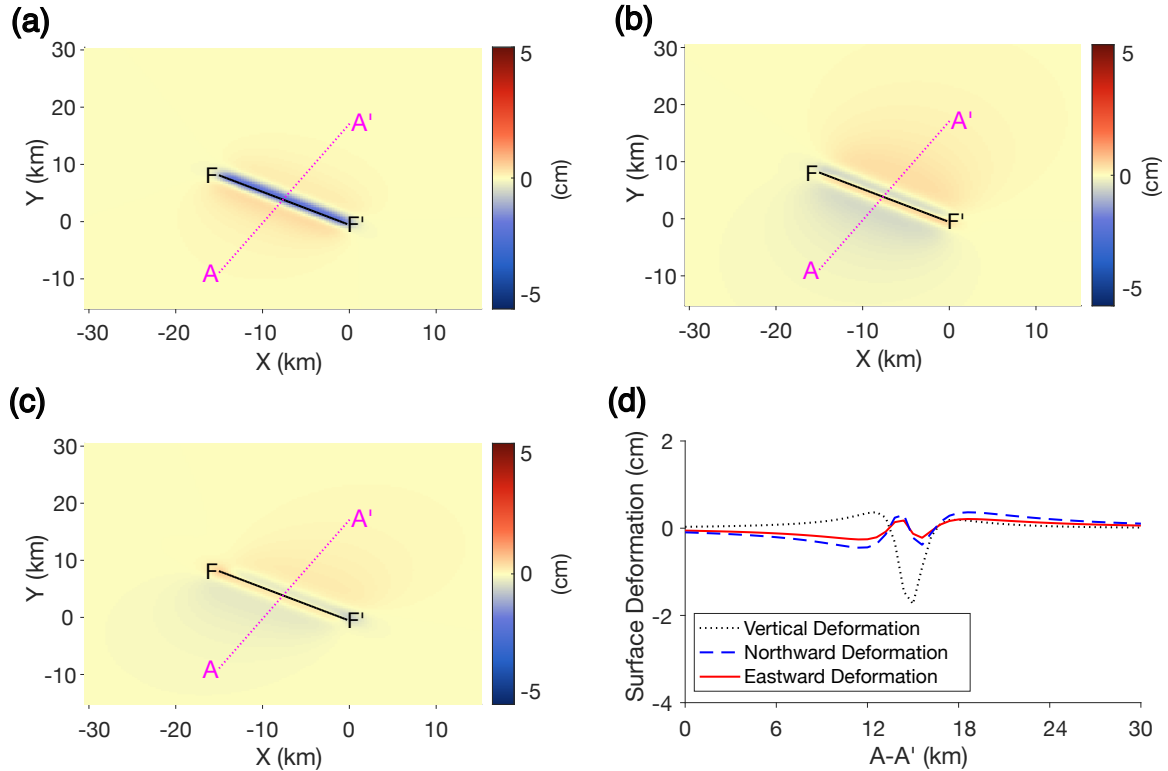
Figure A.3: The predicted surface deformation from the Okada fault model with best-fit parameters in the (a) vertical direction (positive means uplift), (b) northward direction (positive means north, negative means south), and (c) eastward direction (positive means east, negative means west). (d) Comparison of the 3D deformation profiles along A-A$'$ transect that is perpendicular to fault plane.
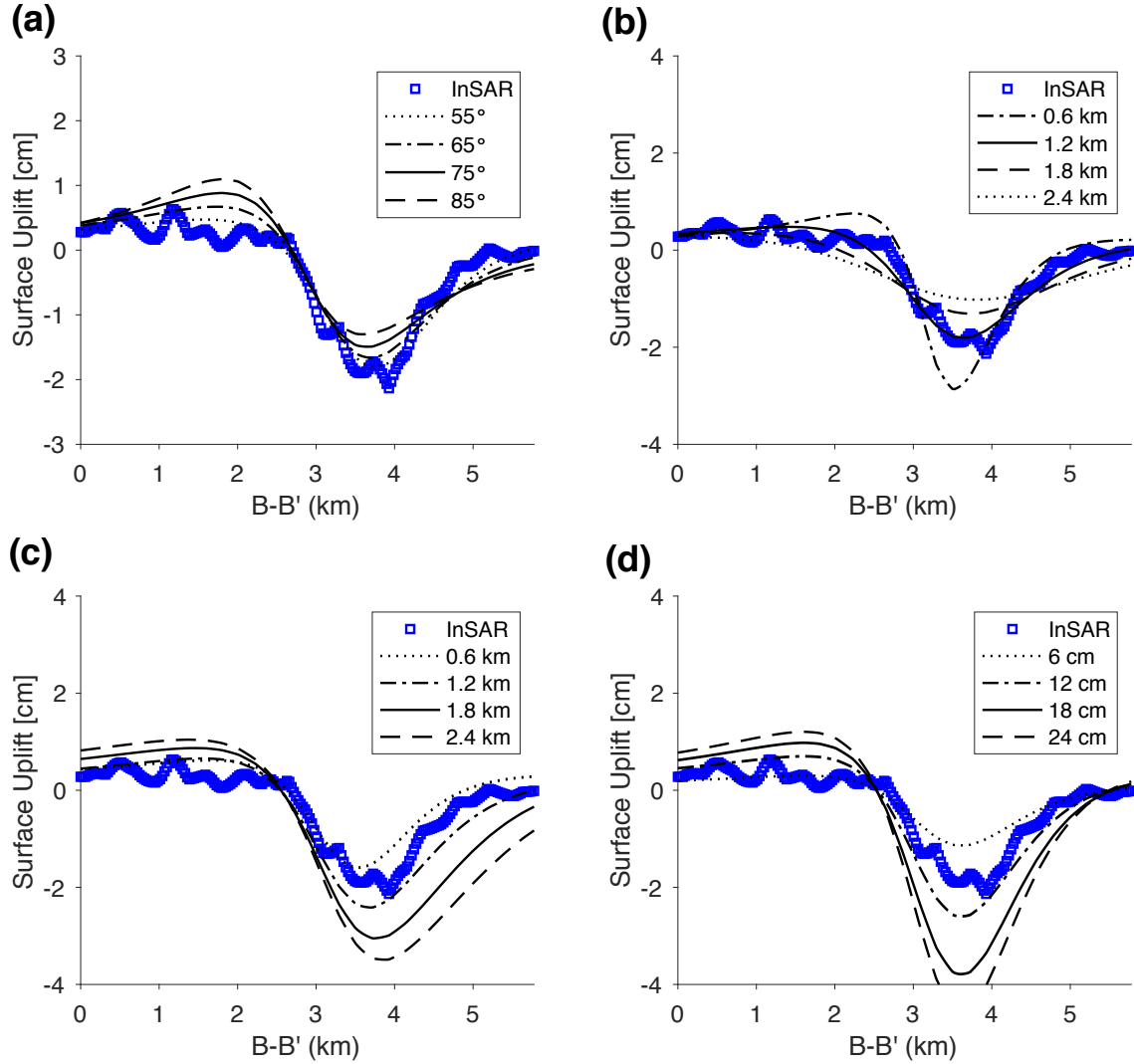
Figure A.4: Estimated surface subsidence along the B-B' transect associated with fault #3 with various fault properties: (a) fault dip angle (δ) of 55°, 65°, 75°, 85°, (b) fault depth from the surface to the top of the fault (Z) of 0.6 km, 1.2 km, 1.8 km, 2.4 km, (c) fault width along the dip direction, W) of 0.6 km, 1.2 km, 1.8 km, 2.4 km, and (d) net dip slip magnitude (U_2) of 6 cm, 12 cm, 18 cm, 24 cm.

A.2 Cylindrical Reservoir Compaction/Subsidence Model

Geertsma et al. (1973) derived the surface displacement field due to a uniform pressure drop of a cylindrical reservoir at a depth D (Figure A.5). Under the assumption that the reservoir radius R is larger than the reservoir height H, the cylindrical reservoir deforms primarily in the vertical direction. The magnitude of the reservoir compaction ΔH due to a pressure drop ΔP can be written as:

$$\Delta H = Hc_m \Delta P \tag{A.3}$$

Here the uniaxial compaction coefficient c_m can be expressed as

$$c_m = \alpha_p \frac{1+\nu}{1-\nu} \frac{c_b}{3} \tag{A.4}$$

where α_p is Biot's coefficient, c_b is the bulk compressibility, and ν is the Poisson's ratio. Surface vertical deformation u_z due to the reservoir compaction ΔH can be expressed as:

$$u_z(r,0) = 2(1-\nu)\Delta H A(\rho, \eta) \tag{A.5}$$

where $A(\rho, \eta) = R \int_0^\infty e^{-D\alpha} J_1(\alpha R) J_0(\alpha r)\, d\alpha$, $\rho = r/R$, and $\eta = D/R$. The maximum surface deformation at $r = 0$ can be written as:

$$u_z{}^{max} = 2(1-\nu)\Delta H(1 - \frac{\eta}{\sqrt{1+\eta^2}}) \tag{A.6}$$

The best-fit compaction in the cylindrical reservoirs were determined by minimizing the objective function (Du and Olson, 2001):

$$\arg\min_{\mathbf{\Delta H}} = \|\mathbf{G_R \Delta H} - \mathbf{d_r}\|^2 + \beta^2 \|\mathbf{H_L \Delta H} - \mathbf{d_0}\|^2 \tag{A.7}$$

where $\mathbf{G_R}$ is the discrete Green's function that maps the compaction of cylindrical reservoirs $\mathbf{\Delta H}$ in the subsurface to the observed vertical deformation at specific surface locations. $\mathbf{G_R}$ is a function of reservoir geometry parameters as shown in Equation (A.5). $\mathbf{d_r}$ is a vector of vertical deformation observations associated with the reservoir compaction. In this study, $\mathbf{d_r}$ is the difference between the InSAR-

observed total vertical deformation and modeled vertical fault slip deformation, β^2 is the penalty factor that weights the smoothness constraint, and $\mathbf{H_L}$ is the finite difference approximation of the Laplacian operator. The reservoir compaction is constrained to be negative, and $\mathbf{d_0}$ is set to be zero.

Based on the production well data near Pecos, we discretized two layers of reservoirs in the subsurface: Delaware Mountain Group (DMG) at depth 1.52 km and Wolfcamp at depth 3.05 km (Figure A.6). The shallow groundwater level reservoirs were not included in the reservoir model, because the water levels in the groundwater aquifers in the Pecos area were stable over the time period of interest (Deng et al., 2020). The producing wells in the DMG were predominantly located to the east of Pecos, and we set 25 cylindrical reservoirs with the radius of 0.83 km. In the Wolfcamp formation, the wells were producing over the entire region. We discretized the layer covering the entire area with 100 cylindrical reservoirs with the radius of 0.83 km.

We utilized the pattern search optimization tool in MATLAB to minimize the objective function (Equation (A.7)). As the penalty factor β^2 decreases, the NSSR decreases, R^2 increases, and the modeled surface deformation better matches the InSAR data (Figure A.7). Once the penalty factor (β^2) is smaller than 0.01, the NSSR and R^2 no longer change substantially. The best-fit reservoir compaction results (β^2 equals 0.01) for the two producing layers are shown in Figure A.6. While DMG reservoirs show some compaction (0 - 8 cm), the dominant compaction is in the Wolfcamp layer (0 - 27 cm). The production volume in DMG is as significant as in Wolfcamp. However, the dominant injection volume into DMG could maintain the reservoir pressure and minimize reservoir compaction. For certain regions in the Wolfcamp layer, the reservoir compaction appears to be discontinuous given the low β^2 value. We note that it is reasonable to observe localized compaction for tight shale formations, because the low formation permeability can cause heterogeneous pressure distribution during the depletion.

If appropriate mechanical properties of the formation are available, the distribution of reservoir pressure change and depleted zone can be evaluated by the reservoir compaction magnitudes based on Equation (A.3). For example, if we assume Young's modulus of 25 GPa, Poisson's ratio of 0.25, and Biot's coefficient of 0.67 based on published rock properties (Shukla et al., 2013, Xu and Zoback, 2015), the localized
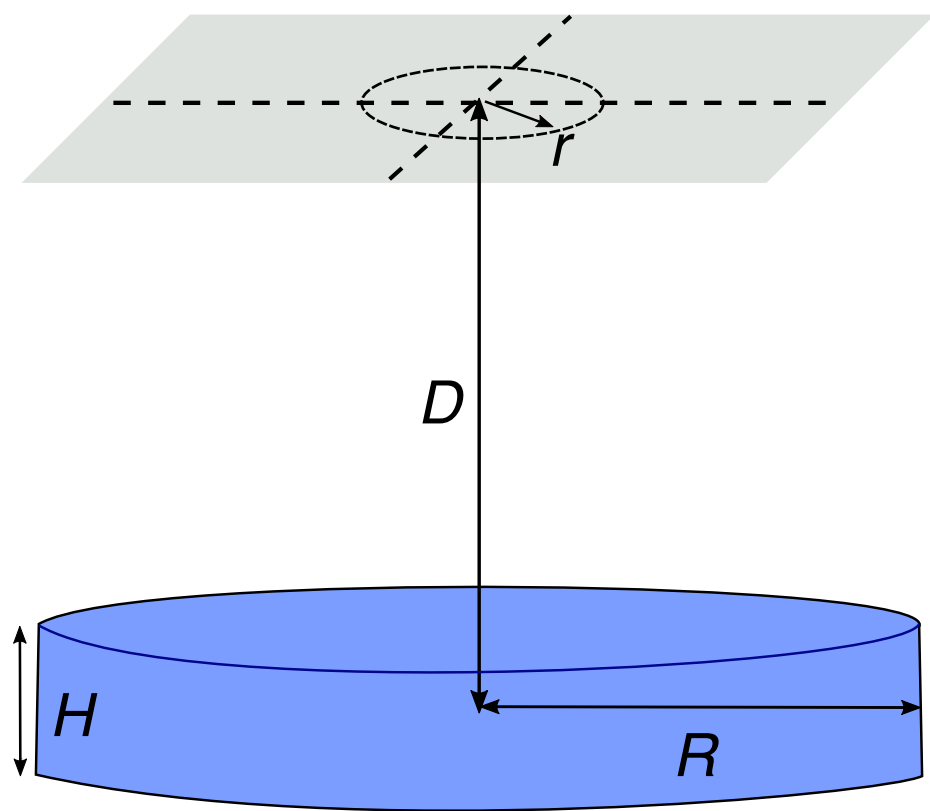
Figure A.5:   Geometry of reservoir model in Geertsma et al. (1973), where H is the reservoir height, D is the reservoir depth, and R is the reservoir radius.
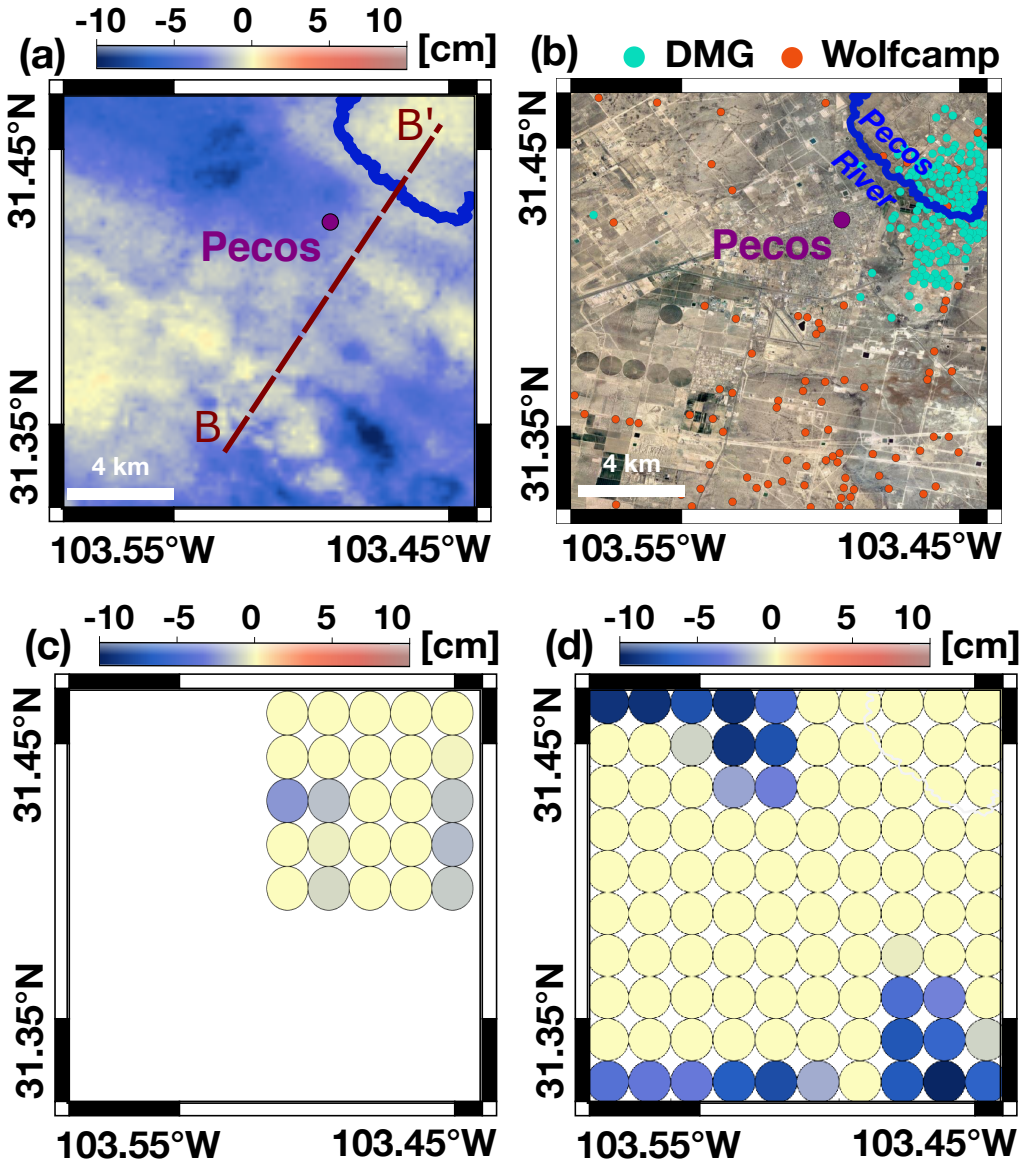
Figure A.6: (a) Input for reservoir model: vertical surface deformation difference between InSAR and fault model (vertical surface deformation not explained by the fault model). (b) Producing well locations in near Pecos in the Delaware Mountain Group (DMG, cyan) and Wolfcamp (orange). Reservoir compaction values in (c) DMG reservoirs at depth 1.52km, and (d) Wolfcamp reservoirs at depth 3.05km.
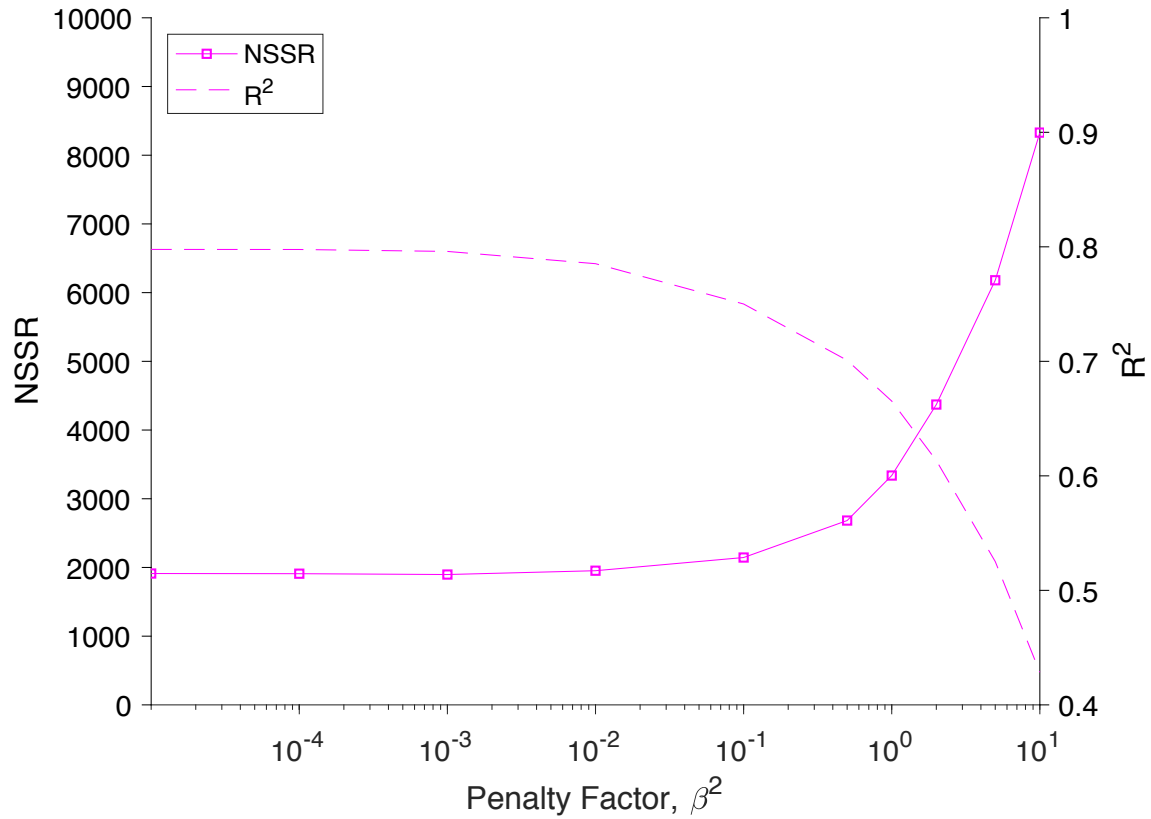
Figure A.7: The Normalized Sum of Squared Residuals (NSSR) and R-squared (R^2) with varying penalty factor (β^2) for the discretized reservoir compaction model

maximum pressure drop is approximately 21 MPa. This is within a reasonable range given operational history in the area.

Bibliography

Agram, P., Jolivet, R., Riel, B., Lin, Y., Simons, M., Hetland, E., Doin, M.-P., and Lasserre, C. (2013). New radar interferometric time series analysis toolbox released. *Eos, Transactions American Geophysical Union*, 94(7):69–70.

Agram, P. S. (2010). *Persistent Scatterer Interferometry in Natural Terrain*. PhD thesis, Stanford University.

Anantrasirichai, N., Biggs, J., Albino, F., and Bull, D. (2019a). The application of convolutional neural networks to detect slow, sustained deformation in InSAR time series. *Geophysical Research Letters*, 46(21):11850–11858.

Anantrasirichai, N., Biggs, J., Albino, F., and Bull, D. (2019b). A deep learning approach to detecting volcano deformation from satellite imagery using synthetic datasets. *Remote Sensing of Environment*, 230:111179.

Anantrasirichai, N., Biggs, J., Albino, F., Hill, P., and Bull, D. (2018). Application of machine learning to classification of volcanic deformation in routinely generated InSAR data. *Journal of Geophysical Research: Solid Earth*.

Ansari, H. (2018). *Efficient High-Precision Time Series Analysis for Synthetic Aperture Radar Interferometry*. PhD thesis, Technical University of Munich.

Atkinson, G. M., Eaton, D. W., Ghofrani, H., Walker, D., Cheadle, B., Schultz, R., Shcherbakov, R., Tiampo, K., Gu, J., Harrington, R. M., Liu, Y., van der Baan, M., and Kao, H. (2016). Hydraulic fracturing and seismicity in the western canada sedimentary basin. *Seismological Research Letters*, 87(3):631–647.

Bamler, R. and Hartl, P. (1998). Synthetic aperture radar interferometry. *Inverse Problems*, 14(4):R1–R54.

Barnhart, W. D. and Lohman, R. B. (2013). Characterizing and estimating noise in InSAR and InSAR time series with MODIS. *Geochem. Geophys. Geosyst.*, 14(10):4121–4132.

Bekaert, D., Walters, R., Wright, T., Hooper, A., and Parker, D. (2015a). Statistical comparison of insar tropospheric correction techniques. *Remote Sensing of Environment*, 170:40–47.

Bekaert, D. P., Fattahi, H., Jones, J. W., Hansen, M., Kwoun, O.-I., Lewis, S. J., Meyer, F. J., Osmanoglu, B., Marshak, C., Hamlington, B., et al. (2021). Introducing the OPERA project for systematic surface water, surface deformation, and surface disturbance data products from satellite observations. In *AGU Fall Meeting 2021*. AGU.

Bekaert, D. P., Handwerger, A. L., Agram, P., and Kirschbaum, D. B. (2020). InSAR-based detection method for mapping and monitoring slow-moving landslides in remote regions with steep and mountainous terrain: An application to nepal. *Remote Sensing of Environment*, 249:111983.

Bekaert, D. P. S., Hooper, A., and Wright, T. J. (2015b). A spatially variable power law tropospheric correction technique for InSAR data. *Journal of Geophysical Research: Solid Earth*, 120(2):1345–1356.

Berardino, P., Fornaro, G., Lanari, R., and Sansosti, E. (2002). A new algorithm for surface deformation monitoring based on small baseline differential SAR interferograms. *Geoscience and Remote Sensing, IEEE Transactions on*, 40(11):2375–2383.

Blewitt, G., Hammond, W., and Kreemer, C. (2018). Harnessing the gps data explosion for interdisciplinary science. *EOS*, 99.

Born, G. H., Dunne, J. A., and Lame, D. B. (1979). Seasat mission overview. *Science*, 204(4400):1405–1406.

Burbey, T. J. (2008). The influence of geologic structures on deformation due to ground water withdrawal. *Groundwater*, 46(2):202–211.

Bürgmann, R., Rosen, P. A., and Fielding, E. J. (2000). Synthetic aperture radar interferometry to measure earth's surface topography and its deformation. *Annual review of earth and planetary sciences*, 28(1):169–209.

Cao, Y., Jónsson, S., and Li, Z. (2021). Advanced InSAR tropospheric corrections from global atmospheric models that incorporate spatial stochastic properties of the troposphere. *Journal of Geophysical Research: Solid Earth*, 126(5).

Chaussard, E., Bürgmann, R., Shirzaei, M., Fielding, E. J., and Baker, B. (2014). Predictability of hydraulic head changes and characterization of aquifer-system and fault properties from InSAR-derived ground deformation. *Journal of Geophysical Research: Solid Earth*, 119(8):6572–6590.

Chen, C. W. and Zebker, H. A. (2001). Two-dimensional phase unwrapping with use of statistical models for cost functions in nonlinear optimization. *Journal of the Optical Society of America A*, 18(2):338–351.

Chen, J., Knight, R., Zebker, H. A., and Schreüder, W. A. (2016). Confined aquifer head measurements and storage properties in the San Luis Valley, Colorado, from spaceborne InSAR observations. *Water Resources Research*, 52(5):3623–3636.

Cleveland, W. S. (1979). Robust locally weighted regression and smoothing scatterplots. *Journal of the American Statistical Association*, 74(368):829–836.

Council, N. R. (2013). *Induced Seismicity Potential in Energy Technologies*. National Academies Press.

Cumming, I. and Bennett, J. (1979). Digital processing of seasat SAR data. In *ICASSP '79. IEEE International Conference on Acoustics, Speech, and Signal Processing*. Institute of Electrical and Electronics Engineers.

Cumming, I. G. and Wong, F. H. (2004). *Digital Processing of Synthetic Aperture Radar Data: Algorithms and Implementation*. Artech House Inc.

Dahm, T., Becker, D., Bischoff, M., Cesca, S., Dost, B., Fritschen, R., Hainzl, S., Klose, C. D., Kühn, D., Lasocki, S., Meier, T., Ohrnberger, M., Rivalta, E., Wegler, U., and Husen, S. (2012). Recommendation for the discrimination of human-related and natural seismicity. *Journal of Seismology*, 17(1):197–202.

Deichmann, N. and Giardini, D. (2009). Earthquakes induced by the stimulation of an enhanced geothermal system below basel (switzerland). *Seismological Research Letters*, 80(5):784–798.

Deng, F., Dixon, T. H., and Xie, S. (2020). Surface deformation and induced seismicity due to fluid injection and oil and gas extraction in western texas. *Journal of Geophysical Research: Solid Earth*, page e2019JB018962.

Ding, X.-l., Li, Z.-w., Zhu, J.-j., Feng, G.-c., and Long, J.-p. (2008). Atmospheric effects on InSAR measurements and their mitigation. *Sensors*, 8(9):5426–5448.

Doin, M., Lasserre, C., Peltzer, G., Cavalie, O., and Doubre, C. (2009). Corrections of stratified tropospheric delays in SAR interferometry: validation with global atmospheric models. *Journal of Applied Geophysics*, 69(1):35 – 50.

Du, J. and Olson, J. E. (2001). A poroelastic reservoir model for predicting subsidence and mapping subsurface pressure fronts. *Journal of Petroleum Science and Engineering*, 30(3):181 – 197.

Du, Y., Aydin, A., and Segall, P. (1992). Comparison of various inversion techniques as applied to the determination of a geophysical deformation model for the 1983 Borah Peak earthquake. *Bulletin of the Seismological Society of America*, 82(4):1840–1866.

Duersch, M. I. (2013). *Backprojection for synthetic aperture radar*. PhD thesis, Brigham Young University.

Ebmeier, S. K. (2016). Application of independent component analysis to multitemporal InSAR data with volcanic case studies. *Journal of Geophysical Research: Solid Earth*, 121(12):8970–8986.

Efron, B. (1979). Bootstrap methods: Another look at the jackknife. *The Annals of Statistics*, 7(1).

Efron, B. and Hastie, T. (2019). *Computer Age Statistical Inference: Algorithms, Evidence, and Data Science*. Cambridge University Press.

Efron, B. and Tibshirani, R. J. (1994). *An introduction to the bootstrap*. CRC press.

Elliott, J. R., Biggs, J., Parsons, B., and Wright, T. J. (2008). InSAR slip rate determination on the altyn tagh fault, northern tibet, in the presence of topographically correlated atmospheric delays. *Geophysical Research Letters*, 35(12):n/a–n/a.

Elliott, J. R., Walters, R. J., and Wright, T. J. (2016). The role of space-based observation in understanding and responding to active tectonics and earthquakes. *Nature Communications*, 7(1):13844.

Ellsworth, W. L. (2013). Injection-induced earthquakes. *Science*, 341(6142):1225942.

Emardson, T. R., Simons, M., and Webb, F. H. (2003). Neutral atmospheric delay in Interferometic Synthetic Aperture Radar applications: Statistical description and mitigation. *Journal of Geophysical Research: Solid Earth*, 108(B5):1–8.

Farr, T. G., Rosen, P. A., Caro, E., Crippen, R., Duren, R., Hensley, S., Kobrick, M., Paller, M., Rodriguez, E., Roth, L., Seal, D., Shaffer, S., Shimada, J., Umland, J., Werner, M., Oskin, M., Burbank, D., and Alsdorf, D. (2007). The shuttle radar topography mission. *Reviews of Geophysics*, 45(2).

Fattahi, H. and Amelung, F. (2013). DEM error correction in InSAR time series. *IEEE Transactions on Geoscience and Remote Sensing*, 51(7):4249–4259.

Fattahi, H. and Amelung, F. (2014). InSAR uncertainty due to orbital errors. *Geophysical Journal International*, 199(1):549–560.

Ferretti, A., Fumagalli, A., Novali, F., Prati, C., Rocca, F., and Rucci, A. (2011). A new algorithm for processing interferometric data-stacks: SqueeSAR. *IEEE Transactions on Geoscience and Remote Sensing*, 49(9):3460–3470.

Ferretti, A., Prati, C., and Rocca, F. (2000). Nonlinear subsidence rate estimation using permanent scatterers in differential SAR interferometry. *IEEE Transactions on Geoscience and Remote Sensing*, 38(5):2202–2212.

Ferretti, A., Prati, C., and Rocca, F. (2001). Permanent scatterers in sar interferometry. *IEEE Transactions on geoscience and remote sensing*, 39(1):8–20.

Filliben, J. J. (1975). The probability plot correlation coefficient test for normality. *Technometrics*, 17(1):111–117.

Fornaro, G., Verde, S., Reale, D., and Pauciullo, A. (2015). CAESAR: An approach based on covariance matrix decomposition to improve multibaseline–multitemporal interferometric SAR processing. *IEEE Transactions on Geoscience and Remote Sensing*, 53(4):2050–2065.

Foulger, G. R., Wilson, M. P., Gluyas, J. G., Julian, B. R., and Davies, R. J. (2018). Global review of human-induced earthquakes. *Earth-Science Reviews*, 178:438–514.

Frohlich, C., DeShon, H., Stump, B., Hayward, C., Hornbach, M., and Walter, J. I. (2016a). A historical review of induced earthquakes in texas. *Seismological Research Letters*, 87(4):1022–1038.

Frohlich, C., DeShon, H., Stump, B., Hayward, C., Hornbach, M., and Walter, J. I. (2016b). Reply to "comment on 'a historical review of induced earthquakes in texas' by cliff frohlich, heather DeShon, brian stump, chris hayward, matt hornbach, and jacob i. walter" by steve everley. *Seismological Research Letters*, 87(6):1381–1383.

Frohlich, C., Hayward, C., Rosenblit, J., Aiken, C., Hennings, P., Savvaidis, A., Lemons, C., Horne, E., Walter, J. I., and DeShon, H. R. (2019). Onset and cause of increased seismic activity near pecos, west texas, usa from observations at the lajitas txar seismic array. *Journal of Geophysical Research: Solid Earth*.

Gabriel, A. K., Goldstein, R. M., and Zebker, H. A. (1989). Mapping small elevation changes over large areas: Differential radar interferometry. *Journal of Geophysical Research*, 94(B7):9183.

Gaddes, M. E., Hooper, A., Bagnardi, M., Inman, H., and Albino, F. (2018). Blind signal separation methods for InSAR: The potential to automatically detect and monitor signals of volcanic deformation. *Journal of Geophysical Research: Solid Earth*, 123(11):10,226–10,251.

Gan, W. and Frohlich, C. (2013). Gas injection may have triggered earthquakes in the cogdell oil field, texas. *Proceedings of the National Academy of Sciences*, 110(47):18786–18791.

Gaswirth, S. B. and Marra, K. R. (2016). Assessment of undiscovered continuous oil resources in the wolfcamp shale of the midland basin, permian basin province, texas, 2016. Technical report, US Geological Survey.

Ge, J., Nicot, J.-P., Hennings, P., Smye, K., Hosseini, S., Gao, R., and Breton, C. (2022). Recent water disposal and pore pressure evolution in the Delaware Mountain Group, Delaware Basin, Southeast New Mexico and West Texas, USA. *Journal of Hydrology: Regional Studies*, 40:101041.

Geertsma, J. et al. (1973). Land subsidence above compacting oil and gas reservoirs. *Journal of Petroleum Technology*, 25(06):734–744.

Goldstein, R. M. and Zebker, H. A. (1987). Interferometric radar measurement of ocean surface currents. *Nature*, 328(6132):707–709.

Goldstein, R. M., Zebker, H. A., and Werner, C. L. (1988). Satellite radar interferometry: Two-dimensional phase unwrapping. *Radio Science*, 23(4):713–720.

Graham, L. (1974). Synthetic interferometer radar for topographic mapping. *Proceedings of the IEEE*, 62(6):763–768.

Gray, A. L., Mattar, K. E., and Sofko, G. (2000). Influence of ionospheric electron density fluctuations on satellite radar interferometry. *Geophysical Research Letters*, 27(10):1451–1454.

Grigoli, F., Cesca, S., Priolo, E., Rinaldi, A. P., Clinton, J. F., Stabile, T. A., Dost, B., Fernandez, M. G., Wiemer, S., and Dahm, T. (2017). Current challenges in monitoring, discrimination, and management of induced seismicity related to underground industrial activities: A european perspective. *Reviews of Geophysics*, 55(2):310–340.

Grigoratos, I., Rathje, E., Bazzurro, P., and Savvaidis, A. (2020). Earthquakes induced by wastewater injection, part II: Statistical evaluation of causal factors and seismicity rate forecasting. *Bulletin of the Seismological Society of America*, 110(5):2483–2497.

Guarnieri, A. M. and Tebaldini, S. (2008). On the exploitation of target statistics for SAR interferometry applications. *IEEE Transactions on Geoscience and Remote Sensing*, 46(11):3436–3443.

Hampel, F. R. (1974). The Influence Curve and its Role in Robust Estimation. *Journal of the American Statistical Association*, 69(346):383–393.

Hanssen, R. (2001). *Radar Interferometry: Data Interpretation and Error Analysis*. Remote Sensing and Digital Image Processing. Springer.

112

Hanssen, R. F., Weckwerth, T. M., Zebker, H. A., and Klees, R. (1999). High-resolution water vapor mapping from interferometric radar measurements. *Science*, 283(5406):1297–1299.

Hasegawa, H. S., Wetmiller, R. J., and Gendzwill, D. J. (1989). Induced seismicity in mines in canada?an overview. *Pure and Applied Geophysics PAGEOPH*, 129(3-4):423–453.

Havazli, E. and Wdowinski, S. (2021). Detection threshold estimates for InSAR time series: A simulation of tropospheric delay approach. *Sensors*, 21(4):1124.

Hennings, P., Dvory, N., Horne, E., Li, P., Savvaidis, A., and Zoback, M. (2021). Stability of the fault systems that host-induced earthquakes in the delaware basin of west texas and southeast new mexico. *The Seismic Record*, 1(2):96–106.

Hooper, A., Bekaert, D., Spaans, K., and Arıkan, M. (2012). Recent advances in SAR interferometry time series analysis for measuring crustal deformation. *Tectonophysics*, 514:1–13.

Hooper, A. J. (2006). *Persistent scatter radar interferometry for crustal deformation studies and modeling of volcanic deformation*. Stanford University.

Horne, E. A., , Hennings, P. H., and Zahm, C. K. (2021). Basement-rooted faults of the delaware basin and central basin platform, permian basin, west texas and southeastern new mexico. In *The Geologic Basement of Texas: A Volume in Honor of Peter T. Flawn*. University of Texas at Austin, Bureau of Economic Geology.

Huang, M.-H., Fielding, E. J., Dickinson, H., Sun, J., Gonzalez-Ortega, J. A., Freed, A. M., and Bürgmann, R. (2017). Fault geometry inversion and slip distribution of the 2010 mw 7.2 el mayor-cucapah earthquake from geodetic data. *Journal of Geophysical Research: Solid Earth*, 122(1):607–621.

Hubbert, M. K. and Rubey, W. W. (1959). Role of fluid pressure in mechanics of overthrust faulting. *Geological Society of America Bulletin*, 70(2):115.

Jacobs, T. D. B., Junge, T., and Pastewka, L. (2017). Quantitative characterization of surface topography using spectral analysis. *Surface Topography: Metrology and Properties*, 5(1):013001.

Jolivet, R., Agram, P. S., Lin, N. Y., Simons, M., Doin, M.-P., Peltzer, G., and Li, Z. (2014). Improving InSAR geodesy using global atmospheric models. *Journal of Geophysical Research: Solid Earth*, 119(3):2324–2341.

Jolivet, R., Grandin, R., Lasserre, C., Doin, M.-P., and Peltzer, G. (2011). Systematic InSAR tropospheric phase delay corrections from global meteorological reanalysis data. *Geophysical Research Letters*, 38(17):n/a–n/a.

JPL, N. (2013). NASA shuttle radar topography mission global 1 arc second. *NASA LP DAAC*, 15.

Jung, J., jin Kim, D., Lavalle, M., and Yun, S.-H. (2016). Coherent change detection using InSAR temporal decorrelation model: A case study for volcanic ash detection. *IEEE Transactions on Geoscience and Remote Sensing*, 54(10):5765–5775.

Kellndorfer, J., Cartus, O., Lavalle, M., Magnard, C., Milillo, P., Oveisgharan, S., Osmanoglu, B., Rosen, P. A., and Wegmüller, U. (2022). Global seasonal sentinel-1 interferometric coherence and backscatter data set. *Scientific Data*, 9(1).

Keranen, K. M. and Weingarten, M. (2018). Induced seismicity. *Annual Review of Earth and Planetary Sciences*, 46(1):149–174.

Khakim, M., Tsuji, T., and Matsuoka, T. (2012). Geomechanical modeling for insar-derived surface deformation at steam-injection oil sand fields. *Journal of Petroleum Science and Engineering*, 96-97:152 – 161.

Kim, J.-W. and Lu, Z. (2018). Association between localized geohazards in west texas and human activities, recognized by sentinel-1a/b satellite radar imagery. *Scientific Reports*, 8(1):4727.

Kitajima, N., Seto, R., Yamazaki, D., Zhou, X., Ma, W., and Kanae, S. (2021). Potential of a SAR small-satellite constellation for rapid monitoring of flood extent. *Remote Sensing*, 13(10):1959.

Kulu, E. (2021). Satellite constellations-2021 industry survey and trends. In *35th Annual Small Satellite Conference*.

Lauknes, T. R. (2011). Insar tropospheric stratification delays: Correction using a small baseline approach. *IEEE Geoscience and Remote Sensing Letters*, 8(6):1070–1074.

Li, F. and Goldstein, R. (1990). Studies of multibaseline spaceborne interferometric synthetic aperture radars. *IEEE Transactions on Geoscience and Remote Sensing*, 28(1):88–97.

Li, Z. (2005). Interferometric synthetic aperture radar (InSAR) atmospheric correction: GPS, moderate resolution imaging spectroradiometer (MODIS), and InSAR integration. *Journal of Geophysical Research: Solid Earth*, 110(B3).

Liang, C., Agram, P., Simons, M., and Fielding, E. J. (2019). Ionospheric correction of insar time series analysis of c-band sentinel-1 tops data. *IEEE Transactions on Geoscience and Remote Sensing*, 57(9):6755–6773.

Lindeberg, T. (1993). Detecting salient blob-like image structures and their scales with a scale-space primal sketch: A method for focus-of-attention. *International Journal of Computer Vision*, 11(3):283–318.

Lindeberg, T. (1998). Feature detection with automatic scale selection. *International Journal of Computer Vision*, 30(2):79–116.

Liu, S. (2012). *Satellite radar interferometry: estimation of atmospheric delay*. PhD thesis, Delft University of Technology.

Lohman, R. B. and Simons, M. (2005). Some thoughts on the use of InSAR data to constrain models of surface deformation: Noise structure and data downsampling. *Geochemistry, Geophysics, Geosystems*, 6(1):n/a–n/a.

Lomax, A. and Savvaidis, A. (2019). Improving absolute earthquake location in west texas using probabilistic, proxy ground-truth station corrections. *Journal of Geophysical Research: Solid Earth*.

Lowe, D. G. (2004). Distinctive image features from scale-invariant keypoints. *International Journal of Computer Vision*, 60(2):91–110.

Lund Snee, J. and Zoback, M. (2018). State of stress in the permian basin, texas and new mexico: Implications for induced seismicity. *The Leading Edge*, 37(2):127–134.

Massonnet, D., Rossi, M., Carmona, C., Adragna, F., Peltzer, G., Feigl, K., and Rabaute, T. (1993). The displacement field of the Landers earthquake mapped by radar interferometry. *Nature*, 364:138–142.

Maurer, J., Bekaert, D. P., Sangha, S., Buzzanga, B. A., Marshak, C., Lei, Y., Kumar, P., and Fattahi, H. (2021). Raider: Raytracing atmospheric delay estimation for radar. In *AGU Fall Meeting 2021*. AGU.

McGarr, A. and Barbour, A. J. (2017). Wastewater disposal and the earthquake sequences during 2016 near fairview, pawnee, and cushing, oklahoma. *Geophysical Research Letters*, 44(18):9330–9336.

Michaelides, R. J. (2020). *Quantifying permafrost processes and soil moisture with interferometric phase and closure phase*. PhD thesis, Stanford Unniversity.

Michaelides, R. J., Zebker, H. A., and Zheng, Y. (2019). An algorithm for estimating and correcting decorrelation phase from insar data using closure phase triplets. *IEEE Transactions on Geoscience and Remote Sensing*, 57(12):10390–10397.

Moreira, A. (2014). A golden age for spaceborne SAR systems. In *2014 20th International Conference on Microwaves, Radar and Wireless Communications (MIKON)*. IEEE.

Morishita, Y., Lazecky, M., Wright, T. J., Weiss, J. R., Elliott, J. R., and Hooper, A. (2020). LiCSBAS: An open-source InSAR time series analysis package integrated with the LiCSAR automated Sentinel-1 InSAR processor. *Remote Sensing*, 12(3):424.

Murray, K. D., Bekaert, D. P., and Lohman, R. B. (2019). Tropospheric corrections for insar: statistical assessments and applications to the central united states and mexico. *Remote Sensing of Environment*, 232:111326.

Murray, K. D., Lohman, R. B., and Bekaert, D. P. S. (2021). Cluster-based empirical tropospheric corrections applied to InSAR time series analysis. *IEEE Transactions on Geoscience and Remote Sensing*, 59(3):2204–2212.

Nicholson, C. and Wesson, R. L. (1990). Earthquake hazard associated with deep well injection. Technical report, U.S. Geological Survey.

Okada, Y. (1992). Internal deformation due to shear and tensile faults in a half-space. *Bulletin of the Seismological Society of America*, 82(2):1018–1040.

Onn, F. (2006). *Modeling Water Vapor Using GPS With Application To Mitigating Insar Atmospheric Distortions.* PhD thesis, Stanford University.

Parker, A. L., Biggs, J., Walters, R. J., Ebmeier, S. K., Wright, T. J., Teanby, N. A., and Lu, Z. (2015). Systematic assessment of atmospheric uncertainties for InSAR data at volcanic arcs using large-scale atmospheric models: Application to the cascade volcanoes, united states. *Remote Sensing of Environment*, 170:102–114.

Pepin, K. S., Ellsworth, W. L., Sheng, Y., and Zebker, H. A. (2022). Shallow aseismic slip in the delaware basin determined by sentinel-1 InSAR. *Journal of Geophysical Research: Solid Earth*, 127(2).

Raspini, F., Bianchini, S., Ciampalini, A., Soldato, M. D., Solari, L., Novali, F., Conte, S. D., Rucci, A., Ferretti, A., and Casagli, N. (2018). Continuous, semi-automatic monitoring of ground deformation using sentinel-1 satellites. *Scientific Reports*, 8(1).

Rosen, P., Hensley, S., Joughin, I., K.Li, F., Madsen, S., Rodriguez, E., and Goldstein, R. M. (2000). Synthetic Aperture Radar Interferometry. *Proceedings of the IEEE*, 88(3):333–382.

Rosen, P. A., Gurrola, E., Sacco, G. F., and Zebker, H. (2012). The insar scientific computing environment. In *EUSAR 2012; 9th European Conference on Synthetic Aperture Radar*, pages 730–733. VDE.

Rosen, P. A., Hensley, S., and Chen, C. (2010). Measurement and mitigation of the ionosphere in l-band interferometric SAR data. In *2010 IEEE Radar Conference*. IEEE.

Rosen, P. A., Hensley, S., Shaffer, S., Veilleux, L., Chakraborty, M., Misra, T., Bhan, R., Sagi, V. R., and Satish, R. (2015). The NASA-ISRO SAR mission - an international space partnership for science and societal benefit. In *2015 IEEE Radar Conference (RadarCon)*. IEEE.

Rouet-Leduc, B., Jolivet, R., Dalaison, M., Johnson, P. A., and Hulbert, C. (2021). Autonomous extraction of millimeter-scale deformation in InSAR time series using deep learning. *Nature Communications*, 12(1).

Rousseeuw, P. J. and Hubert, M. (2011). Robust statistics for outlier detection. *Wiley Interdisciplinary Reviews: Data Mining and Knowledge Discovery*, 1(1):73–79.

Rubinstein, J. L. and Mahani, A. B. (2015). Myths and facts on wastewater injection, hydraulic fracturing, enhanced oil recovery, and induced seismicity. *Seismological Research Letters*, 86(4):1060–1067.

Sandwell, D., Mellors, R., Tong, X., Wei, M., and Wessel, P. (2011). Open radar interferometry software for mapping surface deformation. *Eos, Transactions American Geophysical Union*, 92(28):234–234.

Sandwell, D. T. and Price, E. J. (1998). Phase gradient approach to stacking interferograms. *Journal of Geophysical Research: Solid Earth*, 103(B12):30183–30204.

Savvaidis, A., Lomax, A., and Breton, C. (2020). Induced seismicity in the delaware basin, west texas, is caused by hydraulic fracturing and wastewater disposal. *Bulletin of the Seismological Society of America*, 110(5):2225–2241.

Savvaidis, A., Young, B., Huang, G.-c. D., and Lomax, A. (2019). Texnet: A statewide seismological network in texas. *Seismological Research Letters*.

Scanlon, B. R., Ikonnikova, S., Yang, Q., and Reedy, R. C. (2020). Will water issues constrain oil and gas production in the united states? *Environmental Science & Technology*, 54(6):3510–3519.

Scott, D. W. (2015). *Multivariate Density Estimation: Theory, Practice, and Visualization*. John Wiley & Sons, second edition.

Segall, P. (1992). Induced stresses due to fluid extraction from axisymmetric reservoirs. *pure and applied geophysics*, 139(3):535–560.

Segall, P. (2010). *Earthquake and Volcano Deformation*. Princeton University Press.

Segall, P. and Heimisson, E. R. (2019). On the integrated surface uplift for dip-slip faults. *Bulletin of the Seismological Society of America*, 109(6):2738–2740.

Semple, A. G., Pritchard, M. E., and Lohman, R. B. (2017). An incomplete inventory of suspected human-induced surface deformation in north america detected by satellite interferometric synthetic-aperture radar. *Remote Sensing*, 9(12):1296.

Shearer, P. M. (2019). *Introduction to Seismology*. Cambridge University Press.

Shirzaei, M., Ellsworth, W. L., Tiampo, K. F., González, P. J., and Manga, M. (2016). Surface uplift and time-dependent seismic hazard due to fluid injection in eastern Texas. *Science*, 353(6306):1416–1419. ISBN: 1095-9203 (Electronic) 0036-8075 (Linking).

Shukla, P., Kumar, V., Curtis, M., Sondergeld, C. H., and Rai, C. S. (2013). Nanoindentation studies on shales. *American Rock Mechanics Association*.

Simons, M. and Rosen, P. (2007). Interferometric synthetic aperture radar geodesy. In *Treatise on Geophysics*, pages 391–446. Elsevier.

Simpson, D., Leith, W., and Scholz, C. (1988). Two types of reservoir-induced seismicity. *Bulletin of the Seismological Society of America*, 78(6):2025–2040.

Skoumal, R. J., Barbour, A. J., Brudzinski, M. R., Langenkamp, T., and Kaven, J. O. (2020a). Induced seismicity in the delaware basin, texas. *Journal of Geophysical Research: Solid Earth*, 125(1).

Skoumal, R. J., Kaven, J. O., Barbour, A. J., Wicks, C., Brudzinski, M. R., Cochran, E. S., and Rubinstein, J. L. (2020b). The induced M_w 5.0 March 2020 West Texas seismic sequence. *Journal of Geophysical Research: Solid Earth*, 126(1).

Smith, E. and Weintraub, S. (1953). The constants in the equation for atmospheric refractive index at radio frequencies. *Proceedings of the IRE*, 41(8):1035–1037.

Solheim, F. S., Vivekanandan, J., Ware, R. H., and Rocken, C. (1999). Propagation delays induced in GPS signals by dry air, water vapor, hydrometeors, and other particulates. *Journal of Geophysical Research: Atmospheres*, 104(D8):9663–9670.

Staniewicz, S., Chen, J., Lee, H., Olson, J., Savvaidis, A., Reedy, R., Breton, C., Rathje, E., and Hennings, P. (2020). InSAR reveals complex surface deformation patterns over an 80,000 km^2 oil-producing region in the permian basin. *Geophysical Research Letters*, 47(21):e2020GL090151.

Strang, G. (2006). *Linear algebra and its applications*. Thomson, Brooks/Cole, Belmont, CA.

Stringham, C., Farquharson, G., Castelletti, D., Quist, E., Riggi, L., Eddy, D., and Soenen, S. (2019). The capella x-band SAR constellation for rapid imaging. In *IGARSS 2019 - 2019 IEEE International Geoscience and Remote Sensing Symposium*. IEEE.

Szeliski, R. (2022). *Computer Vision: Algorithms and Applications*. Springer International Publishing, second edition.

Talwani, P. (1997). On the nature of reservoir-induced seismicity. *Pure and Applied Geophysics*, 150(3-4):473–492.

Taylor, L. S., Quincey, D. J., Smith, M. W., Baumhoer, C. A., McMillan, M., and Mansell, D. T. (2021). Remote sensing of the mountain cryosphere: Current capabilities and future opportunities for research. *Progress in Physical Geography: Earth and Environment*, 45(6):931–964.

Tebaldini, S. and Guarnieri, A. M. (2010). Methods and performances for multipass SAR interferometry. In *Geoscience and Remote Sensing New Achievements*. InTech.

The Academy of Medicine, E. and of Texas, S. (2017). *Environmental and Community Impacts of Shale Development in Texas*. The Academy of Medicine, Engineering and Science of Texas (TAMEST).

Torres, R., Snoeij, P., Geudtner, D., Bibby, D., Davidson, M., Attema, E., Potin, P., Rommen, B., Floury, N., Brown, M., Traver, I. N., Deghaye, P., Duesmann, B., Rosich, B., Miranda, N., Bruno, C., L'Abbate, M., Croci, R., Pietropaolo, A., Huchler, M., and Rostan, F. (2012). GMES sentinel-1 mission. *Remote Sensing of Environment*, 120:9–24.

Trugman, D. T. and Shearer, P. M. (2017). GrowClust: A hierarchical clustering algorithm for relative earthquake relocation, with application to the spanish springs and sheldon, nevada, earthquake sequences. *Seismological Research Letters*, 88(2A):379–391.

Tymofyeyeva, E. and Fialko, Y. (2015). Mitigation of atmospheric phase delays in InSAR data, with application to the eastern california shear zone. *Journal of Geophysical Research: Solid Earth*, 120(8):5952–5963.

van der Baan, M. and Calixto, F. J. (2017). Human-induced seismicity and large-scale hydrocarbon production in the USA and canada. *Geochemistry, Geophysics, Geosystems*, 18(7):2467–2485.

Vasco, D. W. and Ferretti, A. (2005). On the use of quasi-static deformation to understand reservoir fluid flow. *GEOPHYSICS*, 70(4):O13–O27.

Vasco, D. W., Ferretti, A., and Novali, F. (2008). Reservoir monitoring and characterization using satellite geodetic data: Interferometric synthetic aperture radar observations from the krechba field, algeria. *GEOPHYSICS*, 73(6):WA113–WA122.

Verdon, J. P., Baptie, B. J., and Bommer, J. J. (2019). An improved framework for discriminating seismicity induced by industrial activities from natural earthquakes. *Seismological Research Letters*.

Waters, G. A., Heinze, J. R., Jackson, R., Ketter, A. A., Daniels, J. L., and Bentley, D. (2006). *SPE-103202-MS*, chapter Use of Horizontal Well Image Tools to Optimize Barnett Shale Reservoir Exploitation, page 13. Society of Petroleum Engineers, San Antonio, Texas, USA.

Wiley, C. (1985). Synthetic aperture radars. *IEEE Transactions on Aerospace and Electronic Systems*, AES-21(3):440–443.

Wiley, C. A. (U.S. Patent 3 196 436, Aug. 1954). Pulsed doppler radar methods and apparatus.

Wu, C. (1976). A digital system to produce imagery from SAR data. In *Systems Design Driven by Sensors*. American Institute of Aeronautics and Astronautics.

Xu, S. and Zoback, M. D. (2015). Analysis of stress variations with depth in the permian basin spraberry/dean/wolfcamp shale. In *49th US Rock Mechanics/Geomechanics Symposium*. American Rock Mechanics Association.

Yague-Martinez, N., Leach, N. R., Dasgupta, A., Tellman, E., and Brown, J. S. (2021). Towards frequent flood mapping with the capella sar system. the 2021 eastern australia floods case. In *2021 IEEE International Geoscience and Remote Sensing Symposium IGARSS*. IEEE.

Yu, C., Li, Z., and Penna, N. T. (2018a). Interferometric synthetic aperture radar atmospheric correction using a gps-based iterative tropospheric decomposition model. *Remote Sensing of Environment*, 204:109–121.

Yu, C., Li, Z., Penna, N. T., and Crippa, P. (2018b). Generic atmospheric correction model for interferometric synthetic aperture radar observations. *Journal of Geophysical Research: Solid Earth*, 123(10):9202–9222.

Yu, C., Penna, N. T., and Li, Z. (2017). Generation of real-time mode high-resolution water vapor fields from gps observations. *Journal of Geophysical Research: Atmospheres*, 122(3):2008–2025.

Yunjun, Z., Fattahi, H., and Amelung, F. (2019). Small baseline insar time series analysis: Unwrapping error correction and noise reduction. *Computers & Geosciences*, 133:104331.

Zan, F. D. and Gomba, G. (2018). Vegetation and soil moisture inversion from SAR closure phases: First experiments and results. *Remote Sensing of Environment*, 217:562–572.

Zan, F. D. and Guarnieri, A. M. (2006). TOPSAR: Terrain observation by progressive scans. *IEEE Transactions on Geoscience and Remote Sensing*, 44(9):2352–2360.

Zan, F. D., Parizzi, A., Prats-Iraola, P., and Lopez-Dekker, P. (2014). A SAR interferometric model for soil moisture. *IEEE Transactions on Geoscience and Remote Sensing*, 52(1):418–425.

Zan, F. D., Zonno, M., and Lopez-Dekker, P. (2015). Phase inconsistencies and multiple scattering in SAR interferometry. *IEEE Transactions on Geoscience and Remote Sensing*, 53(12):6608–6616.

Zebker, H. (2021). Accuracy of a model-free algorithm for temporal InSAR tropospheric correction. *Remote Sensing*, 13(3):409.

Zebker, H. A. (2017). User-friendly insar data products: fast and simple timeseries processing. *IEEE Geoscience and Remote Sensing Letters*, 14(11):2122–2126.

Zebker, H. A. (2018). Insar mission-level products on demand - do we need range-doppler? In *IGARSS 2018 - 2018 IEEE International Geoscience and Remote Sensing Symposium*. IEEE.

Zebker, H. A. and Goldstein, R. M. (1986). Topographic mapping from interferometric synthetic aperture radar observations. *Journal of Geophysical Research*, 91(B5):4993.

Zebker, H. A., Rosen, P. A., and Hensley, S. (1997). Atmospheric effects in interferometric synthetic aperture radar surface deformation and topographic maps. *Journal of Geophysical Research: Solid Earth*, 102(B4):7547–7563. Publisher: Wiley Online Library.

Zebker, H. A. and Villasenor, J. (1992). Decorrelation in interferometric radar echoes. *IEEE Transactions on Geoscience and Remote Sensing*, 30(5):950–959.

Zhai, G., Shirzaei, M., and Manga, M. (2021). Widespread deep seismicity in the delaware basin, texas, is mainly driven by shallow wastewater injection. *Proceedings of the National Academy of Sciences*, 118(20).

Zheng, W., Kim, J.-W., Ali, S. T., and Lu, Z. (2019). Wastewater leakage in west texas revealed by satellite radar imagery and numerical modeling. *Scientific Reports*, 9(1):14601.

Zheng, Y. (2019). *Imaging Cascadia Slow Slip Events with Modern Interferometric Synthetic Aperture Radar Datasets*. PhD thesis, Stanford University.

Zheng, Y., Fattahi, H., Agram, P., Simons, M., and Rosen, P. (2022). On closure phase and systematic bias in multi-looked SAR interferometry. *IEEE Transactions on Geoscience and Remote Sensing*, pages 1–1.

Zheng, Y. and Zebker, H. A. (2017). Phase correction of single-look complex radar images for user-friendly efficient interferogram formation. *IEEE Journal of Selected Topics in Applied Earth Observations and Remote Sensing*, 10(6):2694–2701.

Zwieback, S., Hensley, S., and Hajnsek, I. (2015). Assessment of soil moisture effects on l-band radar interferometry. *Remote Sensing of Environment*, 164:77–89.

Zwieback, S., Hensley, S., and Hajnsek, I. (2017). Soil moisture estimation using differential radar interferometry: Toward separating soil moisture and displacements. *IEEE Transactions on Geoscience and Remote Sensing*, 55(9):5069–5083.

Zwieback, S. and Meyer, F. J. (2022). Reliable InSAR phase history uncertainty estimates. *IEEE Transactions on Geoscience and Remote Sensing*, 60:1–9.